Electromagnetic Formation Flight of Satellite Arrays

By

DANIEL W. KWON

S.B. Aeronautical and Astronautical Engineering
Massachusetts Institute of Technology, 2002

S.B. Electrical Engineering and Computer Science
Massachusetts Institute of Technology, 2002

SUBMITTED TO THE DEPARTMENT OF
AERONAUTICAL AND ASTRONAUTICAL ENGINEERING
IN PARTIAL FULLFILLMENT OF THE DEGREE OF

MASTER OF SCIENCE IN AERONAUTICS AND ASTRONAUTICS

at the

MASSACHUSETTS INSTITUTE OF TECHNOLOGY

February 2005

Signature of Author.....
Department of Aeronautics and Astronautics
December 10, 2004

Certified by.....
David W. Miller
Associate Professor of Aeronautics and Astronautics
Thesis Supervisor

Accepted by.....
Jaime Peraire
Professor of Aeronautics and Astronautics
Chair, Committee on Graduate Student

Electromagnetic Formation Flight of Satellite Arrays

by

DANIEL W. KWON

Submitted to the Department of Aeronautics and Astronautics
on December 10, 2004 in Partial Fulfillment of the
Requirements for the Degree of Master of Science
in Aeronautics and Astronautics
at the Massachusetts Institute of Technology

Abstract

Proposed methods of actuating spacecraft in sparse aperture arrays use propellant as a reaction mass. For formation flying systems, propellant becomes a critical consumable which can be quickly exhausted while maintaining relative orientation. Furthermore, the total required propellant mass is highly dependant on ΔV, which requires propellant mass to increase exponentially. Additional problems posed by propellant include optical contamination, plume impingement, thermal emission, and vibration excitation.

For those missions where control of relative degrees of freedom is important, we consider using a system of electromagnets, in concert with reaction wheels, to replace the consumables. A system of electromagnets, powered by solar energy, does not rely on consumables such as propellant mass.

To fully understand the benefits of using formation flown architectures, we first investigate how the science returns are affected, using NASA's Terrestrial Planet Finder (TPF) as an example. Electromagnets are then implemented on simple multi-spacecraft arrays to understand how the design impacts overall system performance. This model is expanded to include subsystems critical for operation using electromagnets. TPF is then used to benchmark its performance against various micropropulsion systems. Finally the use of electromagnets for multiple roles in space systems is discussed.

Thesis Supervisor: David W. Miller
Title: Associate Professor of Aeronautics and Astronautics

ACKNOWLEDGMENTS

To Dave Li, former roommate and friend.

See you in space.

TABLE OF CONTENTS

Abstract 3

Acknowledgments 5

Table of Contents 7

List of Figures 11

List of Tables 17

Chapter 1 19

1.1 Motivation 19

1.2 Previous and Current Projects 20

1.3 Thesis Objectives 22

1.4 Thesis Outline 22

Chapter 2 25

2.1 Nomenclature 25

2.2 Uncertainty 26

2.2.1 Introduction to $\eta_{\oplus}$ and η_u 26

2.2.2 Effects of η_u 27

2.2.3 When Does η_u Change 30

2.3 Completeness 32

2.3.1 Cost Model 37

2.3.2 Completeness Baseline Trends 39

2.4 Fixed vs. Variable Baseline System 45

2.5 Architecture Conclusions 48

Chapter 3 49

3.1 EMFF Background 49

3.2 Circular Trajectories 53

3.2.1 Agility Sizing 54

3.2.2 Mission Efficiency Sizing 63

3.2.3 Non-Identical Configuration 66

3.3 Linear Trajectories 71

3.3.1 Escape Velocity 76

3.4 Conclusions and Future System Trades Work 77

Chapter 4 79

4.1 Superconducting Wire Performance Variation 79

4.1.1 Effects on spacecraft acceleration 85

4.1.2 Effects on total loop current 89

4.2 Thermal Subsystem 91

4.2.1 Earth Trailing Orbit 93

4.2.2 Low Earth Orbit 96

4.2.3 Material Selection 98

4.2.4 Thermal Subsystem Conclusions 99

4.3 Structure 99

4.3.1 Beam analysis and trends 100

4.3.2 Future Structural Model Considerations 103

4.4 Power 104

4.4.1 Design Overview 104

4.4.2 Experimental Calculations 105

4.4.3 Theoretical Analysis 109

4.5 Avionics Performance using GPS 112

4.6 Subsystems Summary 114

Chapter 5 117

5.1 Overview of original model 118

5.2 Higher Fidelity Model 121

5.2.1 Overview 121

5.2.2 EMFF model 124

5.2.3 Micropropulsion System Designs 137

5.3 Results 143

5.4 Conclusions and Future Work 146

Chapter 6 149

6.1 Power Transmission 149

6.2 Passive offensive capability 153

6.3 Passive Defensive Capabilities 157

6.4 Communications 157

6.5 Multi-role Conclusions 158

Chapter 7 159

7.1 Thesis Summary 159

7.2 Contributions 163

7.3 Recommendations for Future Work 163

Appendix A 165

References 167

LIST OF FIGURES

Figure 2.1 Example Poisson distribution 28

Figure 2.2 Pictorial depiction of $\eta_{\oplus}$ and η_u in the set of all stars 29

Figure 2.3 Precursor mission timeline 30

Figure 2.4 Relationship of metal rich stars and planetary occurrences [14] 31

Figure 2.5 Regions around a star 34

Figure 2.6 Completeness vs. $\frac{r_{iwd}}{r_i}$ for different α 37

Figure 2.7 Theoretical star distribution [16] 39

Figure 2.8 Potential planet gain vs. minimum SSI baseline 42

Figure 2.9 Science productivity ratio of SSI and SCI vs. baseline ratio for different inner habitable zone and inner working distance ratios 44

Figure 2.10 Baseline variability for the $\frac{SSI}{SCI}$ ratio 45

Figure 2.11 Completeness for two fixed baseline systems 46

Figure 2.12 Completeness for a fixed and variable baseline system 48

Figure 3.1 Far field magnetic model 50

Figure 3.2 Two dipoles interacting in the far field 51

Figure 3.3 Two unequal mass satellites and coils with identical radius coils rotating around their common bari-center 54

Figure 3.4 Rotation rate versus vehicle B coil mass 56

Figure 3.5 Mass breakdown for vehicle B 57

Figure 3.6 Separation distance versus vehicle B core mass for different HTS technology levels and coil radii, five minute revolution period 58

Figure 3.7 Coil radius versus vehicle B core mass, that provide a five minute period at 25 meters of separation, for three different HTS technology levels 58

Figure 3.8 Dipole orientations during angular acceleration 59

Figure 3.9 Reaction wheel versus core mass 60

Figure 3.10 Two identical spacecraft orbiting about a third 61

Figure 3.11 Rotation rate versus vehicle B coil mass for two and three spacecraft arrays 63

Figure 3.12 Mission efficiency comparison for additional spacecraft 67

Figure 3.13 EM mass distribution effect on rotation rate for a three spacecraft TPF-class array 70

Figure 3.14 Optimal electromagnetic mass fraction of the center spacecraft for three spacecraft array with 600 kg dry mass 71

Figure 3.15 Two vehicles undergoing radial separation. 71

Figure 3.16 Temporal history for radial position and velocity. 72

Figure 3.17 Relative acceleration versus vehicle B coil mass for different vehicle B core masses 74

Figure 3.18 Core mass of vehicle B is 10 kg and coil mass is optimized at 7.55 kg. Maximum separation is 22.1 m 74

Figure 3.19 The fraction of the maximum magnetic moment in each vehicle as a function of time 75

Figure 3.20 Divergent trajectories resulting from a tenth of a second increase in acceleration time (<1%) and maximizing the magnetic moments in both vehicles . 76

Figure 3.21 Trajectory for threefold increase in HTS technology and 50 kg core mass for vehicle B. Maximum separation is 29.3 m. 76

Figure 4.1 Variation of HTS critical current density with temperature and magnetic field parallel (a) and perpendicular (b) to the HTS wire [18] 80

Figure 4.2 Geometry of HTS coil turns 80

Figure 4.3 Magnetic field from line currents 82

Figure 4.4 HTS wire stacks for the MIT-SSL EMFF testbed 82

Figure 4.5 Linear fit of a) I_c variation versus parallel magnetic field for 77 K, b) I_c variation versus temperature for B = 0.22 T 84

Figure 4.6 Cryogenic system power versus temperature for a 2.5 W thermal load..... 86

Figure 4.7 Acceleration with I_c variation from magnetic field and temperature normalized by acceleration with no I_c variation (77 K, no magnetic field) 89

Figure 4.8 Total loop current versus loop turns at 77 K 90

Figure 4.9 a) Gravity fed system b) Pressurized tank system 92

Figure 4.10 Coil geometry 93

Figure 4.11 Thermal free body diagrams for a) Insulation case b) Vacuum-gap case 93

Figure 4.12 Heat flow into the EMFF coils for insulator and vacuum-gap designs 95

Figure 4.13 Heat flow comparison for LEO and Earth trailing orbit..... 98

Figure 4.14 Material selection comparison for a) Earth trailing orbit, b) LEO 99

Figure 4.15 Simple three beam configuration for EMFF coil support structures 100

Figure 4.16 Cantilevered beam model 101

Figure 4.17 a) Acceleration versus coil radius, b) Optimal coil radius versus deflection constraint for 600 kg spacecraft, R_s = 2 m, M_c = 10 kg 103

Figure 4.18 Power system setup 105

Figure 4.19 Original power system battery configuration 106

Figure 4.20 Coil and battery operation, 10% duty cycle at 0.1 Hz 107

Figure 4.21 Helical coil 108

Figure 4.22 Resistance of mosfet as a function of temperature [21] 111

Figure 4.23 GPS test scenarios 112

Figure 4.24 GPS experimental test setups 113

Figure 4.25 GPS test summary 114

Figure 5.1 Five spacecraft TPF design using EMFF 117

Figure 5.2 Mass comparison for TPF using various propulsion systems (two hour rotation period) [22] 120

Figure 5.3 Flow diagram of EMFF system design 125

Figure 5.4 Custom reaction wheel curve fit 130

Figure 5.5 EMFF subsystem mass breakdown for various HTS technology levels, rotation periods, and baselines 136

Figure 5.6. On-axis and off-axis thruster configuration 139

Figure 5.7 ΔV for collector spacecraft 142

Figure 5.8 Mass comparison for TPF using various propulsion systems, four hour rotation period, 75 m baseline 144

Figure 5.9 Mass breakdown for various propulsion systems, four hour rotation period, 75 m baseline 145

Figure 5.10 EMFF (1x HTS technology) and PPT mass versus baseline for various rotation periods 146

Figure 6.1 Diagram of EMFF-FESM power sharing concept with non-EMFF vehicle reaction wheel arrangement 150

Figure 6.2 Notional time history of EMFF dipole and permanent magnet orientations in xy-plane 150

Figure 6.3 EMFF Deny, Degrade concept diagram 154

Figure 6.4 Degradation capabilities 156

Figure 6.5 EMFF protective magnetosphere 157

LIST OF TABLES

Table 2.1 Two Cases for determining the potential number of observable planets 34

Table 2.2 Example of uncertainty applied to three fixed baseline systems 47

Table 3.1 Parameters for baseline scenario 55

Table 3.2 Optimized design parameters for two spacecraft and *N* Spacecraft arrays 67

Table 3.3 Spacecraft mass breakdown [12] 69

Table 4.1 Parameters used to determine effect of I_c variation 88

Table 4.2 Cryocooler specifications 96

Table 4.3 Containment material properties 98

Table 4.4 EMFF testbed coil parameters and experimental power results 108

Table 4.5 EMFF testbed power subsystem component breakdown 110

Table 5.1 Summary of key equations for the micropropulsion systems 119

Table 5.2 Subsystems used in JPL, EMFF, and micropropulsion system models 122

Table 5.3 Collector spacecraft subsystem breakdown 123

Table 5.4 Summary of parameters used in TPF model 124

Table 5.5 Structures subsystem parameters 125

Table 5.6 Properties of Honeywell Aerospace Constellation Series momentum wheels 130

Table 5.7 Effects of temperature on I_c 134

Table 5.8 Reaction wheel masses for outer collector, eight hour rotation period, 75 m baseline 141

Table 5.9 PPT mass comparison 143

Table 6.1 EMFF-FESM power sharing parameters 152

Table 6.2 EMFF and target satellite parameters 156

Chapter 1

INTRODUCTION

1.1 Motivation

Missions using multiple spacecraft flying in formation are emerging as an alternative to traditional monolithic spacecraft. Some of the benefits of multiple spacecraft architectures include, but are not limited to: creation of large sensor apertures, mission flexibility, increased reliability, upgradeability, staged deployment, and lower costs. An example of a formation flight system is NASA's Terrestrial Planet Finder (TPF), whose goal is to detect Earth-like planets around nearby stars. One of the proposed architectures for TPF is an Infrared Michelson Interferometer consisting of five formation flown spacecraft.

One of the limitations of formation flight spacecraft is the propellant required for formation control. Since propellant is a consumable, the mission lifetime for a spacecraft is limited by the amount of propellant available, and once it is consumed, the spacecraft is rendered useless and its mission is over. Another problematic effect of propellant-based systems is impingement of thruster plumes on neighboring spacecraft. Plume impingement can contaminate precision optical surfaces, create unnecessary vibration excitation, produce inadvertent charging, and ablate material off a spacecraft surface. In addition, missions imaging in the infrared spectrum could be thermally blinded or obscured by propellant plumes across their line of sight [1].

Upon further inspection of distributed satellite systems, it is the maintenance of relative formation control that is important and most costly. There are two alternatives to using propellant for actuation of multiple spacecraft. First, an external field, such as the Earth's magnetic field, can be used given the necessary magnetic actuators on board. The second alternative is for each spacecraft to produce their own field that others in the formation

can react against. In this case momentum conservation prohibits control of the motion of the center of mass of the formation since only internal forces are present. This technique is achieved by creating a steerable magnetic dipole and is called Electromagnetic Formation Flight (EMFF).

EMFF is implemented on a spacecraft by driving current through three orthogonal electromagnetic coils to create a steerable magnetic dipole in three dimensions. EMFF, in concert with reaction wheels, can control the relative separation, relative attitude and inertial rotation for a satellite formation. These coils are powered by solar energy, a limitless resource. By obviating the need for consumables to control a formation, the mission lifetime is theoretically unbounded. The absence of thruster plumes also eliminates the malignant effects of impingement.

1.2 Previous and Current Projects

There are many benefits to EMFF, however there are also several challenging issues. One of the challenges of EMFF is that it involves coupled control and non-linear dynamics because the forces and torques are non-linear with separation distance and orientation. Elias developed a linearized model and optimal controller designs, which proved to be very effective despite the nonlinearities of the system's dynamics and the electromagnetic actuators [2].

The initial development of the Electromagnetic Formation Flight concept was investigated by Kong [3], who analyzed the mass fractions, power demands and volume requirements of EMFF on multi-spacecraft arrays. Early models of EMFF using magnetizable cores and multipole electromagnets were also investigated. TPF was retrofitted with EMFF coils and was used to benchmark EMFF against various propulsive options. It was shown that for long duration missions, EMFF was the most favorable option over thruster systems such as FEEPs, Colloids, and PPTs when considering overall system mass. In addition, spin-up of a five spacecraft TPF collinear array from rest using only electromagnets and reaction wheels was successfully simulated by Sedwick [4].

EMFF in low Earth orbit is also a possibility that has been investigated. EMFF can be used to counteract secular drift between spacecraft due to the Earth's J_2 perturbations [5]. It may also be feasible for re-orienting or re-sizing arrays. Considerations now include: operation in the presence of Earth's magnetic field; the strength needed to counteract differential drag and solar pressure; and interference with communication and radar payloads. Similar systems studies are also being conducted by Hashimoto [6]. An alternate technique of formation flight using electro-static monopoles to generate Coulomb forces has been investigated by King [7]. One difference between a system of electro-static monopoles and a system of electromagnetic dipoles (EMFF) is that the dipoles have the ability to create shear forces and movement in the shear direction.

Another consideration of EMFF that has been investigated by the Massachusetts Institute of Technology Space Systems Laboratory (MIT-SSL) is the effect that such fields can have on spacecraft avionics [8]. Shielding using materials such as mu-metal, analogous to a Faraday cage for electric fields, can help isolate sensitive electronics from high strength magnetic fields. Another option is to place small, oppositely poled dipoles (Helmholz coils) around the avionics bay to locally null the magnetic field near the avionics. One of the objectives of this thesis is to determine the performance of avionics in an EMFF system.

To demonstrate feasibility of the EMFF concept as well as verify near field interaction and test control algorithms, a ground testbed was developed by the MIT-SSL [9]. Two testbed vehicles containing two orthogonal high temperature superconducting wire coils and a single reaction wheel to generate torque about the vertical axis demonstrated controllability of the various degrees of freedom in two dimensions. The testbed was supported on a frictionless air carriage with power supplied by batteries. Each vehicle was identical and interchangeable and did not contain umbilicals. The first version of the testbed implemented a foam containment system and gravity fed liquid Nitrogen coolant tank for the high temperature superconductors. These were replaced by a soldered copper containment system and pressurized liquid Nitrogen coolant tank to create a more robust testbed. This second version of the testbed is currently investigating disturbance

rejection control and trajectory following for two EMFF vehicles to verify control algorithms.

Control using the EMFF testbed based on linearized controllers developed by Elias is one of the areas of current work. The testbed is also being used to develop other control schemes such as gain scheduling. The development of non-linear controllers and distributed control methodologies is being investigated for large EMFF arrays. Current work to further the understanding of the near field magnetic model and methods of managing angular momentum and torque using EMFF inside and outside of the Earth's magnetic field are also being investigated [10].

1.3 Thesis Objectives

The overall objective of this thesis is to analyze the effect of EMFF on multi-spacecraft arrays and spacecraft subsystems. To achieve this overall objective, the following sub-objectives must be considered:

- Develop trades on the performance of multi-spacecraft arrays using EMFF; performance is defined as the spacecraft agility and mission efficiency.
- Formulate models to describe the subsystems associated with EMFF.
- Develop a systematic framework for the implementation of EMFF on TPF.
- Investigate the potential benefits of using EMFF for multiple roles.

1.4 Thesis Outline

This thesis is divided into six main chapters plus an introduction and conclusions chapter. Chapter Two, the first main chapter, discusses the science requirements for an interferometry mission and uses TPF as an example. The goal of the chapter is to motivate the need for formation flying architectures. The concept of designing for uncertainty and completeness and how they impact the science goals of a mission is introduced and used to evaluate between a TPF design that is either structurally

connected or formation flown. A notion of completeness similar to Brown's [11] is introduced and evaluated in Chapter Two.

After understanding the benefits of a formation flown interferometer, Electromagnetic Formation Flight is proposed as the method of implementing such architectures. EMFF is first introduced in Chapter Three, which begins with an introduction to the far field model of the electromagnetic dipole. Building on the fundamental equations, configurations of EMFF spacecraft are optimized based on agility and mission efficiency for both circular trajectories and linear trajectories.

Following this systems analysis of EMFF, Chapter Four investigates the subsystem designs for a single EMFF spacecraft. The subsystems analyzed that are critical to EMFF are the superconducting wire, thermal, structure, power, and avionics subsystems.

After the subsystems have been detailed, Chapter Five incorporates the subsystems into a systems design for TPF. The current model for TPF developed by the Jet Propulsion Laboratory is retrofitted with EMFF and compared to thruster-based designs, which are modeled after Reichbach's micropropulsion systems [1]. The goal of this chapter is to understand the performance of EMFF and see how it compares in terms of mass for a future mission.

Chapter Six investigates the possibility of using EMFF in a multi-role sense, where EMFF spacecraft can perform several different tasks using the electromagnetic coils. The thesis wraps up with conclusions and recommendations for future work in Chapter Seven.

Chapter 2

IMPACT OF ARCHITECTURE ON RISK OF SCIENCE RETURN

A great deal of uncertainty is associated with the expected number of stars that may have Earth-like planets. The productivity of TPF over its mission lifetime depends on the ability of precursor science to assess which stars are the most likely candidates. Because the architecture downselect occurs before most of the precursor science data has been gathered and analyzed, an architecture that is the most robust against the different outcomes of this science must be selected. In addition, completeness is an important metric for comparing different TPF designs and it also gives some insight into the architecture drivers and cost trends. This chapter develops how uncertainty and completeness impact architecture selection to maximize the probability of mission success.

2.1 Nomenclature

The following are definitions used in discussing uncertainty and completeness:

p	Probability of finding planet(s) of interest (POI) within a sample of stars
N_s	Total number of stars in a volume of space
R	Radius of volume of space
$N_{S/\oplus}$	Total number of stars with POI within a volume of space
$\eta_\oplus$	Fraction of Total stars that have POI
η_u	Fraction of Total stars we think have planets of interest
θ_i	Inner habitable zone angular distance (half angle)
θ_{iwd}	Inner working angular distance (half angle)
θ_o	Outer habitable zone angular distance (half angle)
θ_{res}	System angular resolution (full angle)

2.2 Uncertainty

2.2.1 Introduction to $\eta_\oplus$ and η_u

The mission success of extrasolar planet detection is impacted by $\eta_\oplus$, the fraction of total stars that have planet(s) of interest, POI(s). If the value of $\eta_\oplus$ is too small, then there is a low probability of a successful detection due to a finite mission life. But, even if $\eta_\oplus$ is small, precursor science can aid the process by determining which stars to look at. There are two separate issues to consider. The first is how many stars TPF must detect in order to find an Earth-like planet. The second is how far TPF must be able to look in order to see the "right" stars, which are F, G, and K type stars since they are most likely to harbor POI [12]. To clarify, a star with multiple planets of interest is regarded with equal success value as a star with only one planet of interest.

The value of $\eta_\oplus$ is fixed by nature and regardless of the present state of knowledge, there exists some finite number of stars that have POI. To deal with the uncertainty in $\eta_\oplus$ is the concept of η_u, which is defined as the fraction of total stars we think have planets of interest. This provides an upper bound for $\eta_\oplus$ and by its definition, η_u must vary between the value of $\eta_\oplus$ and 1

$$\eta_\oplus \leq \eta_u \leq 1 \tag{2.1}$$

High uncertainty corresponds to η_u equal to one since with no knowledge of $\eta_\oplus$, TPF will look at all stars. As uncertainty decreases η_u approaches $\eta_\oplus$. It is assumed that only the "right" stars are going to be sampled. Then the probability, p, of finding a POI within a sample of stars is

$$p = \frac{\eta_\oplus}{\eta_u} \tag{2.2}$$

With no a priori knowledge, or no precursor science, this probability is simply $\eta_\oplus$ since η_u is one. However, with complete knowledge the probability could equal one. This scenario would mean that the precursor science is so well developed that the TPF

scientists know which stars have extrasolar planets. For example, if only one star in a thousand has a POI ($\eta_\oplus$ = 0.001), but precursor science is able to determine exactly which star has a POI, then TPF only needs to observe that one star with a probability of one of detecting a POI. However, the second issue comes into play since that one star may still be very far away.

Although η_u factors into how many stars TPF must search, it does not affect how far TPF must look. Assuming stars are uniformly distributed, the total number of stars with Earth-like planets in a volume of space is defined as

$$N_{S/\oplus} = \eta_\oplus N_S = \eta_\oplus \frac{4}{3}\pi R^3 n_S \tag{2.3}$$

where n_s is the volumetric star density and R is the distance to the furthest star, which can be determined from Equation (2.3)

$$R = \left(\frac{3N_{S/\oplus}}{\pi n_S \eta_\oplus} \right)^{1/3} \tag{2.4}$$

An earlier example assumed perfect knowledge, (resulting in p = 1), however another possible scenario is that precursor science provides knowledge that yields an η_u of 0.01. In this case, there is a probability of 0.1, or 10% chance, that the stars TPF surveys (based on precursor science) will have a planet. This means that more than one star needs to be surveyed and most likely a reasonable number for stars needs to be surveyed for a successful detection. Once again, the issue becomes that TPF may have to look farther in order to obtain a large enough sample size and the farther TPF is required to image, the longer the baseline and integration time.

2.2.2 Effects of η_u

Sampling statistics can be applied to understand the likelihood of a planetary detection using precursor science. For a large sample size N, the sampling statistics approach a Poisson distribution. The Poisson distribution is commonly used to model the number of

occurrences or successes of some phenomenon in a specified unit of space or time. In this case, the Poisson distribution is used to model the number of stars with POI in a specified volume of space. This volume of space has a sufficiently large enough sample size. In other words, the number of stars to survey is large.

The probability of k successes, $P(k)$, given N number of samples is

$$P(k) = \frac{\lambda^k}{k!} e^{-\lambda} \quad , \quad \lambda = pN \tag{2.5}$$

where λ is the mean success rate; that is, the average number of successes per N samples. Given N samples and k successes, the most likely value of p is k/N. The uncertainty in λ is smaller with fewer successes. An example of the Poisson distribution is shown in Figure 2.1. Applied to planetary detection, N is the number of stars surveyed, k is the number of stars with possible POI determined by precursor science, and λ is the expected number of successes by TPF. This assumes that precursor science only surveys a subset of the TPF starlist.

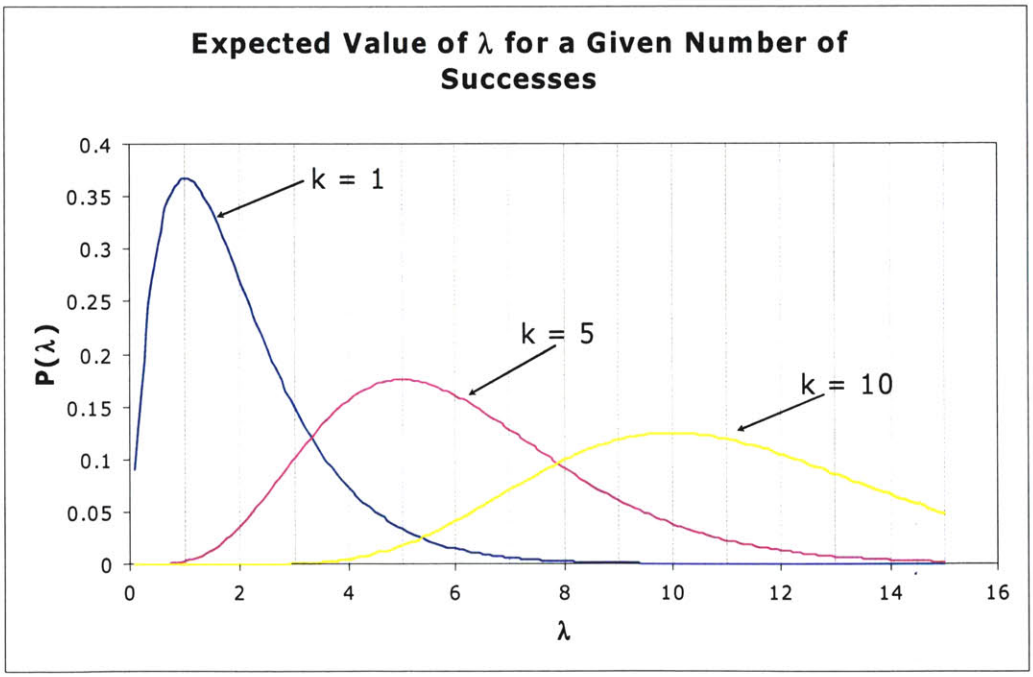

Figure 2.1 Example Poisson distribution

If only F,G, and K type stars are assumed likely to have planets of interest, then currently our estimate at η_u is

$$\eta_u = \frac{N_{F-G-K}}{N_{All}} \tag{2.6}$$

where N_{All} is all the stars in a volume V and is seen in Figure 2.2, which depicts $\eta_\oplus$ as a subset of stars in η_u. As uncertainty decreases, the area of η_u approaches the area of $\eta_\oplus$. The following is an example of an application of the Poisson process model. If precursor science surveys 100 F-G-K stars and identifies two stars with potential POI, then the most likely value of λ for the sample is 2, and $p = \frac{1}{50}$. This could be the result of a first precursor mission; however, additional precursor science and theory could yield additional information.

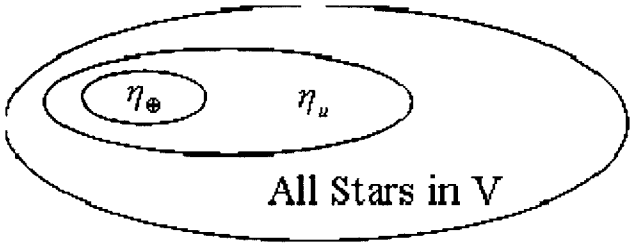

Figure 2.2 Pictorial depiction of $\eta_\oplus$ and η_u in the set of all stars

There are two likely scenarios that can occur. First, if a notable correlation is made, then η_u can be reduced, and p increased. An example of this would be a discovery that all favorable stars are G-type. The second scenario is that the search cannot be made more selective and η_u cannot be reduced. Instead what is known is the p associated with the current strategy, which has an expected value of

$$p = \frac{\eta_\oplus}{\eta_u} \leq 0.02 \tag{2.7}$$

Once the value of p is determined, it can be used to understand how potentially successful a mission is given the number of stars surveyed. If P_f is the likelihood of failing to find any planets in the next sample set, the number of stars or samples needed is

$$N_{samples} = -\frac{1}{p}\ln(P_f) \tag{2.8}$$

Given p, one can then determine the number of additional samples that must be taken for a given likelihood of failure. For example, with the current value of p = 0.02, a likelihood of 1% for failing to find any planets of interest would mean the mission would have to survey greater than 230 stars. If it is eventually determined that there is a reason why only these $\frac{1}{50}$ stars has a POI, then the value of η_u can be reduced by a factor of $\frac{1}{50}$, and future search strategies can be more selective.

2.2.3 When Does η_u Change

Processed precursor science mission data can result in a change of η_u. Knowledge gained from data processing can lag launch dates by 2-3 years [13]. An example of this time lag can be seen from the Keck Interferometer. It achieved first light in December, 2001, and then published its first science observation in July 2003, a delay of 33 months. Keck is one of the many missions which could give TPF useful precursor science data. Keck plans to demonstrate exo-zodiacal dust characterization and nulling and can detect Uranus size planets around stars up to sixty light years away. Figure 2.3 shows other projects which could give TPF useful precursor science data with their approximate launch years. Projects before the intended architecture selection date include SOFIA, which will conduct science on proto-planetary disks and planet formation in nearby star systems, and Spitzer, which will image brown dwarfs, super-planets, and dust disks surrounding nearby stars. Missions after the architecture selection can also help decrease uncertainty. An example is Kepler, which plans to perform indirect planet detection.

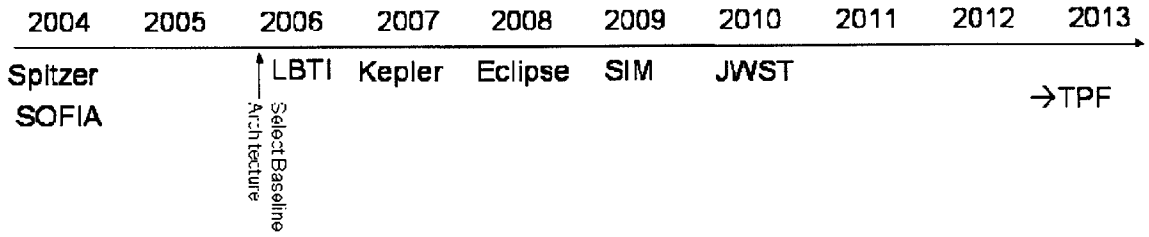

Figure 2.3 Precursor mission timeline

An interesting case study regarding the correlation between Iron-rich stars and large planets [14] has been conducted investigating how η_u changes with significant precursor science and observation. Fischer and Valenti surveyed 754 nearby sun-like stars to determine the presence of a Jupiter-sized planet and took the spectrum of each star to determine the amount of Iron present in the star. The stars harbored 61 planets and data suggested that the metal-rich stars were more likely to develop planetary systems. A near linear relationship between the amount of Iron in a star and the existence of a planet in the star system was found and is seen in Figure 2.4. This data can affect η_u for large planets around sun-like stars assuming it is representative of an arbitrarily large data set.

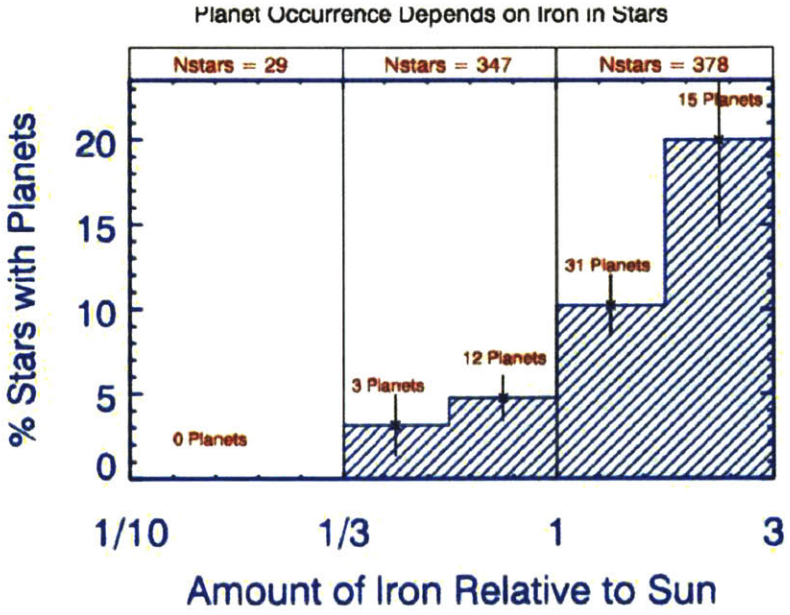

Figure 2.4 Relationship of metal rich stars and planetary occurrences [14]

Stars with $\frac{1}{10}$ to $\frac{1}{3}$ the amount of Iron relative to the Sun appear to have no detectable planets. Therefore, if one is looking for large planets, then one would not survey a star that has small amounts of iron compared to the Sun. In the case of η_u for large planets it can be reduced as

$$\eta_u^{new} = \eta_u^{old}\left(1-\frac{29}{754}\right) \tag{2.9}$$

where η_u^{new} is the value of η_u after taking into account the relationship planetary metal rich stars and planetary occurences. The data also shows that a greater percentage of stars exist when the amount of Iron relative to the Sun is higher (1 to 3 times). It is possible to incorporate weighted probabilities to aid planet detection, however no such algorithm has been developed yet.

2.3 Completeness

The goals of this section are to determine the completeness of a TPF design and to determine a cost model trend for varying baselines. The completeness is the percentage of the habitable zone searched given a set of stars. Completeness is a metric that describes the habitable zone coverage. A completeness of one means the entire habitable zone is searched for all stars. The calculation of completeness begins with an estimate for the potential suitable star distribution, n_s, as seen from Earth

$$n_s = \frac{a_s}{R^{\alpha}} \tag{2.10}$$

where R is the distance from the Earth in parsecs, and α and a_s are constants to be determined later. The units of n_s are stars per cubic parsec. For a uniform density, as one would expect for large volumes of space, α equals 0. A more accurate equation for n_s could include a summation of $\frac{a_{s_i}}{R^{\alpha_i}}$ terms. A single term, which is currently used, is useful in this analysis for simplicity and could represent the dominate term from a full summation equation.

The estimate for the potential planet distribution within a star system is given by

$$n_p = \frac{a_p}{r} \tag{2.11}$$

where r is the distance from the star in astronomical units (AU) and a_p is a constant to be determined later.

Integrating Equation (2.10), the number of suitable stars, N_p, from R_{min} to R_{max} is

$$N_s = 4\pi \int_{R_{min}}^{R_{max}} n_s R^2 dR \tag{2.12}$$

where the differential element is a spherical shell, hence the $4\pi R^2 dR$ term.

Similarly, N_p is the number of potential planets within a star system is given by

$$N_p = \int_{r_i}^{r_o} n_p dr \tag{2.13}$$

where integration occurs between the inner habitable zone, r_i, and the outer habitable zone, r_o.

Finally, the science productivity, which is defined as the number of potential planets among suitable stars, is determined by

$$I = 4\pi \int_{R_{min}}^{R_{max}} \int_{r_i}^{r_o} n_s n_p R^2 dr dR \tag{2.14}$$

The two integrals cannot be taken independently and are multiplied because the limits of integration of the two integrals are coupled by the system resolution. If the resolution of the system is too close to the star, stellar leakage prohibits the ability to detect planets anywhere around the star. For this reason, an 'inner working distance' is defined, as shown in Figure 2.5. For a fixed baseline system, this problem occurs for stars that are closest to the Earth, and effectively sets a minimum distance that a star can be from Earth to allow for planet detection. For stars that are just beyond this minimum, the resolution of the system falls between the inner working distance and the inner habitable zone, as shown by the dotted circle 'A' in Figure 2.5. In this case the entire habitable zone is investigated. As stars that are farther away are viewed the resolution falls outside the inner habitable zone (shown by dotted circle 'B'), and only portions of the habitable zone outside the resolution limit are seen. Since only a partial viewing of the habitable zone can occur, potential planets can miss detection by a fixed baseline system. Eventually, at greater distances, the resolution equals the angular extent of the outer habitable zone and

none of the habitable zone can be searched. When the resolution reaches the outer habitable zone, an upper limit on stellar distances that can be investigated is established.

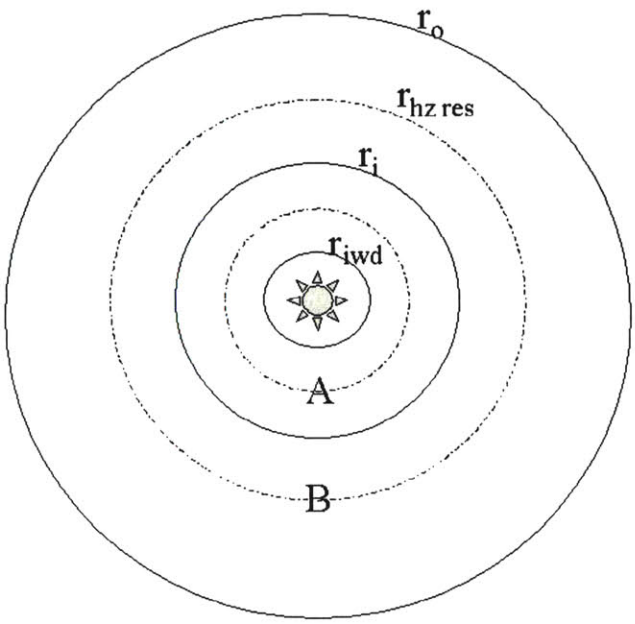

Figure 2.5 Regions around a star

There are two different cases, to determine the potential number of observable planets, which are illustrated in Table 2.1. Case 1 adds up the potential number of planets in the habitable zone of nearby stars, for which the habitable zone is fully resolved. Case 2 adds up the potential number of planets of farther stars, for which the habitable zone is only partially resolved. For Case 2 the minimum resolvable distance of the habitable zone is defined as r_{hz_res}. It is assumed that all star systems are viewed face on.

Table 2.1 Two Cases for determining the potential number of observable planets

Case 1 Closer stars, view habitable zone entirely where $2\theta_{iwd} \leq \theta_{res} \leq 2\theta_i$	$I_1 = \int_{R_{min}}^{R_{max}} 4\pi \int_{r_i}^{r_o} \frac{a_s}{R^\alpha} \frac{a_p}{r} R^2 dr dR$ where $R_{min} = \frac{2r_{iwd}B}{\lambda}$ and $R_{max} = \frac{2r_iB}{\lambda}$
Case 2 Farther stars, view habitable zone incompletely where $2\theta_i \leq \theta_{res} \leq 2\theta_o$ and $r_i \leq r_{hz\_res} \leq r_o$	$I_2 = \int_{R_{min}}^{R_{max}} 4\pi \int_{r_{hz\_res}}^{r_o} \frac{a_s}{R^\alpha} \frac{a_p}{r} R^2 dr dR$ where $R_{min} = \frac{2r_iB}{\lambda}$ $R_{max} = \frac{2r_oB}{\lambda}$ and $r_{hz\_res} = \frac{\lambda R}{2B}$

From these two cases, completeness is defined as

$$C = \frac{I_1 + I_2}{N_s N_p} \tag{2.15}$$

where N_s and N_p are the total number of suitable stars and potential planets per star respectively.

The science productivity terms, I_1 and I_2 are determined as functions of α

$$I_1 = \begin{cases} 4\pi a_s a_p \ln(\frac{r_o}{r_i}) \frac{1}{3-\alpha} (\frac{2r_{iwd}B}{\lambda})^{3-\alpha} ((\frac{r_i}{r_{iwd}})^{3-\alpha} - 1) & \alpha \neq 3 \\ 4\pi a_s a_p \ln(\frac{r_o}{r_i}) \ln(\frac{r_i}{r_{iwd}}) & \alpha = 3 \end{cases} \tag{2.16}$$

$$I_2 = \begin{cases} 4\pi a_s a_p \frac{1}{(3-\alpha)^2} ((2p)^{3-\alpha} - (2q)^{3-\alpha} - (2q)^{3-\alpha}(3-\alpha)\ln(\frac{p}{q})) & \alpha \neq 3 \\ 2\pi a_s a_p \ln(\frac{r_o}{r_i})^2 & \alpha = 3 \end{cases} \tag{2.17}$$

where $p = \frac{r_o B}{\lambda}$ and $q = \frac{r_i B}{\lambda}$. Appendix A illustrates these calculations in greater detail.

To finish the calculation for completeness, N_s and N_p are determined by normalizing their respective distribution such that the distribution integrates to 1. For N_s,

$$\int PDF_{N_s} dR = \frac{1}{N_s} \int_{R_{min}}^{R_{max}} 4\pi \frac{a_s}{R^\alpha} R^2 dR = 1 \tag{2.18}$$

from which N_s is solved for over the range $R_{min} = \frac{2Br_{iwd}}{\lambda}$ to $R_{max} = \frac{2Br_o}{\lambda}$.

$$N_s = \begin{cases} \frac{4\pi a_s}{3-\alpha} (\frac{2r_{iwd}B}{\lambda})^{3-\alpha} ((\frac{r_o}{r_{iwd}})^{3-\alpha} - 1) & \alpha \neq 3 \\ 4\pi a_s \ln(\frac{r_o}{r_{iwd}}) & \alpha = 3 \end{cases} \tag{2.19}$$

In similar fashion, the PDF of N_p is

$$\int PDF_{N_p}\,dr = \frac{1}{N_p}\int_{r_i}^{r_o}\frac{a_p}{r}\,dr = 1 \tag{2.20}$$

yielding

$$N_p = a_p \ln(\frac{r_o}{r_i}) \tag{2.21}$$

In the case of our solar system, one can make an estimate for the constant a_p, where $N_p = 3$ and $r_o = 6\ r_i$, corresponding to an inner habitable zone of approximately 0.5 AU and an outer habitable zone of approximately 3.0 AU.

$$a_p = \frac{3}{\ln(6)} = 1.67 \tag{2.22}$$

Multiplying N_s and N_p yields

$$N_p N_s = \frac{4\pi a_s a_p}{3-\alpha}\ln(\frac{r_o}{r_i})(\frac{2r_{iwd}B}{\lambda})^{3-\alpha}((\frac{r_o}{r_{iwd}})^{3-\alpha}-1) \tag{2.23}$$

and calculating the two components of completeness yields

$$I_1 = \frac{I_1}{N_p N_s} = \begin{cases} \dfrac{((\frac{r_i}{r_{iwd}})^{3-\alpha}-1)}{((\frac{r_o}{r_{iwd}})^{3-\alpha}-1)} & \alpha \neq 3 \\ \dfrac{\ln(\frac{r_i}{r_{iwd}})}{\ln(\frac{r_o}{r_{iwd}})} & \alpha = 3 \end{cases} \tag{2.24}$$

$$I_2 = \frac{I_2}{N_p N_s} = \begin{cases} \dfrac{1}{(3-\alpha)\ln(\frac{r_o}{r_i})}(\frac{r_i}{r_{iwd}})^{3-\alpha}\dfrac{((\frac{r_o}{r_i})^{3-\alpha}-1-(3-\alpha)\ln(\frac{r_o}{r_i}))}{((\frac{r_o}{r_{iwd}})^{3-\alpha}-1)} & \alpha \neq 3 \\ \dfrac{1}{\ln(\frac{r_o}{r_i})\ln(\frac{r_o}{r_{iwd}})} & \alpha = 3 \end{cases} \tag{2.25}$$

From Equations (2.24) and (2.25), completeness can be determined for various values of α as a function of the ratio between the inner working distance and the inner habitable

zone, which is shown in Figure 2.6. This is the completeness for a fixed baseline design and represents the minimum completeness for a tunable baseline. A tunable baseline has the ability to achieve a completeness of one, for any choice of α. Additional accuracy can be determined by using a more suitable, higher fidelity star model.

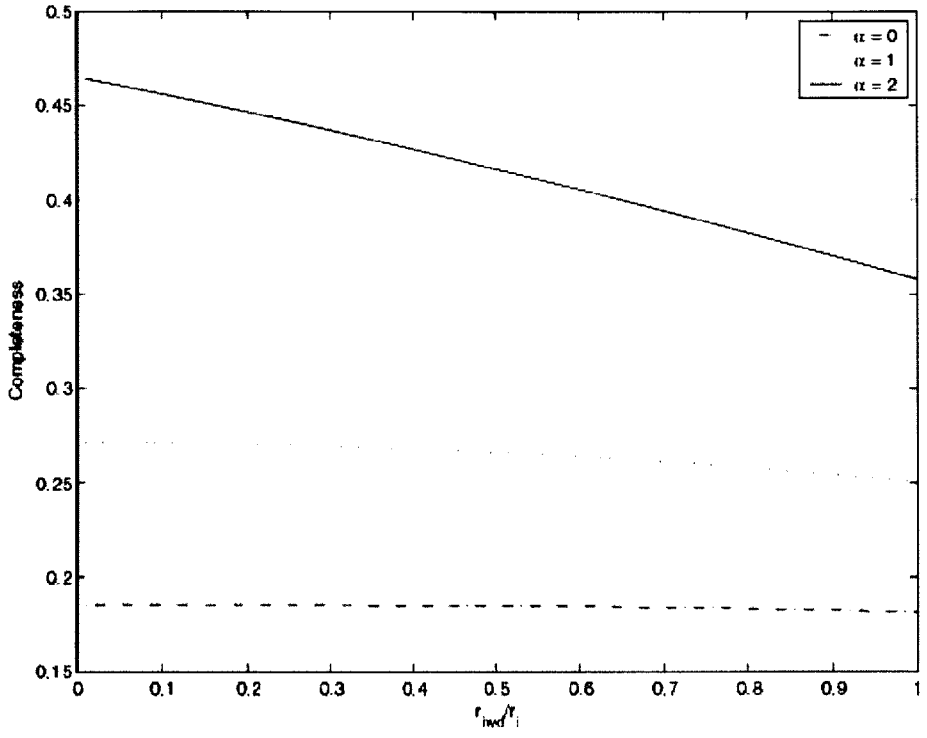

Figure 2.6 Completeness vs. $\frac{r_{iwd}}{r_i}$ for different α

2.3.1 Cost Model

The total aperture cost for TPF is estimated as the number of apertures, n_a times the cost of each aperture, which is a function of the aperture diameter, D_a,

$$\$ = n_a \$_a D_a^{\gamma} \tag{2.26}$$

The cost efficiency is defined as the total aperture cost over the science productivity, $I_1 + I_2$. This analysis does not assume a variable integration time. The size of each aperture is designed with a sufficient signal to noise ratio (SNR) to detect potential

planets at the farthest star system. Beyond this farthest star system, the SNR drops below the required amount to detect potential planets and the system resolution falls outside the outer habitable zone. The total signal collecting area is

$$A = n_a \frac{\pi D_a^2}{4} = (a_{SNR} R^2)^{\frac{1}{\beta}} \tag{2.27}$$

where $a_{SNR} \approx \frac{A^\beta}{R^2}$ and β is a constant to be determined later. Therefore the aperture diameter is described by

$$D_a = \frac{2(a_{SNR})^{\frac{1}{2\beta}} R^{\frac{1}{\beta}}}{\sqrt{n_a \pi}} \tag{2.28}$$

where the farthest star dictates $R_{max} = \frac{2r_o B}{\lambda}$. From the previous section, $I_1 + I_2$ was determined so that

$$\frac{\$}{I_1 + I_2} = \frac{n_a \$_a (\frac{2}{\sqrt{n_a \pi}} (a_{SNR})^{\frac{1}{2\beta}} (\frac{2r_o B}{\lambda})^{\frac{1}{\beta}})^\gamma}{\frac{4\pi a_s a_p B^{3-\alpha}}{3-\alpha} [\ln(\frac{r_o}{r_i})(\frac{2r_{iwd}}{\lambda})^{3-\alpha}((\frac{r_i}{r_{iwd}})^{3-\alpha} - 1) + \frac{1}{3-\alpha}(\frac{2r_i}{\lambda})^{3-\alpha}(\frac{r_o}{r_i}^{3-\alpha} - 1 - (3-\alpha)\ln(\frac{r_o}{r_i}))]} \tag{2.29}$$

for $\alpha \neq 3$. Taken as a function of baseline, the cost per potential planet is

$$\frac{\$}{I_1 + I_2} \approx B^{\frac{\gamma}{\beta} - 3 + \alpha} \tag{2.30}$$

The cost model trend is largely impacted by β. For example, for a uniform density of stars ($\alpha = 0$) with $\beta = \frac{1}{2}$, if the functional dependence of aperture cost on diameter is greater than the $\frac{3}{2}$ power, then it is more costly per potential planet found to go to longer baselines, from the standpoint of apertures only. Since this scaling law is thought to be $\gamma = 2.7$ [15], this indicates that cost per potential planet detection goes as $B^{2.4}$. This gives no indication as to the minimum baseline necessary to achieve a given number of planet detections. However, if $\beta = 1$, than the cost per potential planet detection goes as $B^{-0.3}$, so it will become cheaper per potential planet to go to longer baselines. This can be achieved using a longer fixed baseline, if permissible by launch constraints, etc. It is also

possible that a variable baseline system has the ability to reap the benefits of going to longer baselines.

2.3.2 Completeness Baseline Trends

Given a fixed mission lifetime, there are a limited number of stars that can be viewed for planet detection. The integration time required for planet detection about a given star is fixed regardless of the habitable zone coverage, or completeness. Therefore time is most efficiently spent viewing stars which have 100% completeness or the highest completeness otherwise. A fixed baseline system will have a completeness of one over the closest stars. However, stars which are farther away will have partial coverage, and the number of these stars increase with distance, as seen in Figure 2.7 [16]. Stars with 100% coverage occur in a relatively narrow distance band, where the left end of the band is determined by the star glint and instrument properties and the right end of the band is determined by the point at which resolution equals the inner habitable zone. Figure 2.7 also shows an example of such a band. Additional stars can be included by either looking closer or farther out. However, a larger number of stars can be included by looking farther out, but at the expense of longer integration times.

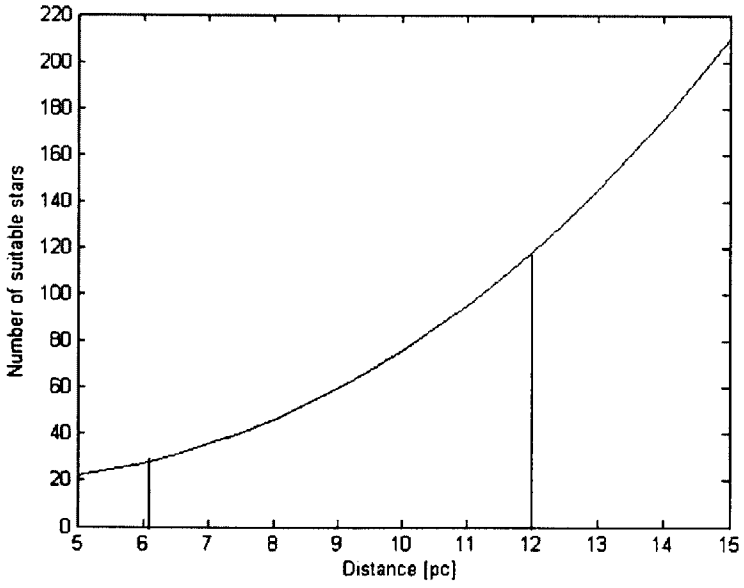

Figure 2.7 Theoretical star distribution [16]

As a reminder, the fraction of total stars that have a planet of interest is $\eta_{\oplus}$. If $\eta_{\oplus}$ is small, then the coverage band may not be a large enough sample size to detect a potential planet. To increase the coverage band, a variable baseline can be utilized, but the question becomes, how much variability is necessary.

In order to gain insight into the degree of baseline variability, the number of potential planets for a fixed baseline system, or Structurally Connected Interferometer (SCI), must first be determined. The number of planets detected is outlined in Table 2.1 and is used as a starting point for calculation. Unity completeness is used to set a common metric for comparing variable and fixed baseline systems. Case 1 from Table 2.1 is used since it has a completeness of one and the following has calculated the inner integral for the SCI system.

$$I_{SCI}\big|_{C=1} = 4\pi \int_{\frac{2\eta_{iwd}B_{SCI}}{\lambda}}^{\frac{2\eta B_{SCI}}{\lambda}} a_p a_s R^{2-\alpha} \ln(\frac{r_o}{r_i}) dR \tag{2.31}$$

Continuing to integrate leads to the number of potential planets for the SCI system for the baseline B_{SCI}.

$$I_{SCI}\big|_{C=1} = \frac{4\pi a_p a_s}{3-\alpha} \ln\left(\frac{r_o}{r_i}\right)\left(\frac{2B_{SCI}}{\lambda}\right)^{3-\alpha}\left(r_i^{3-\alpha} - r_{iwd}^{3-\alpha}\right) \tag{2.32}$$

The Separated Spacecraft Interferometer (SSI), also called a Formation Flown Interferometer (FFI), follows a similar procedure as the SCI case, however now the baseline can be varied between B_{min} and B_{max}.

$$I_{SSI}\big|_{C=1} = 4\pi \int_{\frac{2\eta_{iwd}B_{min}}{\lambda}}^{\frac{2\eta B_{max}}{\lambda}} a_p a_s R^{2-\alpha} \ln(\frac{r_o}{r_i}) dR \tag{2.33}$$

It should be noted that since the baseline is not the exact same as the SCI case (and thus the R_{min} and R_{max} are different), it is possible that the SSI system has a different set of stars from the SCI system. However since there is no current knowledge over any of the

set of stars, the assumption is made that they are similar. Continuing to integrate leads to the number of potential planets for the SSI system for a baseline of range B_{min} to B_{max}.

$$I_{SSI}\big|_{C=1} = \frac{4\pi a_p a_s}{3-\alpha} \ln\left(\frac{r_o}{r_i}\right)\left(\frac{2}{\lambda}\right)^{3-\alpha}\left((r_i B_{max})^{3-\alpha} - (r_{iwd} B_{min})^{3-\alpha}\right) \tag{2.34}$$

To compare the SSI system and the SCI system, the ratio of the two potential planet equations is taken and simplified as

$$\left.\frac{I_{SSI}}{I_{SCI}}\right|_{C=1} = \frac{\left(\frac{B_{max} r_i}{B_{SCI} r_{iwd}}\right)^{3-\alpha} - \left(\frac{B_{min}}{B_{SCI}}\right)^{3-\alpha}}{\left(\frac{r_i}{r_{iwd}}\right)^{3-\alpha} - 1} \tag{2.35}$$

The ratio of potential planets is in terms of the various baselines and the inner habitable zone, r_i, and the inner working distance r_{iwd}. Assuming r_i and r_{iwd} are already set by nature and the instruments, the variable parameters are B_{SCI}, B_{min}, and B_{max}. As an example scenario, the constraints are $B_{min} = B_{SCI} = 100$ m and B_{min} is varied to see how the ratio changes. This result is plotted in Figure 2.8 for $r_i = 0.5$ AU. The smallest inner working distance used is modeled as 1.5 times the diameter of the sun resulting in $\frac{r_i}{r_{iwd}} = 35.7$. If this is the representative inner working distance, then it is only the maximum baseline which needs to be varied in order to achieve a gain in the SSI system over the SCI system. For much higher inner working distances, the SSI system gains by decreasing its minimum baseline.

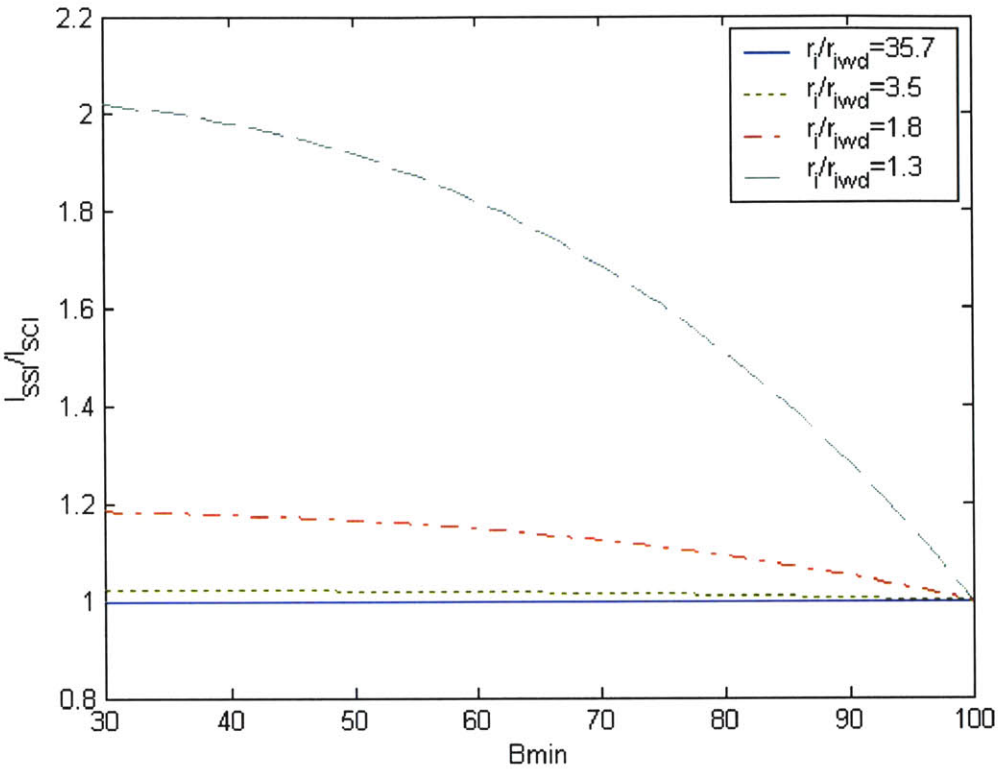

Figure 2.8 Potential planet gain vs. minimum SSI baseline

A further constraint using the SCI and SSI systems mission lifetime, T_L, can also be levied. The integration time for a single star goes as distance squared, R^2, if the exo-zodiacal signal and planet signal dominate the local zodiacal signal. This is shown as follows, where the constant a_{snr} contains all the terms not dependant on R.

$$T_i = \begin{cases} a_{snr} R^2 & \text{Exo-Zodiacal Background, Planet Signal Dominant} \\ a_{snr} R^4 & \text{Local Zodiacal Background Signal Dominant} \end{cases} \tag{2.36}$$

The mission lifetime is the cumulation of the integration times for all the stars systems viewed between R_{min} and R_{max} with a stellar density n_s.

$$T_L = 4\pi \int_{R_{min}}^{R_{max}} n_s T_i R^2 dR \tag{2.37}$$

The mission lifetime for a SCI system, $T_{L_{SCI}}$, is the time it takes to image a set of stars for a baseline B_{SCI}.

$$T_{L_{SCI}}\Big|_{C=1} = 4\pi \int_{\frac{2r_{iwd}B_{SCI}}{\lambda}}^{\frac{2r_iB_{SCI}}{\lambda}} a_p a_{snr} R^{4-\alpha} dR = \frac{4\pi a_p a_{snr}}{5-\alpha}\left(\frac{2B_{SCI}}{\lambda}\right)^{5-\alpha}\left(r_i^{5-\alpha} - r_{iwd}^{5-\alpha}\right) \tag{2.38}$$

In similar fashion, mission lifetime for a SSI system, $T_{L_{SSI}}$, is the time it takes to image a set of stars for a baseline of range B_{min} to B_{max}.

$$T_{L_{SSI}}\Big|_{C=1} = \frac{4\pi a_p a_{snr}}{5-\alpha}\left(\frac{2}{\lambda}\right)^{5-\alpha}\left((r_i B_{max})^{5-\alpha} - (r_{iwd} B_{min})^{5-\alpha}\right) \tag{2.39}$$

Now that two equations for T_L have been obtained, they can be set equal to each other and a relationship between B_{SCI}, B_{min}, and B_{max} can be determined. This is simplified as

$$\frac{B_{max}}{B_{SCI}} = \frac{1}{r_i}\left[r_i^{5-\alpha} - r_{iwd}^{5-\alpha} + \left(\frac{B_{min}}{B_{SCI}} r_{iwd}\right)^{5-\alpha}\right]^{\frac{1}{5-\alpha}} \tag{2.40}$$

Substituting Equation (2.40) into Equation (2.39) leads to a $\frac{I_{SSI}}{I_{SCI}}$ ratio that is function of B_{min} and B_{SCI}

$$\frac{I_{SSI}}{I_{SCI}}\Big|_{C=1} = \frac{\frac{1}{r_{iwd}^{3-\alpha}}\left[r_i^{5-\alpha} - r_{iwd}^{5-\alpha} + \left(\frac{B_{min} r_{iwd}}{B_{SCI}}\right)^{5-\alpha}\right]^{\frac{3-\alpha}{5-\alpha}} - \left(\frac{B_{min}}{B_{SCI}}\right)^{3-\alpha}}{\left(\frac{r_i}{r_{iwd}}\right)^{3-\alpha} - 1} \tag{2.41}$$

As a check, if the baselines of the SCI and SSI are equal, meaning $B_{SCI} = B_{min}$, the result should be unity. Both systems yield the same number of potential planets. The effect of baseline variability is not mathematically intuitive, so Equation (2.41) is graphically shown in Figure 2.9. The inner habitable zone distance used for Figure 2.9 is 0.5 AU. The gain in potential planets by the variable baseline system occurs in the regime where the minimum baseline is smaller than that of the fixed baseline system. As the inner working distance approaches the inner habitable zone the potential planet gain increases in this regime. The variable baseline system allows for more potential planets when

compared to a fixed baseline system of same completeness and same mission lifetimes. To achieve this, the variable baseline system looks at stars which are closer since the minimum baseline must be smaller than the fixed baseline system.

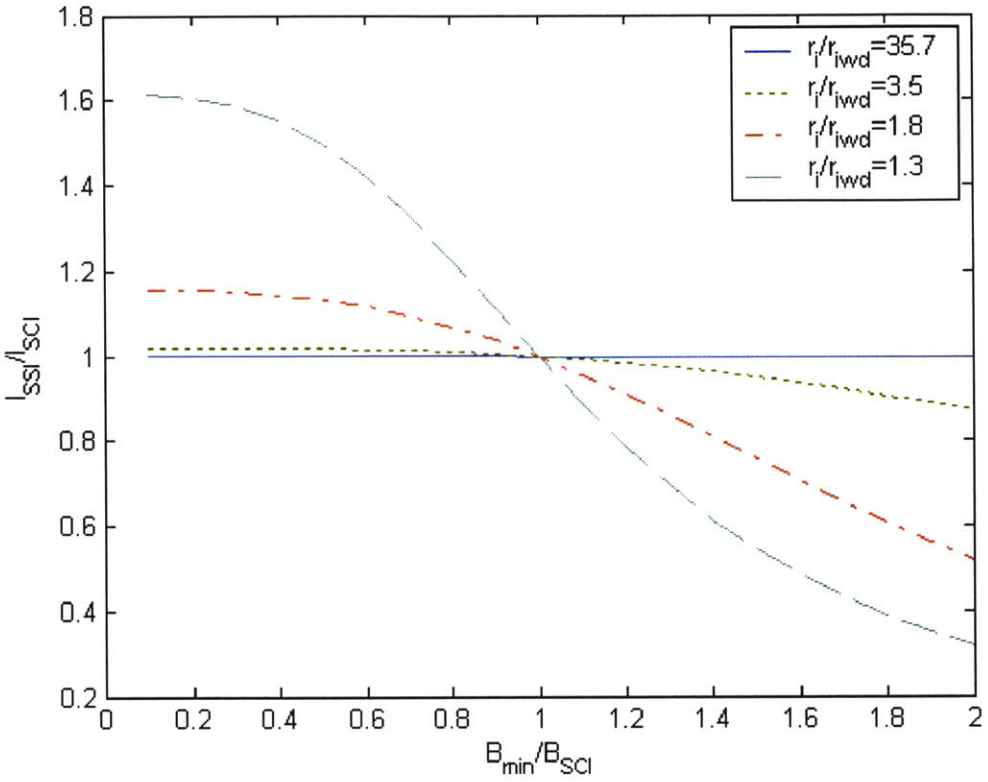

Figure 2.9 Science productivity ratio of SSI and SCI vs. baseline ratio for different inner habitable zone and inner working distance ratios

Figure 2.10 illustrates a problematic region in Figure 2.9. In the right half of Figure 2.9, where $B_{min} > B_{SCI}$, the maximum baseline actually becomes less than the minimum baseline, as seen in Figure 2.10. Additionally, in the upper left quadrant of Figure 2.9, where $B_{min} < B_{SCI}$, B_{max} also is less than the SCI baseline resulting in a very small baseline range. It is possible that the strict mission lifetime constraint allows little flexibility in baseline and constrains it to small bounds.

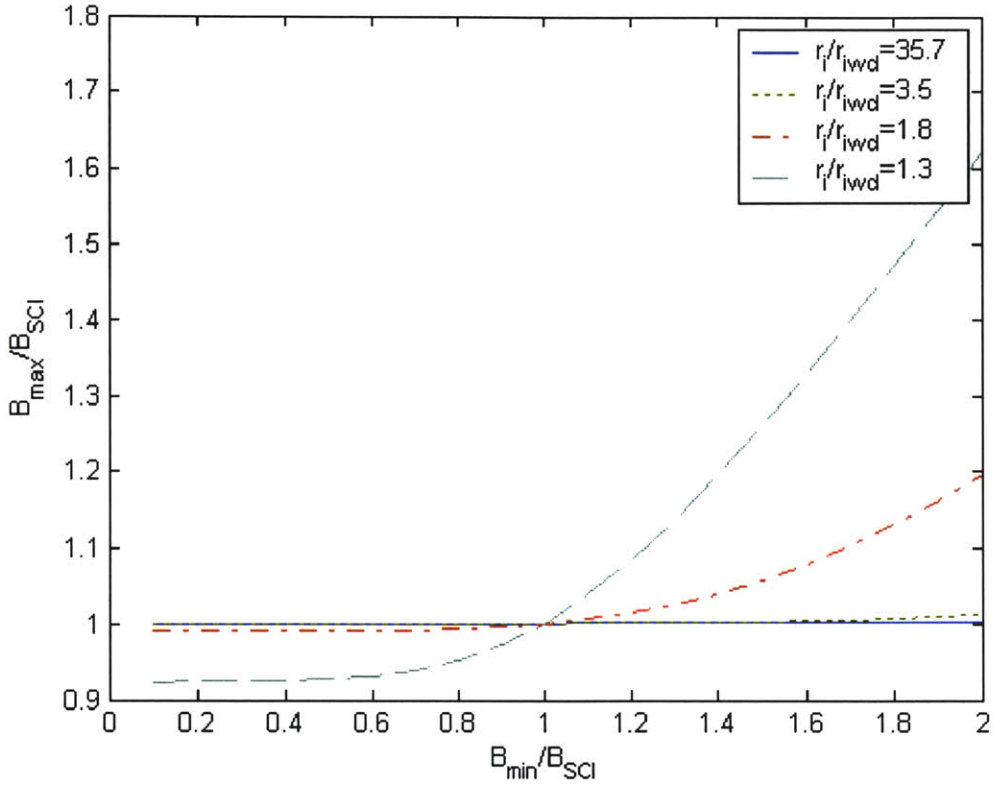

Figure 2.10 Baseline variability for the $\frac{SSI}{SCI}$ ratio

2.4 Fixed vs. Variable Baseline System

One of the aspects of completeness is that the time required for detection about a given star is the same regardless of habitable zone coverage and that less than 100% coverage allows the possibility of missing the detection of an existing planet. Fixed baseline systems will have 100% coverage over some stars, but partial coverage over most as seen in Figure 2.11 for two different fixed baseline systems. Stars with 100% coverage occur in a narrow distance band. A large number of stars can be included in this band by looking farther out, but at the expense of longer integration times. For a fixed mission lifetime, longer integration times can also result in few stars viewed. Higher uncertainty in which stars should be observed favors looking closer, since a larger sample set can be viewed over the mission lifetime.

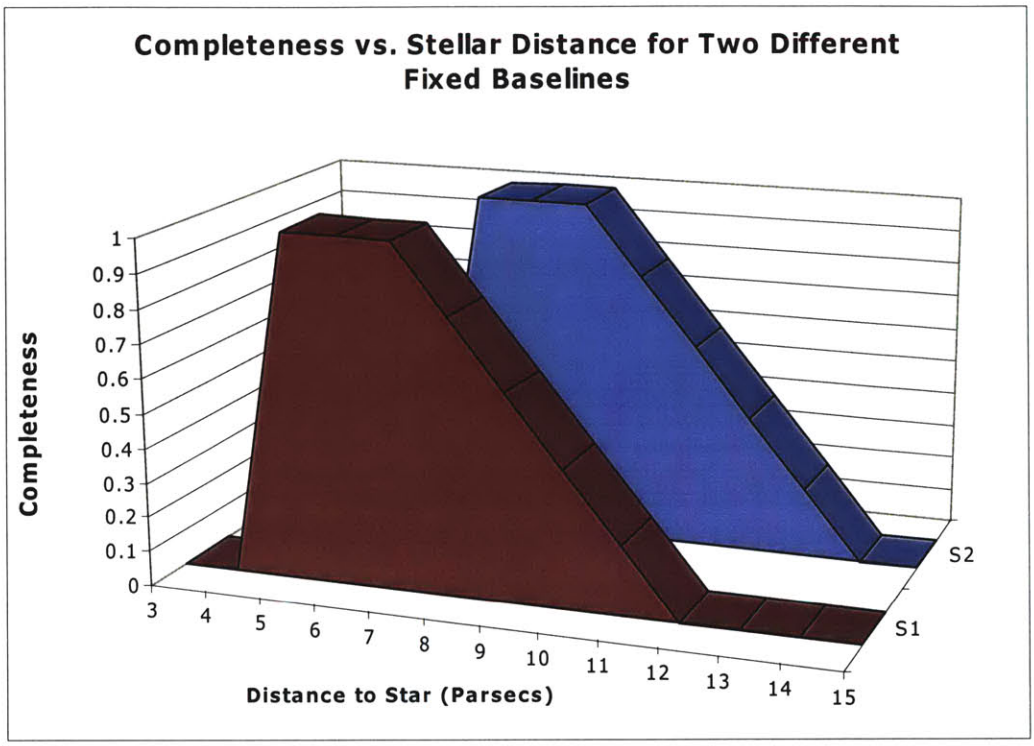

Figure 2.11 Completeness for two fixed baseline systems

An example of uncertainty applied to fixed baseline systems can be shown in Table 2.2. Shown are three fixed baseline systems which can view a different number of stars. BL 1 has the shortest baseline and BL 3 has the longest baseline. The number of viewable stars over the mission is the effect of distance on integration time. There are two notional cases shown in Table 2.2.

The first case is for $\eta_{\oplus} = 0.01$ and for no precursor knowledge ($\eta_u = 1$). As the baseline for the fixed system increases, going from BL 1 to BL 3, the number of planets that are detectable increase since there are a greater number of viewable stars. However for a fixed mission lifetime, the probability of not detecting a planet actually increases for the longer fixed baseline systems since fewer stars are viewable due to excessive integration times.

Table 2.2 Example of uncertainty applied to three fixed baseline systems

	BL 1	BL 2	BL 3
# of stars in ΔR (C=1)	100	500	1000
# viewable over mission	50	40	30
# of planets if $\eta_{\oplus} = 0.01$	1	5	10
P_f if $\eta_{\oplus} = 0.01$, $\eta_u = 1$	60%	67%	74%
# of planets if $\eta_{\oplus} = 0.001$	0	0	1
P_f if $\eta_{\oplus} = 0.001$, $\eta_u = .01$	100%	100%	5%

The second case, Rows 5 and 6 of Table 2.2, shows the effect of an $\eta_{\oplus}$ that is much smaller ($\eta_{\oplus}$ = 0.001), but with a reduced uncertainty of η_u = 0.01 due to precursor science. In this scenario, the number of stars accessible by a shorter fixed baseline system may be insufficient to have POI. A longer fixed baseline system can access POI and with additional knowledge there is a significant decrease in the probability of not finding a planet (P_f).

In summary of this example, longer fixed baseline systems are less likely to find POI if η_u is large, but may be the only chance of finding them if precursor missions reduce η_u. Because precursor science data will lag the architecture downselect there is no way to know whether a shorter or longer fixed baseline is better.

Unlike a fixed baseline system, a variable baseline allows for observational completeness regardless of the stellar distance as seen in Figure 2.12. The variable baseline system can be adapted to the following two cases in uncertainty. If η_u turns out to be relatively large, operating at shorter baselines allows for many more observations to be made over the mission lifetime, increasing science throughput. If η_u turns out to be relatively small, operating at longer baselines grants access to a much larger volume of stars, increasing science throughput. These very large baselines may be necessary to access a sufficient volume of space to insure the stars with POI can be observed. The longer integration times make the need for a tunable baseline (to achieve full completeness) even more

important. Independent of technological issues, a formation flown variable baseline system appears to offer the lowest risk of science return.

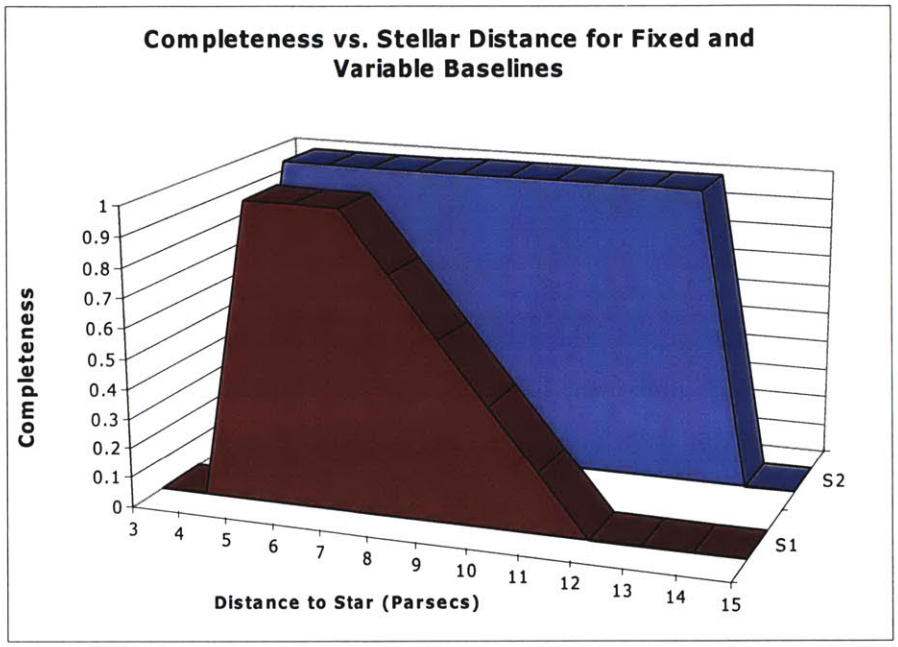

Figure 2.12 Completeness for a fixed and variable baseline system

2.5 Architecture Conclusions

Without precursor science there is a high uncertainty in finding POI, however even if η_u is very small, precursor science has the ability to upper bound η_u in such a way that one can be smarter about which stars to observe. A large uncertainty in η_u drives a mission toward a desire for more observations, and therefore shorter baselines. The danger lies in the possibility that the limited number of stars accessible by a shorter fixed baseline system may not have access to stars with any POI. Larger fixed baseline systems allow for more stars to be accessed, but without good precursor knowledge, one cannot effectively limit the search. The problem is that the architecture downselect occurs before it will be known whether searching closer or farther is a better approach. The most robust solution is to make the baseline variable, over a relatively large extent, allowing operation in either mode. This supports a formation flown system as providing the least science risk.

Chapter 3

EMFF MULTI-SPACECRAFT DESIGNS

The previous chapter elaborated on the benefits of a tunable baseline system, which can be achieved by formation flying. This chapter introduces the concept of Electromagnetic Formation Flight applied to multiple satellite arrays. Starting with the forces and torques that can be achieved to actuate EMFF spacecraft in relative motions, we will determine the agility capabilities of EMFF for two spacecraft in circular trajectories. This simple array can be expanded by adding additional EMFF spacecraft. Another method of sizing arrays will use the concept of mission efficiency. This case will culminate by looking at the effects of *N*-spacecraft in an array. Linear trajectories using a non-linear simulator will also be described. Distributing mass among multiple spacecraft to create a mother/daughter type relationship is one of the recurring ideas in this chapter.

3.1 EMFF Background

The simplest method of modeling the forces and torques created by EMFF satellites is to approximate the coils as permanent bar magnets. This is called the far field model and is applicable at distances far enough from the satellite that the electromagnetic coils appear as dipoles. At this distance, the dipole field structure for permanent bar magnets and electromagnetic dipoles are the same. Using the far field model, we can imagine two orthogonal coils represented by a pair of magnets, which have the ability to turn their fields on or off, located in a two dimensional plane as seen in Figure 3.1.

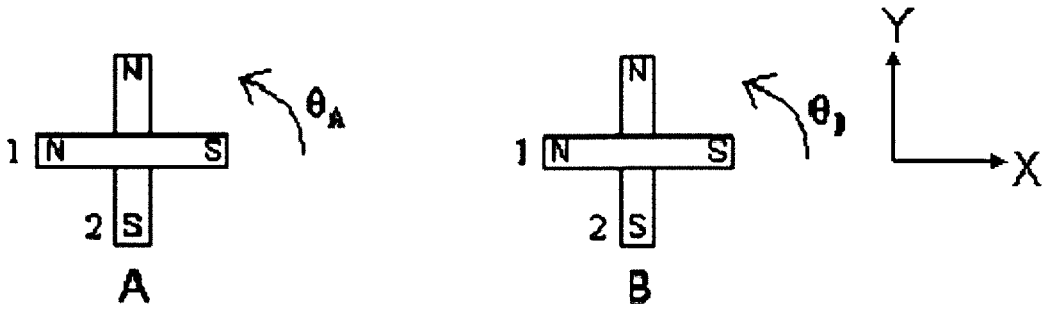

Figure 3.1 Far field magnetic model

To create an attractive force, magnet one from both vehicle A and B is turned on, at which point the south or minus polarity from A is attracted to the north or plus polarity of B. The north of A is also repelled from the north of B and the south repelled from the south of B. However, the attractive component of force is much stronger resulting in a net attraction and movement along the x-axis. To create a net repulsive force, the polarity of one of the magnets is reversed.

Movement in the y-direction is achieved when the magnetic field generated by one vehicle is orthogonal to the field generated by the other vehicle. For example, by enabling only magnet two on A and magnet one on B while all others are turned off. In this case the plus polarities repel each other causing the magnets to turn in the counter-clockwise direction. In addition the minus polarities repel although this effect is weaker and in the opposite direction. The net effect is a counter-clockwise torque seen on both A and B plus a shear force in the positive y-direction on A and a shear force in the negative y-direction on B. By using a reaction wheel to provide a torque in the clockwise direction, a net shearing motion can be created while maintaining constant inertial angle in each vehicle.

The permanent magnet model works well to understand the various degrees of freedom. EMFF is implemented in three dimensions by using three orthogonal electromagnetic coils which act as dipole vector components and allow a magnetic dipole to be created in any direction by varying the current through the coils. A reaction wheel assembly with

three orthogonal wheels is also necessary to provide the counter torques for attitude maintenance.

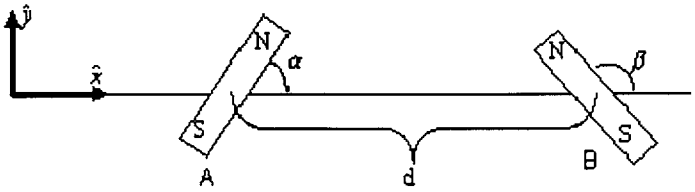

Figure 3.2 Two dipoles interacting in the far field

The interaction force between two arbitrary loops of current can be determined by the Law of Biot and Savart. However, they are difficult to solve except for cases of special symmetry such as circular coils. Therefore circular EMFF coils have been assumed for all analyses unless otherwise stated. The full three dimensional set of equations for forces and torques in the far field have been developed by Sedwick [17]. A simplified two dimensional set for two electromagnetic dipoles separated by a distance, *d*, oriented at arbitrary angles as seen in Figure 3.2 is given for the forces and torque on the left dipole (A) as

$$\begin{aligned} F_{x_A} &= \frac{3}{4\pi}\frac{\mu_0\mu_A\mu_B}{d^4}(2\cos\alpha\cos\beta-\sin\alpha\sin\beta) \\ F_{y_A} &= -\frac{3}{4\pi}\frac{\mu_0\mu_A\mu_B}{d^4}(\cos\alpha\sin\beta+\sin\alpha\cos\beta) \\ T_{z_A} &= -\frac{1}{4\pi}\frac{\mu_0\mu_A\mu_B}{d^3}(\cos\alpha\sin\beta+2\sin\alpha\cos\beta) \end{aligned} \tag{3.1}$$

The forces and torque on the right dipole (B) are

$$\begin{aligned} F_{x_A} &= \frac{3}{4\pi}\frac{\mu_0\mu_A\mu_B}{d^4}(2\cos\alpha\cos\beta-\sin\alpha\sin\beta) \\ F_{y_A} &= -\frac{3}{4\pi}\frac{\mu_0\mu_A\mu_B}{d^4}(\cos\alpha\sin\beta+\sin\alpha\cos\beta) \\ T_{z_A} &= -\frac{1}{4\pi}\frac{\mu_0\mu_A\mu_B}{d^3}(2\cos\alpha\sin\beta+\sin\alpha\cos\beta) \end{aligned} \tag{3.2}$$

The magnetic moment, μ, is defined as a function of the number of loops in a coil, n, the current in the conductor, i, and the coil radius, R_c, in the equation

$$\mu = ni\pi R_c^2 \tag{3.3}$$

If the dipole orientation angles are set to zero ($\alpha = \beta = 0$), the two dipoles align and the forces and torque simplify to

$$\begin{aligned} F_x &= \frac{3}{2\pi}\mu_o \frac{\mu_A \mu_B}{d^4} \\ F_y &= 0 \\ T_z &= 0 \end{aligned} \tag{3.4}$$

In order to generate large magnetic dipoles, Equation (3.3) indicates that a favorable electromagnetic coil design is one with many turns and high current. However, this drives up electromagnetic coil and solar array masses. Conventional coil conductors such as copper suffer from such high current application, since resistance causes significant heat generation and power losses. Therefore the design should utilize a coil that has the lowest resistance possible.

Superconducting material has zero resistance when cooled below a critical temperature resulting in no thermal heating and no power losses across the wire. With high temperature superconducting (HTS) wire, an electromagnet could be built to any size needed. Since there is no resistance, there is no heat production and a coil of any cross-sectional area can be made without fear of overheating the wire. Zero-resistance also means no power is required to maintain a high current through the wire causing the mass of the solar array to be determined by the power requirements of the spacecraft bus and payload mass, and not the coil. The only losses are in the power subsystem itself such as from regulators, switches, and batteries. Therefore the only limitation on the current is the critical current density of the superconducting wire.

There is a critical current density in the conductor above which the HTS will no longer conduct current at zero resistance. This clearly sets a limit on dipole strength.

Furthermore, adding more coil allows the dipole strength to be increased but at the cost of mass. As a result, the current limit and effect of HTS conductor mass density can be modeled.

$$\begin{aligned} i &= I_c A_c \\ M_c &= 2n\pi R_c A_c \rho_c \end{aligned} \tag{3.5}$$

where I_c is the critical current density (Amps/m^2), A_c is the cross-sectional area of the HTS wire, M_c is the mass of the coil, and ρ_c is the volumetric mass density of the HTS wire. Substituting into Equations (3.5) and (3.3) gives Equation (3.6) which can be further simplified if the coils on the two vehicles are assumed to be identical.

$$F_x = \frac{3}{8\pi}\mu_o \left(\frac{I_c}{\rho_c}\right)^2 M_{c_A} R_{c_A} M_{c_B} R_{c_B} \frac{1}{d^4} = \frac{3}{8\pi}\mu_o \left(\frac{I_c}{\rho_c}\right)^2 (M_c R_c)^2 \frac{1}{d^4} \tag{3.6}$$

There are three main design parameters in Equation (3.6). The I_c/ρ_c quantity is the HTS technology parameter and is fixed for various types of HTS wire. With better HTS technology, either through higher current density or lower mass density wires, this technology factor can be improved. The I_c/ρ_c has a value of 16,250 A·m/kg for current state of the art high strength HTS wire at 77 degrees Kelvin [18]. The M_cR_c quantity is the coil design parameter which can vary according to the design of a spacecraft. Finally, the array design parameter sets the separation distance, d. This is the design parameter most sensitive to changes since it has a fourth power relationship. These three design parameters are used throughout the chapter to understand how design affects the overall EMFF system.

3.2 Circular Trajectories

EMFF operating in circular trajectories has been envisioned for imaging applications such as interferometry of which TPF is an example mission. Circumnavigation of a non-EMFF target such as the Space Shuttle or other satellites using multiple EMFF spacecraft

could also be used for inspection or interrogation. The ability of EMFF to create these circular trajectories is developed in this section.

3.2.1 Agility Sizing

To understand the agility of EMFF spacecraft, a goal of the analysis is to achieve a five minute rotation period with a separation of 25 m. These possible maneuvers could represent an inspection around the space shuttle or modules of the space station.

Two spacecraft

The scenario shown in Figure 3.3 illustrates circumnavigation of a non-EMFF target which is located anywhere between the two spacecraft. Two spacecraft are in steady-state rotation about their common bari-center. The total mass of the system is constrained assuming it is set by a mission requirement. In addition, the total coil mass is constrained. The masses of the individual satellites and their coils are unequal but the coils have the same radii. Equal radii are assumed since the satellites may be docked during orbit transfer, and therefore have geometric constraints. They are undocked during inspection maneuvers and most of the massive subsystems remain with the parent satellite (vehicle A). The baseline scenario assumes the parameters shown in Table 3.1.

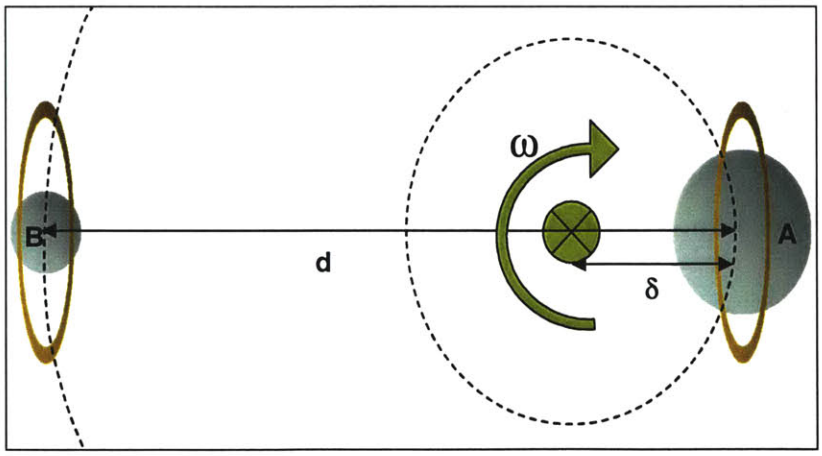

Figure 3.3 Two unequal mass satellites and coils with identical radius coils rotating around their common bari-center

Table 3.1 Parameters for baseline scenario

Parameter	Quantity	Units
Total mass (vehicles A+B)	200	kg
Total coil mass (vehicles A+B)	20	kg
I_c/ρ_c	16,250	Am/kg
Separation distance (d)	25	m
Coil radius	1	m
Desired rotation period	5	minutes
Reaction wheel speed	3000	rpm
Reaction wheel radius	0.25	m

The centripetal force must be supplied by the axial electro-magnetic force,

$$\begin{aligned} F_x &= M_{T_B}\omega^2\left(d-\delta\right) = M_{T_A}\omega^2\delta \\ \delta &= \frac{M_{T_B}}{M_T}d \end{aligned} \tag{3.7}$$

where the masses are given as

$$\begin{aligned} &M_o[\text{Total core mass}] = M_A[\text{Veh. A core mass}] + M_B[\text{Veh. B core mass}] \\ &M_c[\text{Total coil mass}] = M_{c_A}[\text{Veh. A coil mass}] + M_{c_B}[\text{Veh. B coil mass}] \\ &M_T[\text{Total vehicle mass}] = M_o + M_c \\ &M_{T_B}[\text{Total veh. B mass}] = M_B + M_{c_B} \end{aligned} \tag{3.8}$$

Solving Equation (3.7) for ω and substituting Equation (3.6), the resulting rotation rate is

$$\begin{aligned} \omega &= \left[k_o \frac{R_c^2}{d^5} \frac{M_T}{M_T - \left(M_B + M_{c_B}\right)} \frac{M_{c_B}\left(M_c - M_{c_B}\right)}{M_B + M_{c_B}} \right]^{1/2} \\ where\, k_o &= \frac{3}{8\pi}\mu_o\left(\frac{I_c}{\rho_c}\right)^2 \end{aligned} \tag{3.9}$$

To determine how vehicle B coil mass affects agility, the partial derivative of the rotation rate with respect to vehicle B coil mass is taken. Assuming the mass of vehicle B is less than half the total system mass, meaning vehicle B is the smaller vehicle, the optimum coil mass for vehicle B as a function of the core mass of vehicle B is

$$M_{c_{B_{opt}}} = \frac{M_B(M_T - M_B)}{M_o - 2M_B}\left\{-1+\left[1+\frac{M_c}{M_B}\frac{M_o - 2M_B}{M_T - M_B}\right]^{1/2}\right\} \tag{3.10}$$

Shown in Figure 3.4 is the system rotation rate versus vehicle B coil mass for different core masses for vehicle B (M_B) ranging from 100 kg to 0.4 kg. This assumes that the separation is constrained to 25 m. Notice that an optimum coil mass exists for each M_B that maximizes rotation rate. Also plotted by asterisks (*) is the curve relating rotation rate to the optimum vehicle B coil mass. This confirms the relationship for optimum coil mass. Notice that as the core mass of vehicle B becomes a smaller percentage of the system core mass, the corresponding optimum coil mass becomes less and the rotation rate increases.

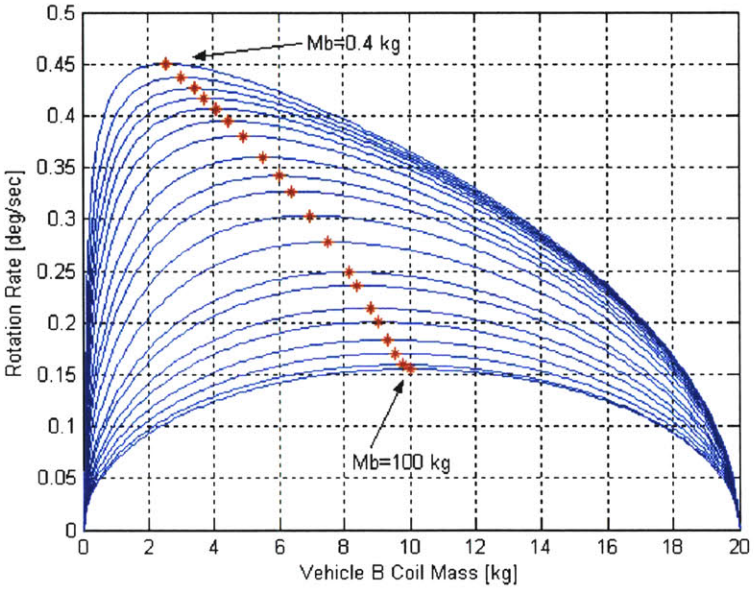

Figure 3.4 Rotation rate versus vehicle B coil mass

A plot of the revolution period as a function of the mass elements of vehicle B is seen in Figure 3.5. For example, if a thirty minute period is desired, the core must be 31 kg, and the coil must be 9 kg giving a total mass for vehicle B of 40 kg. Unfortunately, this system does not meet the goal of a five minute revolution time.

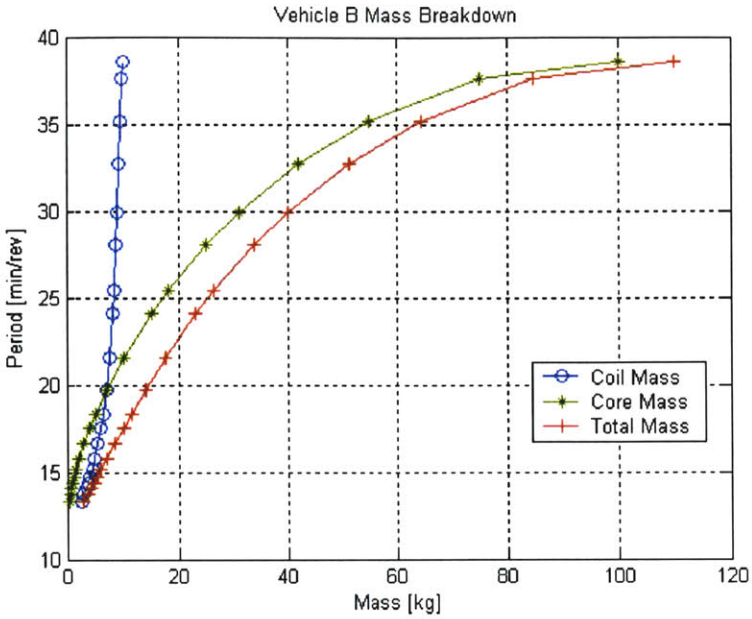

Figure 3.5 Mass breakdown for vehicle B

To understand the family of designs that can achieve the rotation rate and separation distance goal, the next step is to constrain the period to five minutes. Figure 3.6 plots separation distance versus vehicle B core mass where all designs have a five minute revolution period. Each curve uses the optimum vehicle B coil mass from Equation (3.10). The different color, thickness, and type curves are for different HTS technologies. The thin blue-dash-dot corresponds to the baseline technology, medium thickness red-dashed corresponds to three times the baseline, and thick green-solid corresponds to ten times the baseline. For a given line color/thickness/type, the four curves correspond to different coil radii ranging from 0.5 m to 2.0 m. There are several trends that are observed from Figure 3.6. First, less massive core vehicles can support larger separation distances. Second, increasing the coil radius given a vehicle core mass allows larger separation distances to be achieved while maintaining a five minute period. Third, the state-of-the-art HTS cannot achieve a five minute rotation period with a coil less than 2 meters in radius. Increasing the technology threefold rotates a 10 kg core in five minutes using a 1.5 meter radius coil. It also supports 23 kg using a 2 meter radius coil. Increasing the technology tenfold provides the following solutions: a 10 kg core using a 0.5 meter radius coil or a 100 kg core using 1.0 meter radius coil.

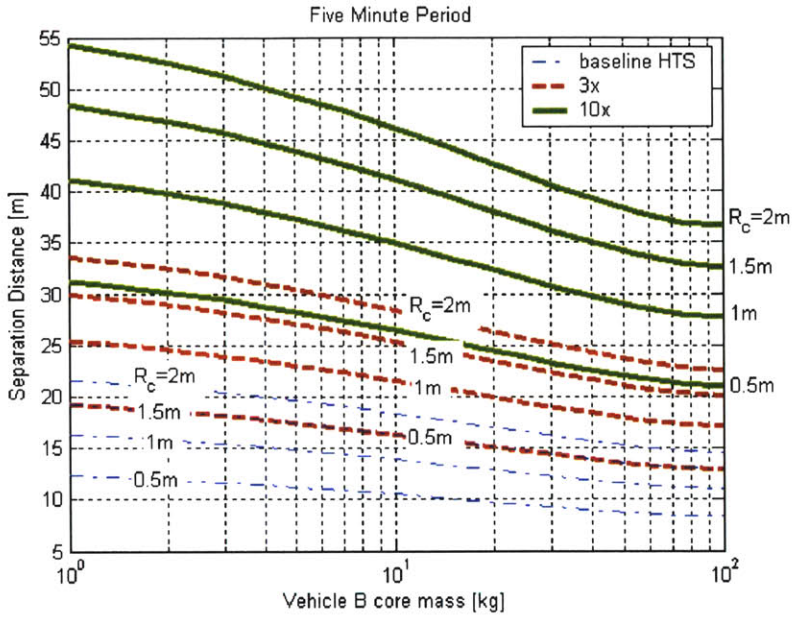

Figure 3.6 Separation distance versus vehicle B core mass for different HTS technology levels and coil radii, five minute revolution period

The last step is to constrain the separation to 25 m, while retaining the five minute period. These results, shown in Figure 3.7, plot the coil radius versus vehicle B core mass. The HTS technology levels correspond to a factor of one (dashed, blue), three (dotted, green), and ten (solid, red) times the current commercially available HTS technology level.

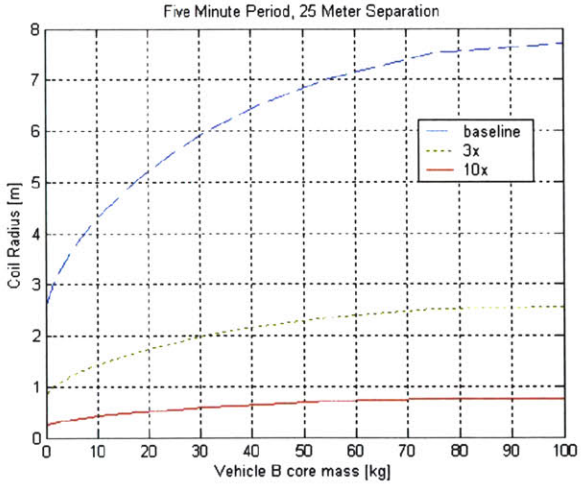

Figure 3.7 Coil radius versus vehicle B core mass, that provide a five minute period at 25 meters of separation, for three different HTS technology levels

Now that the coil has been sized the next component is the reaction wheel assembly. To angularly accelerate the two vehicle array, the dipoles are oriented orthogonally as seen in Figure 3.8. Notice in Equation (3.11) that the torque on the two vehicles is different by a factor of two while the transverse forces are the same.

$$\begin{aligned} &\text{if } \alpha = 0,\ \beta = \frac{\pi}{2} \text{ then } T_z = -\frac{1}{4\pi}\frac{\mu_o \mu_A \mu_B}{d^3} \text{ and } F_y = -\frac{3}{4\pi}\frac{\mu_o \mu_A \mu_B}{d^4} \\ &\text{if } \alpha = \frac{\pi}{2},\ \beta = 0 \text{ then } T_z = -\frac{2}{4\pi}\frac{\mu_o \mu_A \mu_B}{d^3} \text{ and } F_y = -\frac{3}{4\pi}\frac{\mu_o \mu_A \mu_B}{d^4} \end{aligned} \tag{3.11}$$

Due to conservation of angular momentum

$$H = \left(M_{T_A}\delta^2 + M_{T_B}\left(d-\delta\right)^2\right)\omega + I_{w_A}\omega_{w_A} + I_{w_B}\omega_{w_B} = 0 \tag{3.12}$$

Assume that the array is accelerated under constant transverse force. Then, the torques on the two vehicles are constant, although unequal. Equation (3.13) shows that if the reaction wheels on the two satellites are restricted to the same maximum speed, the relative inertias can be found.

$$\begin{aligned} &H_{w_A} = I_{w_A}\omega_{w_A} = T_{z_A} = 2T_{z_B} \\ &H_{w_B} = I_{w_B}\omega_{w_B} = T_{z_B} \\ &if\ \omega_{w_A} = \omega_{w_B} = \omega_w \\ &I_A = 2I_B \end{aligned} \tag{3.13}$$

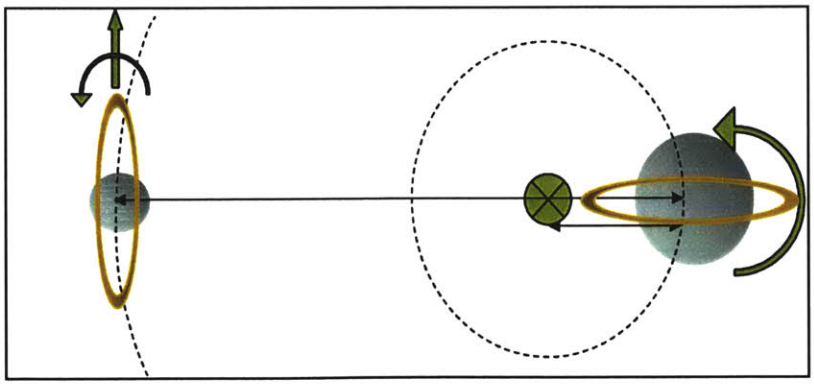

Figure 3.8 Dipole orientations during angular acceleration

Assuming the reaction wheel is a thin annular ring, the mass of the flywheel can be estimated once the radius is defined.

$$I_{w_B} = M_{w_B} r_{w_B}^2 \tag{3.14}$$

The mass of the reaction wheel on vehicle B can be found from

$$M_{w_B} = \left| \frac{\left(M_T - M_{T_B}\right)\delta^2 + M_{T_B}\left(d-\delta\right)^2}{3r_{w_B}^2} \frac{\omega}{\omega_w} \right| \tag{3.15}$$

The relationship between reaction wheel and core mass for a 0.25 m radius reaction wheel on vehicle B is shown in Figure 3.9. The separation is 25 m, the wheel speed is constrained to 3000 rpm, and the rotation period is five minutes. The constant diagonal lines indicate the percentage of total mass that is allocated to the reaction wheel. Notice that the more massive the core mass, the fraction of total mass that has to be dedicated to reaction wheel becomes smaller.

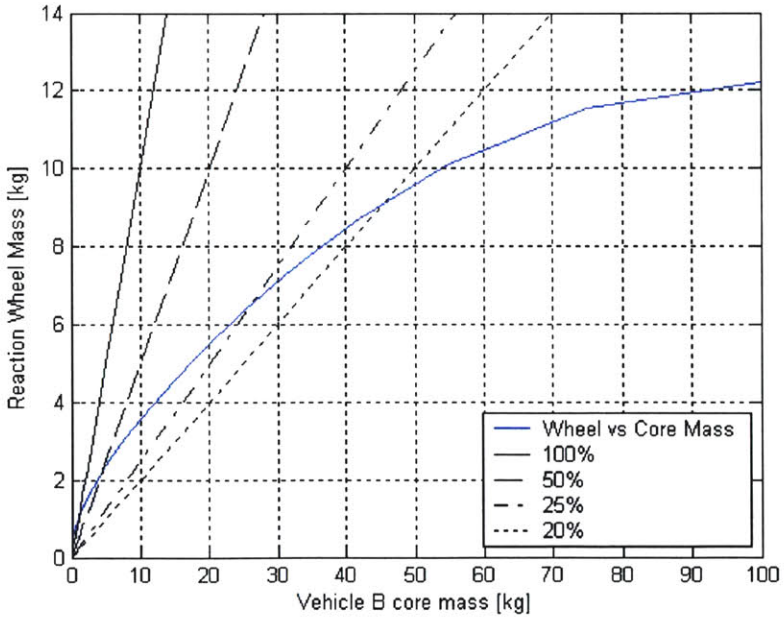

Figure 3.9 Reaction wheel versus core mass

Circular Trajectories with three spacecraft

One of the benefits of multiple spacecraft arrays is that the performance, in this case agility, dramatically improves by adding another spacecraft. Consider three spacecraft (S/C) in a line where the outer two are identical and smaller than the inner one. The inner spacecraft lies at the center of mass and the outer two orbit this inner spacecraft. The maximum separation is now the separation between the outer two spacecraft. This scenario is depicted in Figure 3.10.

The electromagnetic force on S/C_B, due to the two other spacecraft, provides the required centripetal acceleration

$$F_B = F_{B/A} + F_{B/B} = \frac{3}{8\pi}\mu_o\left(\frac{I_c}{\rho_c}\right)^2 \frac{m_{c_B}}{\left(\frac{d}{2}\right)^4}\left(m_{c_A} + \frac{1}{16}m_{c_B}\right) = \left(m_{o_B} + m_{c_B}\right)\omega^2\frac{d}{2} \qquad (3.16)$$

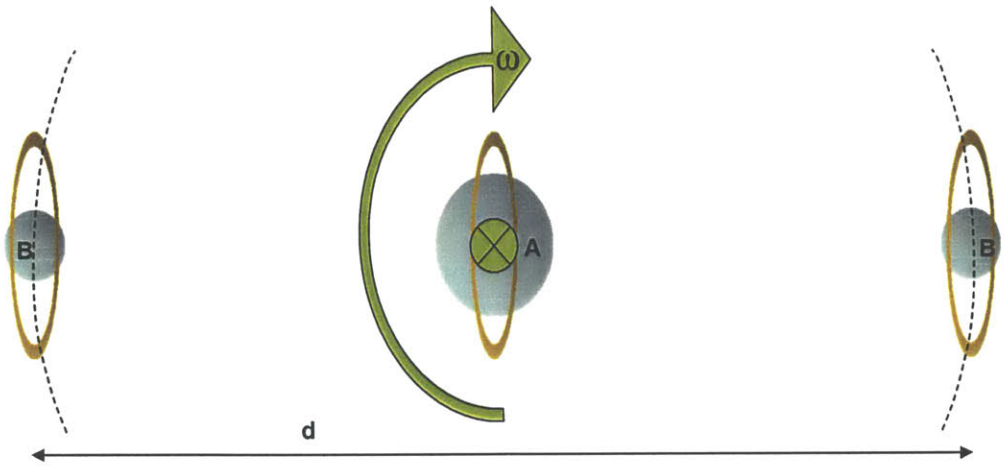

Figure 3.10 Two identical spacecraft orbiting about a third

Notice that the middle spacecraft is capable of providing 16 times greater force. This is since the middle spacecraft halves the separation distance between neighboring spacecraft, which is a fourth power effect. This bridging of the magnetic field is one of the benefits of multiple spacecraft arrays using EMFF. If a propellant-based spacecraft were introduced into the array, it would not have any effect on the force. In fact, the plumes it creates could hinder certain missions.

Expressing the core mass of S/C_A as a fraction of the total core mass, and likewise for the coil mass of S/C_A,

$$\begin{aligned} m_{c_A} &= \alpha m_c \\ m_{o_A} &= \beta m_o \end{aligned} \tag{3.17}$$

The square of the angular velocity is then given by

$$\omega^2 = \frac{3}{8\pi}\mu_o\left(\frac{I_c}{\rho_c}\right)^2\frac{R^2}{d^5}m_c^2\frac{1+30\alpha-31\alpha^2}{(1-\beta)m_o+(1-\alpha)m_c} \tag{3.18}$$

which can be maximized with respect to α,

$$\alpha_{opt} = \left(1+(1-\beta)\frac{m_o}{m_c}\right)\left[1-\left(1-\frac{1+\frac{30}{31}(1-\beta)\frac{m_o}{m_c}}{\left(1+(1-\beta)\frac{m_o}{m_c}\right)^2}\right)^{\frac{1}{2}}\right] \tag{3.19}$$

The rotation rate as a function of the coil mass of S/C_B, for different values of S/C_B core mass is shown in Figure 3.11. The nominal parameters from Table 3.1 are used with a separation between the outer two spacecraft of 25 m. The blue curves are repeated from Figure 3.4 while the green curves correspond to the three spacecraft scenario. Again, the red asterisks correspond to the optimum coil mass which maximizes array rotation rate. The horizontal magenta lines correspond to different durations for one revolution. Since the outer spacecraft are identical, the coil mass on each cannot exceed half of the total coil mass allocated to these spacecraft. Notice that the three spacecraft system can achieve dramatically higher rotation rates than the two spacecraft system. Furthermore, while the two spacecraft system cannot achieve one revolution in ten minutes, the three spacecraft system can orbit in less than three minutes.

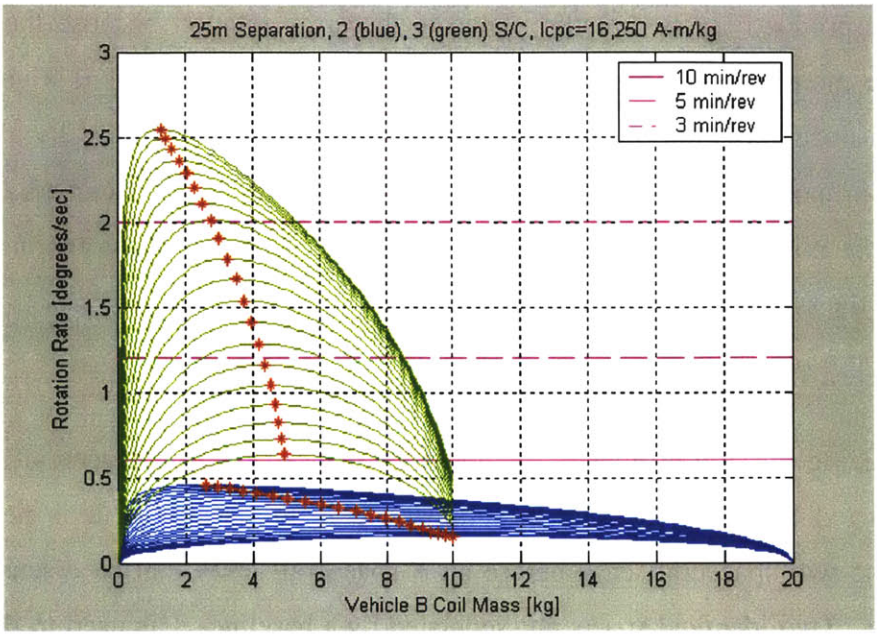

Figure 3.11 Rotation rate versus vehicle B coil mass for two and three spacecraft arrays

3.2.2 Mission Efficiency Sizing

Proposed missions such as TPF, which could utilize EMFF, consist of an array of multiple spacecraft. As arrays become populated with an increased number of spacecraft and array complexity increases, there exist cost and science productivity benefits in determining an optimal distribution of satellites. The main concern for EMFF is determining the optimal distribution of the electromagnetic mass, which consists of the electromagnetic coil mass and solar array mass.

The first concern in sizing an EMFF system is to determine the benefits of increasing the number of spacecraft in an array. For EMFF missions that require array rotation to conduct scientific observations, the mission efficiency can be defined as the science productivity divided by the cost.

$$J = \frac{w}{c_o m_{array}} \tag{3.20}$$

The science productivity is directly related to the array rotation because the faster the rotation, the more images produced in a given amount of time. This is a very general relationship since it assumes photon starvation does not occur. Additionally, the mass of the array is proportional to cost. To simplify J, a scaling term c_o is included. Therefore, increasing the mission efficiency is accomplished by increasing the rotation rate while minimizing the system mass.

Two Spacecraft

The maximizing mission efficiency methodology (MME) for two spacecraft arrays has been conducted by Kong [3], and is summarized in this section. It is necessary to introduce the two spacecraft case before an N-spacecraft array can be discussed in the next section. Two identical spacecraft separated by a baseline, d, is used to determine a nominal case for mission efficiency. The array rotation rate is found by equating the electromagnetic force to the centripetal force and solving for ω as seen in Equation (3.21) and Equation (3.22), where n is the number of coil turns, i is the current, and a is the coil radius.

$$F = \frac{3}{2}\mu_o \pi \frac{n^2 i^2 a^4}{d^4} = \frac{1}{2} m_{tot} \omega^2 d$$
$$\omega = \sqrt{\frac{3\mu_o \pi}{d^5}} \frac{nia^2}{\sqrt{m_{tot}}} \tag{3.21}$$

c_o is defined so that J becomes a function of the electromagnet properties. For two spacecraft, J_2 is found to be

$$m_{array} = 2m_{tot}$$
$$c_o = \sqrt{\frac{3\mu_o \pi}{d^5}} \tag{3.22}$$
$$J_2 = \frac{nia^2}{2m_{tot}^{3/2}}$$

where the total array mass, m_{array}, consists of two identical spacecraft.

This same procedure is repeated for three spacecraft, however with increased complexity. Assuming the array rotates around the center spacecraft, there are two layers of design, the inner and outer spacecraft layers designated by subscripts. Determining how to design these layers is discussed later. For simplicity, assume identical spacecraft masses. The force and magnetic interactions for three spacecraft is defined as

$$F = \frac{3}{2}\mu_o \pi a^4 \left(\frac{n_i i_i n_o i_o}{(\frac{d}{2})^4} + \frac{n_o^2 i_o^2}{d^4} \right) = \frac{1}{2} m_{tot} \omega^2 d \tag{3.23}$$

$$m_{array} = 2m_{tot_{outer}} + m_{tot_{inner}}$$

The mission efficiency for three identical spacecraft, J_3, is found to be

$$J_3 = \frac{\sqrt{17}}{3} \frac{nia^2}{m_{tot}^{3/2}} \tag{3.24}$$

The gain of adding a third spacecraft into the array can be found by taking the ratio of mission efficiencies.

$$\frac{J_3}{J_2} = 2.75 \tag{3.25}$$

The mission efficiency almost triples by adding a third spacecraft into the array. The added center spacecraft does not need to add scientific functionality in order to increase the amount of science collected. The outer spacecraft receives 16 times the electromagnetic force from the center spacecraft allowing the array to rotate much faster. Since the array rotates about the center spacecraft, the center vehicle does not need to translate. It can still provide the necessary magnetic forces to the outer spacecraft by steering its dipole. Since the center spacecraft does not need to translate relative to the outer spacecrafts, there is no mass penalty on it. This leads to a later trade on mass distribution of the array.

Additional Spacecraft

Uniformly incrementing the array with additional identical spacecraft continues the trend of increasing the mission efficiency. For N identical spacecraft in a uniformly separated array, the efficiency metric, J_N, is determined by

$$J_N = \frac{\sqrt{\sum_{i=1}^{N-1}\left(\frac{N-1}{i}\right)^4}}{N}\frac{nia^2}{m_{tot}^{3/2}} \tag{3.26}$$

Results of the optimized design parameters for two spacecraft and N spacecraft are summarized in Table 3.2, where the results in the first column are duplicated from Kong [3]. The relative efficiency between N spacecraft and N-1 spacecraft for systems with more than two spacecraft is

$$\Sigma_N = \frac{J_N}{J_{N-1}} = \frac{N-1}{N}\frac{\sqrt{\sum_{i=1}^{N-1}\left(\frac{N-1}{i}\right)^4}}{\sqrt{\sum_{i=1}^{N-2}\left(\frac{N-2}{i}\right)^4}} = \frac{(N-1)^3}{N(N-2)^2}\sqrt{1+\frac{1}{(N-1)^4\sum_{i=1}^{N-2}\frac{1}{i^4}}}\,,\ N>2 \tag{3.27}$$

Although additional spacecraft increase J, there are diminishing returns in relative efficiency as seen in Figure 3.12. For example, a five spacecraft array has a 40% improvement in mission efficiency over a four spacecraft array; however, a six spacecraft array only has a 25% improvement in mission efficiency over a five spacecraft array. This trend continues and for large N, Σ_N approaches 1.

3.2.3 Non-Identical Configuration

The MME design of an array applies very well with spacecraft of equal masses and for rotating systems. Instead of using ω as a critical design factor, a more generalized design parameter is the spacecraft agility, or acceleration of a spacecraft or array. Now, given design restrictions on total mass, the mass of an array can be distributed to optimize its

Table 3.2 Optimized design parameters for two spacecraft and *N* Spacecraft arrays.

Coil	Two Spacecraft Case [3]	*N* Spacecraft Case
turns	$n_{opt} = \dfrac{m_o}{2\pi^2 a \rho_c r^2}$	$n_{opt} = \dfrac{m_o}{2\pi^2 a \rho_c r^2}$
current	$i_{opt} = \pi r^2 \sqrt{\dfrac{P_W \rho_c}{p_c}}$	$i_{opt} = \pi r^2 \sqrt{\dfrac{P_W \rho_c}{p_c}}$
amp-turns	$ni\big\|_{opt} = \dfrac{m_o}{2\pi a}\sqrt{\dfrac{P_W}{\rho_c p_c}}$	$ni\big\|_{opt} = \dfrac{m_o}{2\pi a}\sqrt{\dfrac{P_W}{\rho_c p_c}}$
Spacecraft		
mass	$m_{opt} = 3m_o$	$m_{opt} = 3m_o$
power	$P_{opt} = m_o P_W$	$P_{opt} = m_o P_W$
rotation rate	$\omega_{opt} = \sqrt{\dfrac{3\mu_o \pi}{d^5}}\dfrac{a\sqrt{m_o}}{2\sqrt{3}\pi}\sqrt{\dfrac{P_W}{\rho_c p_c}}$	$\omega_{opt} = \sqrt{\sum_{i=1}^{N-1}\left(\dfrac{N-1}{i}\right)^4}\sqrt{\dfrac{3\mu_o \pi}{d^5}}\dfrac{a\sqrt{m_o}}{2\sqrt{3}\pi}\sqrt{\dfrac{P_W}{\rho_c p_c}}$
System		
mass	$m_{sys} = 6m_o$	$m_{sys} = 3Nm_o$
efficiency	$J_{opt} = \dfrac{a}{4\pi\sqrt{27 m_o}}\sqrt{\dfrac{P_W}{\rho_c p_c}}$	$J_{opt} = \dfrac{\sqrt{\sum_{i=1}^{N}\left(\dfrac{N-1}{i}\right)^4}}{N}\dfrac{a}{2\pi\sqrt{27 m_o}}\sqrt{\dfrac{P_W}{\rho_c p_c}}$

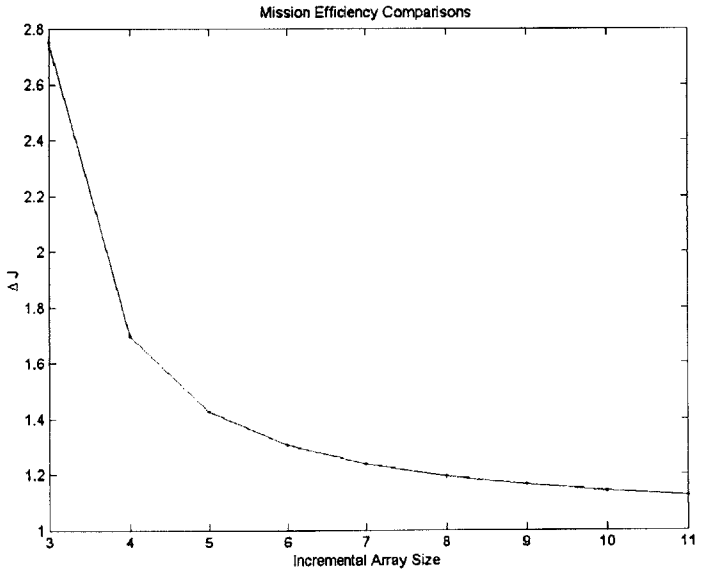

Figure 3.12 Mission efficiency comparison for additional spacecraft

acceleration. Similar to ω, the acceleration of a spacecraft determines its science productivity. In a three spacecraft array, the center spacecraft may consist of different number of amp-turns (η_i) from that of the two outer spacecraft (η_o) while it is assumed that the coil diameters are identical. The generated force is similar to the electromagnetic force from Equation (3.21) and can be solved for the acceleration of the outer spacecraft of the array, where η is substituted for amp-turns product (ni)

$$\ddot{x}_o = \frac{3}{2}\mu_o \pi \frac{a^4}{m_{o_{total}} s^4}\left(16\eta_i\eta_o + \eta_o^2\right) \qquad (3.28)$$
$$\eta = ni \ \text{[Amp-turns]}$$

The electromagnetic mass of a spacecraft consists of the coil mass and solar array mass. To simplify the approach, the coil and solar array masses have been rewritten in terms of the current density of the conductor

$$m_{em} = m_{coil} + m_{sa} = 2(\pi r)^2 na\rho_c + 2\left(\frac{i}{r}\right)^2 \frac{p_c an}{P_w} = 2\pi nia\frac{\rho_c}{c} + 2\pi nia\frac{p_c c}{P_w} \qquad (3.29)$$
$$m_{em} = 2\pi\eta a\left(\frac{\rho_c}{c} + \frac{p_c c}{P_w}\right)$$

The total mass of each spacecraft is now defined as

$$m_{total} = m_o + m_{em} = m_o + 2\pi\eta a\beta \qquad (3.30)$$

where

$$\beta = \frac{\rho_c}{c} + \frac{p_c c}{P_w} \qquad (3.31)$$

The three spacecraft array consists of two "layers." The inner layer consists of the center spacecraft bus and payload mass and electromagnetic mass, and the outer layer consists of the two identical bus and payload masses and electromagnetic mass of the outer spacecraft. The bus and payload mass of each spacecraft is assumed to be equal since

they have similar payloads for optics, avionics, etc. Therefore the electromagnetic mass is optimally distributed according to a mass fraction of the total electromagnetic mass

$$m_{em_i} = \gamma m_{em_{total}} \tag{3.32}$$

$$m_{em_o} = \left(\frac{1-\gamma}{2}\right) m_{em_{total}} \tag{3.33}$$

Equations (3.32) and (3.33) with Equation (3.30) to solve for the amp-turns for each layer.

$$\eta_o = \frac{1-\gamma}{2}\frac{m_{em_{total}}}{2\pi a\beta} \tag{3.34}$$

$$\eta_i = \gamma\frac{m_{em_{total}}}{2\pi a\beta} \tag{3.35}$$

Using this result, the acceleration of the array from Equation (3.30) is defined in terms of γ. Maximizing with respect to the mass fraction, the optimal mass fraction is found to be a function of bus and payload mass and total electromagnetic mass.

$$\frac{\partial \ddot{x}}{\partial \gamma} = 0 \Rightarrow \gamma_{opt} = \frac{62m_o + 31m_{em} - 2\sqrt{31m_o}\sqrt{31m_o + 16m_{em}}}{31m_{em}} \tag{3.36}$$

Table 3.3 Spacecraft mass breakdown [12]

Mass	Collector S/C		Combiner S/C	
Components	Mass	Power	Mass	Power
Dry	600 kg	268 W	568 kg	687 W
Propulsion	96 kg	300 W	96 kg	300 W
Propellant	35 kg	N/A	23 kg	N/A

For a spacecraft with a dry mass of 600 kg, similar to that of a TPF-class collector (based on the 1999 TPF book [12]) whose specifications are seen in Table 3.3, the electromagnetic (EM) mass distribution and its effect on rotation rate is shown in Figure 3.13. As a point of reference, if the propulsion and propellant mass for three collector

spacecraft were completely replaced with an EM system, the total EM mass would be approximately 400 kg. Shown are a family of curves that have 100, 200, 300, and 400 kg of electromagnetic mass along with horizontal lines depicting two hours per rotation and eight hours per rotation. The peaks of each curve correspond to the mass fraction that yields the maximum rotation rate. This optimal mass fraction of a three spacecraft array is shown in Figure 3.14.

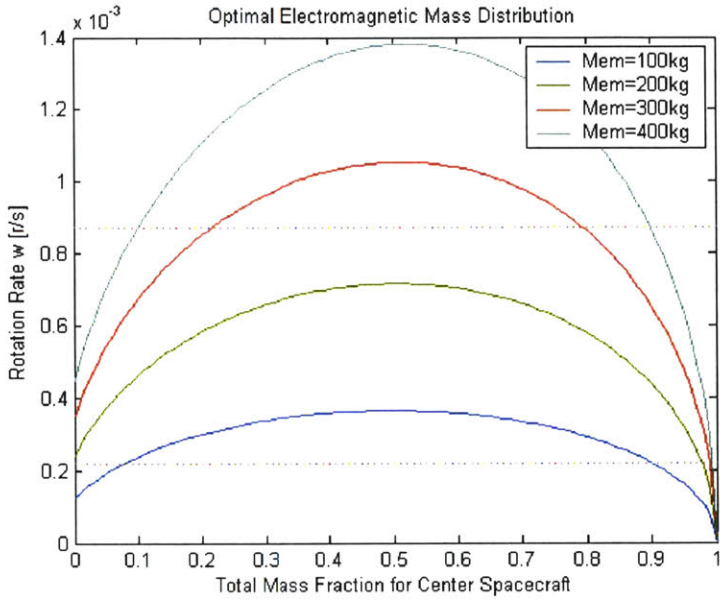

Figure 3.13 EM mass distribution effect on rotation rate for a three spacecraft TPF-class array

The optimum mass fraction is far from the identical three spacecraft configuration with close to half the total EM mass located on the center spacecraft. This is because the center spacecraft does not need to translate relative to the other spacecraft. However, some electromagnetic mass is needed on each spacecraft because the centripetal force is created by their mutual interaction. Therefore there is no mass penalty on the center spacecraft and the resulting electromagnetic mass is much greater than that of the outer spacecraft.

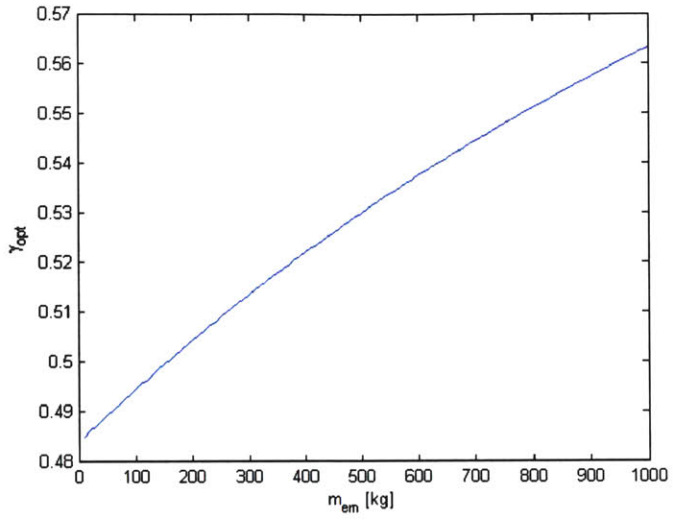

Figure 3.14 Optimal electromagnetic mass fraction of the center spacecraft for three spacecraft array with 600 kg dry mass.

3.3 Linear Trajectories

The next step is to explore the agility with which one vehicle can separate from a second vehicle to a distance of 25 m and return. As opposed to the previous sections, all motion is constrained to occur along the vector separating the two vehicles. This leads to a nonlinear dynamics analysis due to the range of separations that occur during the maneuver. This case is depicted in Figure 3.15, where vehicle A and B are shown at one instance of time with separation d_{min} and another instance of time with separation d_{max}. Agility is optimized across the same variables as explored in the previous section and the resulting performance is compared to the rotating system already studied.

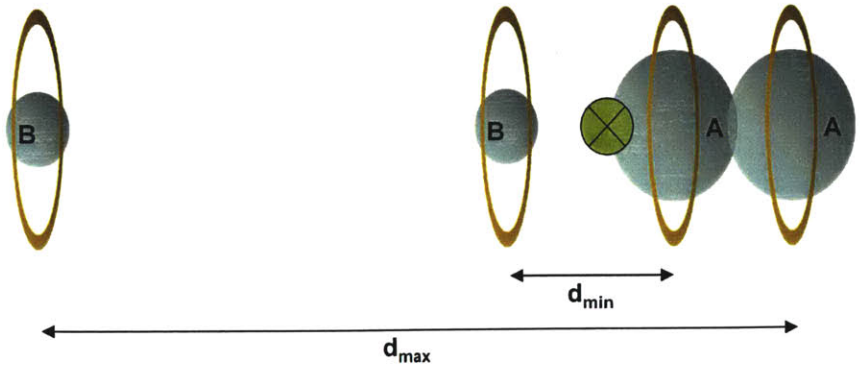

Figure 3.15 Two vehicles undergoing radial separation.

A dynamic simulation is created to assist in this analysis. Figure 3.16 shows the position and velocity time histories using the properties in Table 3.1 and assuming that the two vehicles are identical. Starting at an initial separation of 5m (d_{min} in Figure 3.15) with zero separation velocity, a repulsion force is created (Equation (3.6)) using the maximum capability of the coil for a specific duration. The axial force is then switched to be attractive at the maximum strength until the separation returns to the separation that was present when the polarity was switched, at which point the repulsion force is again created to brake the separation rate to return the vehicles to their initial separation at rest. Note that the rotational dynamics of the vehicles are unstable during repulsion but can be stabilized using reaction wheel control. The goal is to create a maximum separation of 25 m (d_{max} in Figure 3.15) and complete the roundtrip in five minutes. As expected, Figure 3.16 shows symmetry in both time as well as between the motions of the two vehicles. The latter will be lost as non-identical vehicle configurations are explored in maximizing agility. Note that the case shown in Figure 3.16 does not meet the maximum separation requirement.

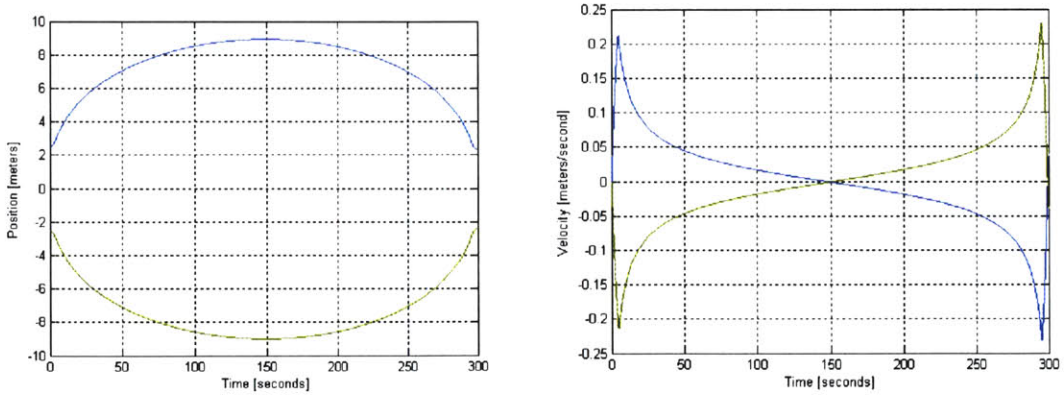

Figure 3.16 Temporal history for radial position and velocity.

In the previous section on agility sizing, it was found that there is an optimum coil allocation as a function of vehicle core mass. Therefore, the same is probably true in this case. Assuming that the metric to optimize is separation acceleration, if it can be maximized independent of separation distance, a single coil mass allocation can be found independent of the maneuver size. Separation acceleration is

$$\Delta\ddot{x} = \ddot{x}_B - \ddot{x}_A = \frac{c_o R_c^2}{\left(x_B - x_A\right)^4} M_T \frac{M_{c_B}\left(M_c - M_{c_B}\right)}{\left(M_T - \left(M_B + M_{c_B}\right)\right)\left(M_B + M_{c_B}\right)} \tag{3.37}$$

Taking the derivative with respect to M_{c_B} and setting it equal to zero gives the optimum coil mass for vehicle B, which maximizes separation acceleration.

$$M_{c_{B_{opt}}} = \frac{M_B M_T - \sqrt{M_B\left(M_B + M_c\right)\left(M_B - M_T\right)\left(M_B + M_c - M_T\right)} - M_B{}^2}{2M_B + M_c - M_T} \tag{3.38}$$

Notice that the optimum vehicle B coil mass is independent of separation distance making this coil mass provide the shortest maneuver time. It can also be shown that this optimum mass is the same as the optimum mass condition derived from the circular trajectories.

Shown in Figure 3.17 is the separation acceleration as a function of vehicle B coil mass for different values of vehicle B core mass ranging from half (100 kg) the total core mass of the system down to ten kg. The curves were calculated at a separation of ten meters. Clearly a maximum acceleration exists and the red points show the optimum vehicle B coil mass from Equation (3.38). The lighter the vehicle B core mass, the higher the separation acceleration and therefore the shorter the maneuver time. Likewise, as the core masses of vehicles A and B become identical, the distribution of coil mass becomes identical.

The simulation in Figure 3.18 assumes an optimized coil mass for a vehicle B core mass of ten kg. Notice that the separation of 25 m is almost achieved with commercial of the shelf (COTS) or baseline HTS technology, a vehicle B core mass of 10 kg, and is completed in five minutes. This is in stark contrast to Figure 3.5 where the minimum rotation period is 13 minutes as the core mass of vehicle B approaches zero. This is because in the linear trajectory, a major portion of the maneuver occurs with the separation between the two spacecraft much less than 25m where the EMFF force is substantially stronger. As a result, linear trajectories are much more agile. Further agility optimization includes exploring advanced HTS technology. Since no angular

momentum is being introduced into the relative motion between the vehicles, the reaction wheels only need to stabilize the unstable rotational dynamics during repulsion and damp the stable rotational dynamics during attraction. As a result, the reaction wheel can be substantially smaller.

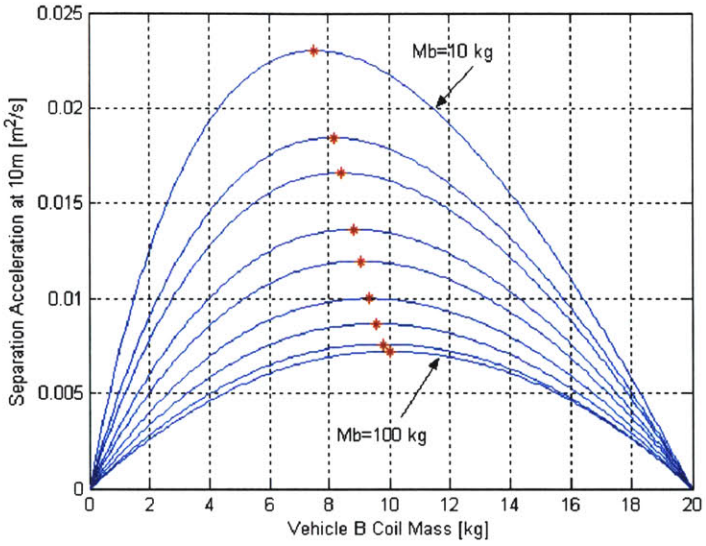

Figure 3.17 Relative acceleration versus vehicle B coil mass for different vehicle B core masses

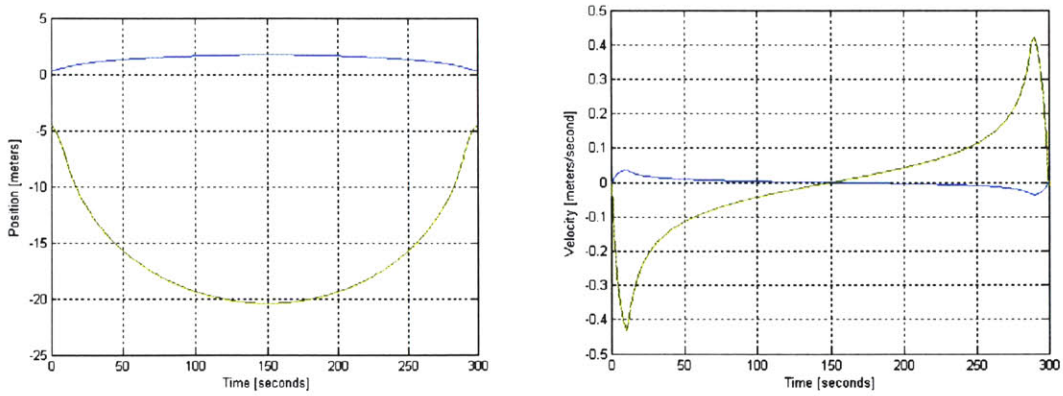

Figure 3.18 Core mass of vehicle B is 10 kg and coil mass is optimized at 7.55 kg. Maximum separation is 22.1 m.

The temporal histories of the magnetic moments in the two vehicles that were used to derive the trajectories in Figure 3.18 are shown in Figure 3.19. The moments are shown

as a fraction of the maximum moment that can be generated. Notice that the moment on vehicle A is maximized and held constant throughout the maneuver. The moment on vehicle B is initially positive to induce separation. There is a trade between the strength of this moment and the duration with which it is held. The polarity is then switched and the strength adjusted to cause the vehicles to return to their original separation after 300 seconds. Notice that the moment on vehicle B is very close to maximum. Unfortunately, this profile is very sensitive. The trajectories that result if the initial positive moment on vehicle B is held on for one-tenth of a second longer (11.1 versus 11.0 seconds) are shown in Figure 3.20. This is a change of less than 1% in duration. Notice that the trajectories are divergent and despite maximizing the moments on the two vehicles, they will forever drift apart. Because of this, it is necessary to perform these trajectories with margin on the moments. For example, a constraint could be placed that the nominal moment on vehicle B never exceeds 90% of maximum. Then, if there is an off-nominal event, there is margin that may allow the vehicles to be brought back together.

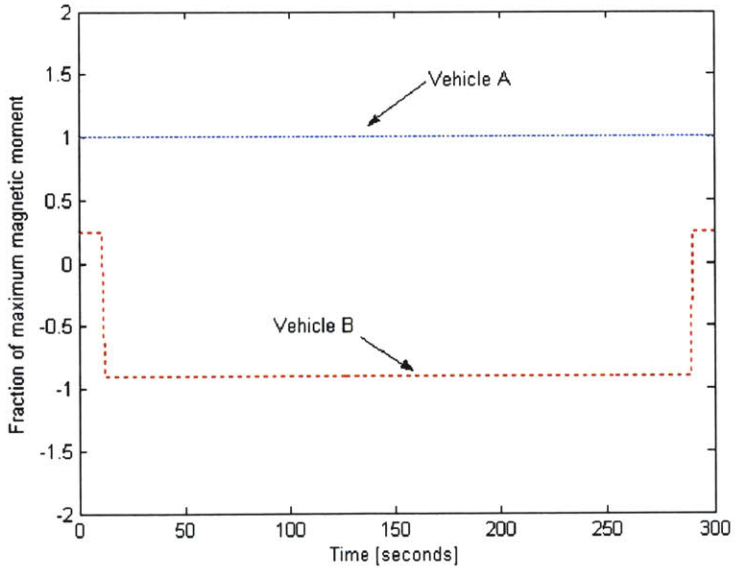

Figure 3.19 The fraction of the maximum magnetic moment in each vehicle as a function of time

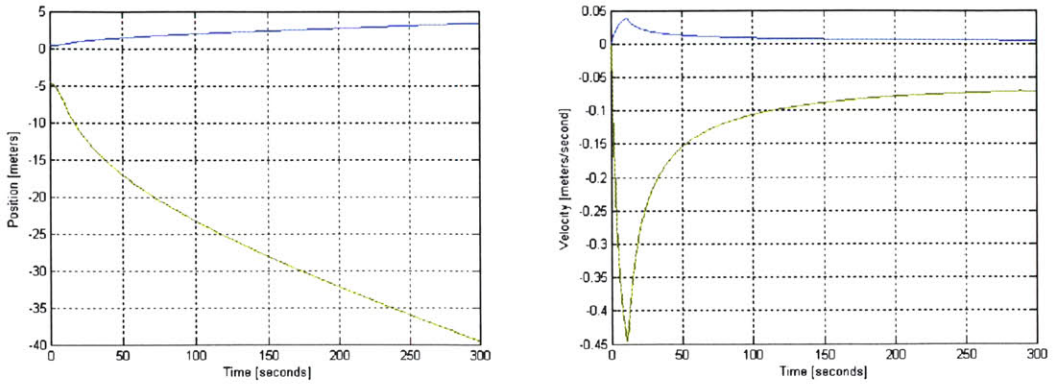

Figure 3.20 Divergent trajectories resulting from a tenth of a second increase in acceleration time (<1%) and maximizing the magnetic moments in both vehicles

Increasing the HTS technology threefold, by increasing the ratio of critical current density over mass density, allows larger vehicle B core masses to be maneuvered through the 25 m trajectory in five minutes. Figure 3.21 shows such a trajectory for a 50 kg core mass for vehicle B. This is a fivefold increase in the core mass of vehicle B and the maximum separation is close to 30 m.

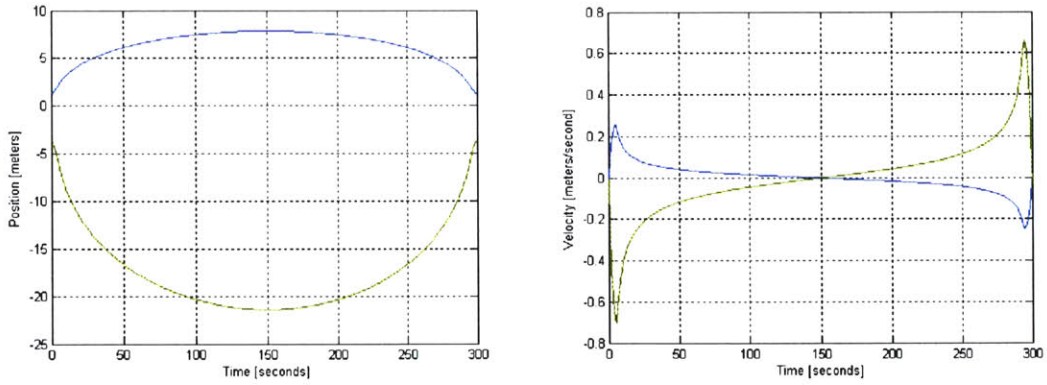

Figure 3.21 Trajectory for threefold increase in HTS technology and 50 kg core mass for vehicle B. Maximum separation is 29.3 m.

3.3.1 Escape Velocity

Clearly, if the separation velocity between the vehicles is greater than a certain value, the electromagnets will not be able to halt their separation, even at maximum coil strength, the vehicles will drift apart. Furthermore, this critical velocity is smaller the greater the

separation between the vehicles. To calculate the relationship between critical velocity and separation, the relationship in Equation (3.39) is used which expresses the change in energy of the system in terms of the integrated work performed. The critical initial velocity (v_i) is that which causes the final separation velocity (v_f) to be zero at infinite separation (x_f).

$$\int_{v_i}^{v_f} v dv = \int_{x_i}^{x_f} a dx \quad \Rightarrow \quad \int_{v_i}^{0} v dv = \int_{x_i}^{\infty} a dx = \int_{x_i}^{\infty} \frac{-k}{x^4} dx \tag{3.39}$$

Integrating and solving gives the relationship in Equation (3.40). The critical velocity is proportional to $x^{-\frac{3}{2}}$ which decreases with separation.

$$v_i^2 = \frac{2}{3}\frac{k}{x_i^3} \quad \Rightarrow \quad v_i = \sqrt{\frac{2}{3}\frac{k}{x_i^3}} \tag{3.40}$$

The value for k can be determined from Equations (3.37) and (3.38). Obviously, the vehicles should be operated below this critical velocity to provide margin against the possibility that the HTS trips and field strength is temporarily lost. This relationship can be used to determine the time that is available to recover field strength.

Assume that the separation velocity and distance are v_1 and x_1, respectively. At this point, the HTS trips into non-superconducting mode and the field strengths are lost. With the vehicles separating at this velocity, the time available to bring the coils back on line, before they are lost, is given by

$$t_c = \frac{1}{v_1}\left(\sqrt[3]{\frac{2}{3}\frac{k}{v_1^2}} - x_1\right) \tag{3.41}$$

3.4 Conclusions and Future System Trades Work

There are three recurring trends from the system trades. The first is that asymmetric EMFF systems tend to have an increased performance. Creating a mother-daughter relationship, where the mother spacecraft is relatively large and the daughter spacecraft is

small, results in systems with high agility. This was also seen when approximately 50% of the electromagnetic mass was located on the center spacecraft to maximize the mission efficiency.

The second is adding EMFF intermediaries into an array which bridge the magnetic field can also lead to increased performance, both for agility and mission efficiency. One can envision this idea on an extremely large scale, where two spacecraft with large science payloads are kilometers apart, but many small EMFF 'bridging' spacecraft lie between them providing force for the entire array.

The third is that higher levels of HTS technology can significantly help the performance of a system. As technology improves, the forces generated increase with technology squared.

So far relatively simple arrays and maneuvers have been addressed. The next steps are to investigate more unique EMFF configurations, such as non-collinear arrays or three dimensional arrays, and hybrid trajectories that incorporate linear and circular movements. The next steps in EMFF system sizing are to determine optimal configurations of these different arrays and also larger arrays. Optimal mass distributions for larger arrays can be simplified by adding additional pairs of spacecraft for a collinear array. Future missions which incorporate up to dozens of EMFF satellite can benefit from this additional analysis.

Chapter 4

EMFF SUBSYSTEM DESIGNS

So far the model of an EMFF spacecraft has been relatively simplistic consisting of the coils and a spacecraft bus. The spacecraft bus has conveniently represented all the subsystems necessary to operate satellite, both in terms of carrying out its intended mission and utilizing EMFF. This chapter describes those subsystems critical to an EMFF satellite and the effects these subsystems have on the overall performance. Once these subsystems have been designed, they can be used to model a more complete EMFF system in Chapter 5.

4.1 Superconducting Wire Performance Variation

The subsystem that enables EMFF is the superconducting wire. The critical current density of the HTS wire is affected by the operating temperature and the magnetic field across the wire. The variation in the critical current density is seen in Figure 4.1 which shows I_c normalized by the I_c at 77 K with no magnetic field as a function of the magnetic field for various operating temperatures. The effect of a magnetic field parallel to the HTS (or tape) surface is shown in Figure 4.1a and the effect of the magnetic field perpendicular to the HTS surface is shown in Figure 4.1b. The cross-sectional view of an HTS wire in Figure 4.2 clarifies the direction of magnetic field perpendicular to the HTS surface and the direction of magnetic field parallel to the HTS surface.

Equation (3.3) indicates that the three ways to generate a large magnetic moment are by using a high amount of coil turns, a high amount of current in the conductor, or a large coil radius. The maximum current in the conductor is limited by technology and the coil size is usually limited by mass and launch constraints. However, one can still generate large magnetic moments by using a large number of coil turns. A stack of HTS wires is illustrated in Figure 4.2 for n turns along with a zoomed view of the HTS wires insulated

by yellow Kapton tape. Each wire has a thickness of 300 μm. Encased inside the wire is the black superconducting material. To model the magnetic field, each wire is treated as a line current and the distance between line currents is approximately 400 μm [9]. The magnetic field that each wire sees from other wires in the same stack is approximated as parallel to the HTS surface.

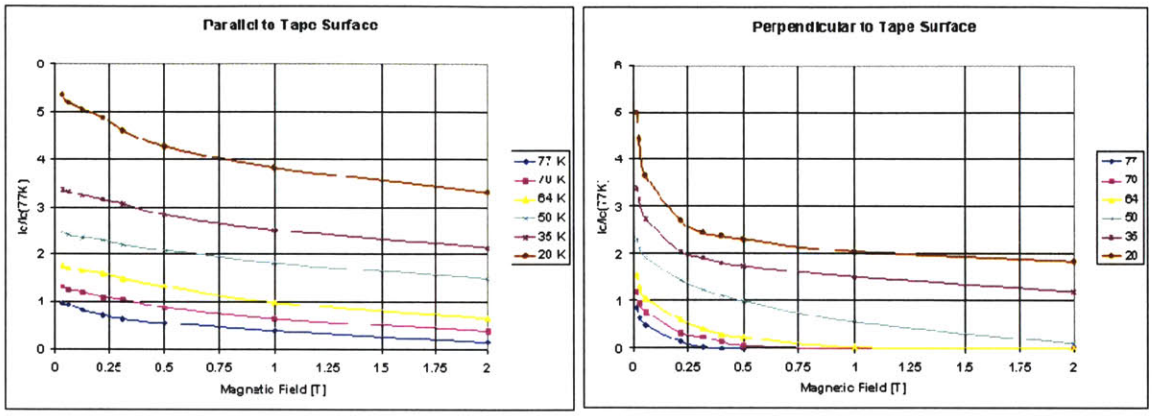

(a) (b)

Figure 4.1 Variation of HTS critical current density with temperature and magnetic field parallel (a) and perpendicular (b) to the HTS wire [18]

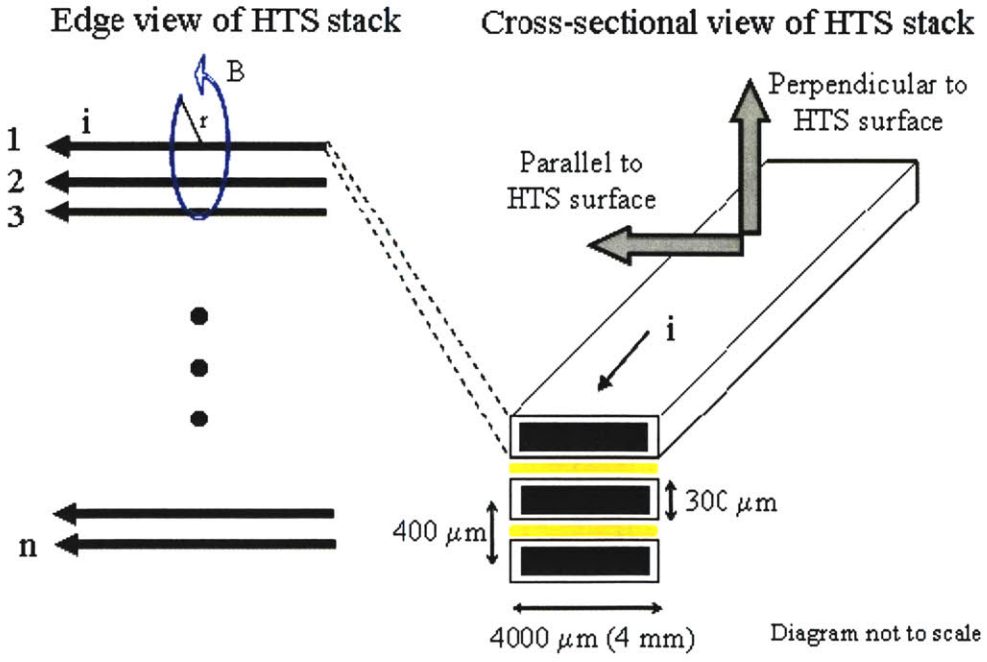

Figure 4.2 Geometry of HTS coil turns

The magnetic field at a distance r that is generated by a line current is

$$B = \frac{\mu_o i}{2\pi r} \tag{4.1}$$

Each wire in the stack generates this magnetic field. In addition, each wire sees a magnetic field generated by all the other wires that is parallel to the wire surface. From Figure 4.2, the field that wire 1 experiences from the j^{th} wire in the stack is

$$B = \frac{\mu_o i_j}{2\pi(j-1)r} \tag{4.2}$$

The wires that see the maximum sum of the magnetic fields are the wires on the ends of the stack. These are the wires at the inner and outer radii of the annulus. For a stack with n turns, this maximum magnetic field is

$$B_N = \frac{\mu_o}{2\pi}\sum_{j=2}^{n}\frac{i_j}{(j-1)r} \tag{4.3}$$

The magnetic field that wire 1 sees from the j^{th} wire is shown in the left graph in Figure 4.3 where the j^{th} wire has a current of 95 Amps. The magnetic field drops off as one over distance, which is expected from a line current. The right graph in Figure 4.3 shows the magnetic field seen by wire 1 as a result of summation of the magnetic field from n-1 wires, each with 95 A. Given the number of turns in a stack, the magnetic field in the direction parallel to the HTS surface can be determined. Using the magnetic field and the operating temperature, the variation in I_c can be found using Figure 4.1a.

The effects of the magnetic field have only considered one stack of HTS wires. The coils in the MIT-SSL EMFF testbed consist of three stacks of HTS wires, where each stack is 33 turns. The cross-sectional view of this configuration is shown in Figure 4.4. Each stack is separated by approximately 5 mm. Again, approximating each wire as a line current, the line currents are separated by 12.5 mm.

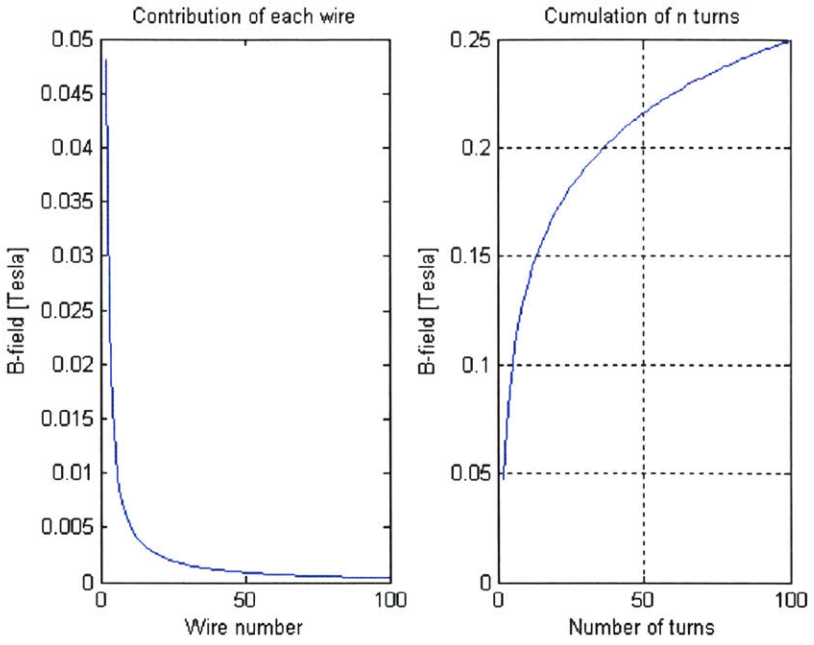

Figure 4.3 Magnetic field from line currents

The magnetic field that the HTS wires sees from a neighboring stack is perpendicular to the HTS surface. Earlier it was determined that the ends of the stack experience the maximum amount of magnetic field parallel to the HTS surface due to other wires within the same stack. The next step is to determine the effect of the magnetic field perpendicular to the HTS surface due to wires in neighboring stack.

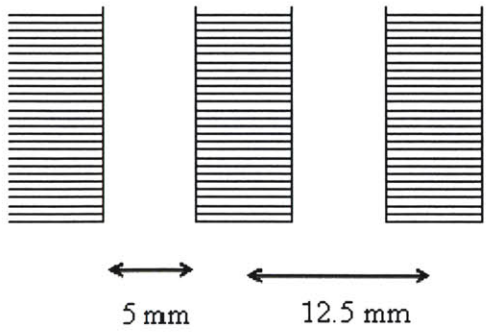

Figure 4.4 HTS wire stacks for the MIT-SSL EMFF testbed

To simply the problem and obtain an order of magnitude result, the effect of the top wire from the center stack on the top wire from the rightmost stack is investigated. These line

current have a distance of 12.5 mm away, so the perpendicular magnetic field due to a current of 95 Amps is

$$B_{\perp} = \frac{\mu_o i}{2\pi r} = \frac{4\pi \cdot 10^{-7} \cdot 95}{2\pi \cdot 0.0125} = 0.00152 \text{ Tesla} \tag{4.4}$$

The contribution of the perpendicular magnetic field is much less than the parallel magnetic field. This is also true for the magnetic field from other wires in the center stack seen by the top wire in the rightmost stack, since separation distance increases. The effects of wires in the neighboring stack can be seen as higher order effects and are effectively negligible.

The expected I_c variation can be compared to the actual I_c variation measured by HTS wires in the MIT-SSL EMFF testbed. This analysis uses the single stack assumption. The maximum observed current through the coils is approximately 95 A. According to American Superconductor, the theoretical maximum allowable current is 115 A for a 100 m wire length [18]. Therefore, the fraction of current observed experimentally compared to the maximum allowable current is

$$\frac{I(\text{B-field})}{I(\text{no B-field})} = \frac{95}{115} = 0.83 \rightarrow 17\% \, I_c \text{ reduction} \tag{4.5}$$

Using Equation (4.3), the magnetic field at the ends of the stack from 33 turns is

$$B_{33} = 0.1958 \text{ Tesla} \tag{4.6}$$

The I_c variation for small magnetic fields parallel to the HTS wire is close to linear and is shown in Figure 4.5a. This figure is a zoomed in version of Figure 4.1a with a linear fit to the I_c data for the 77 K curve. Using the linear fit, the I_c variation for the magnetic field from 33 turns is approximately 0.75. This results in a 25% predicted reduction in I_c. Compared to the experimentally observed 17% reduction in current, the predicted reduction of 25% is conservative.

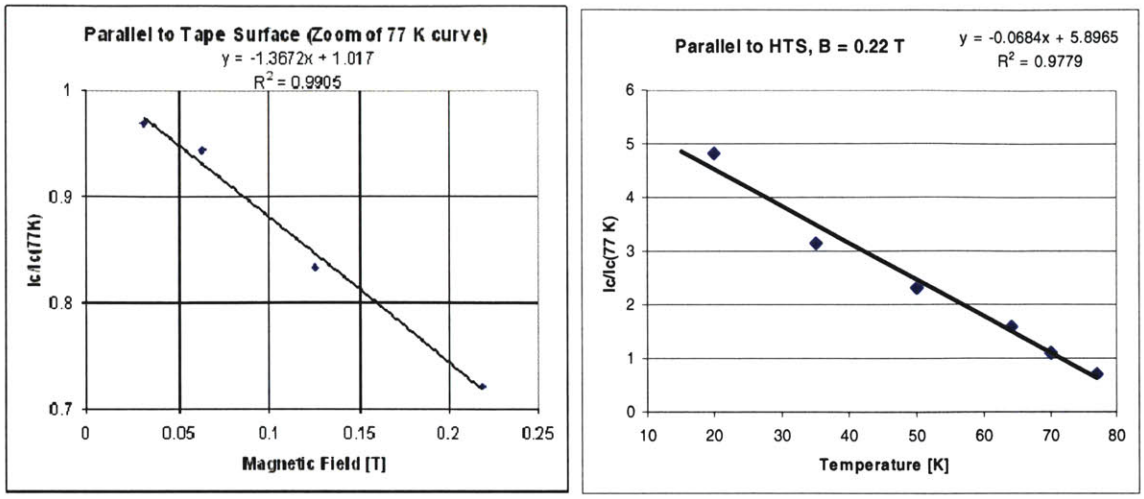

(a) (b)

Figure 4.5 Linear fit of a) I_c variation versus parallel magnetic field for 77 K, b) I_c variation versus temperature for B = 0.22 T

The testbed actually sees more current than predicted. This 8% difference between the predicted reduction and the experimentally observed reduction can be attributed to three possible sources of error. The first is the accuracy of the current measured by the current sensors. It is possible that the measured current differs from the actual current due to sensor noise, calibration, etc. The second possible source of error is the temperature of the HTS wire during the experiment. If the liquid nitrogen provided a temperature lower than 77 K, the HTS wires would see an increase in I_c. The third source of error involves the tightness of the HTS stack. This is the most likely source of error. The distance between wires in a stack, r, has a large impact on the magnitude of the magnetic field. The separation distance used for the analysis is 400 μm, which was estimated before the HTS wires were sealed in the liquid nitrogen containment system. If the HTS stack were packaged looser, that is, with a greater separation between the wires, the magnitude of the magnetic field would be reduced. It is possible that repetitive liquid nitrogen cycling loosened the HTS stack enough to slightly increase the separation distance. A separation of 615 μm between wires (r = 615 μm) results in a magnetic field of 0.0125 Tesla. In this case, the expected reduction in I_c is 17%, which is correlates with the experimental results.

4.1.1 Effects on spacecraft acceleration

Previous EMFF system designs in Chapter 3 have assumed operation at 77 K with no magnetic field across the wires. Reducing temperature can increase I_c while the magnetic field from multiple turns can decrease I_c. The I_c due to the temperature and magnetic field normalized by the I_c at 77 K with no magnetic field is defined as

$$\eta_I = \frac{I_c}{I_c(77\text{K, no field})} \tag{4.7}$$

For a given magnetic field parallel to the HTS wire, the relationship between η_I and temperature is approximately linear between 20 K and 77 K. This is seen in Figure 4.5b for a magnetic field of 0.22 T and is described by the equation

$$\eta_I = a_1 T + b_1 \text{ , } 20\text{ K} \le T \le 77\text{ K} \tag{4.8}$$

A magnetic field of 0.22 T is generated by approximately 55 turns, as seen in Figure 4.3. Decreasing the temperature (a_1 is negative) allows for an increase in η_I, but at the cost of increasing the power required for the thermal cryogenic system and the power to drive the additional current through the warm electronics associated with the coils. The cryogenic system enables the coil to operate at superconducting temperatures and requires power to maintain cold temperatures given a steady state thermal load. The relationship between input power and temperature is approximated by a second order polynomial between 50 K and 77 K

$$P_T = a_2 T^2 + b_2 T + c_2 \text{ , } 50\text{ K} \le T \le 77\text{ K} \tag{4.9}$$

A second order polynomial is selected for simplicity. Higher order polynomials could also have been used. The data used for this curve fit is shown in Figure 4.6 for a thermal load of 2.5 W and is based on cryogenic coolers developed at NASA Goddard [19].

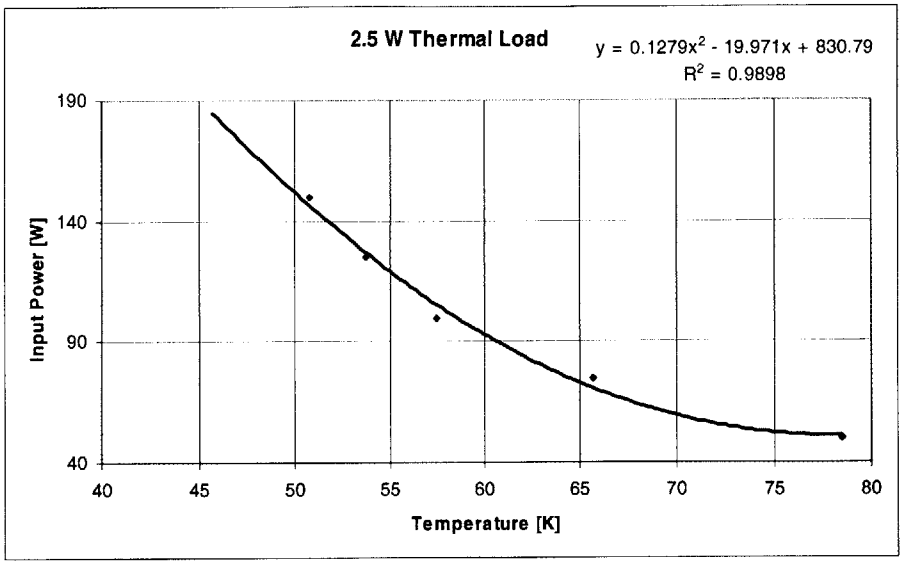

Figure 4.6 Cryogenic system power versus temperature for a 2.5 W thermal load

Clearly the operating temperature has a large impact on η_l and the required power. As the critical current density increases, the force generated increases, as seen in Equation (3.6). This increase in I_c, caused by a decrease in the temperature, consequently increases the required thermal control power and as a result, drive up the mass of the solar array. To determine how the temperature impacts the overall system agility, Equation (3.6) is rewritten to include η_l

$$F = \frac{3}{2}(10^{-7})\left(\eta_l \frac{I_C}{\rho}\right)^2 (M_C R_C)^2 \frac{1}{d^4} \tag{4.10}$$

The spacecraft mass consists of the nominal mass, coil mass, the thermal cryogenic system mass and the solar array mass. Combining the Equation (4.10) and the total spacecraft mass yields

$$a = \frac{F}{M_t} = \frac{\frac{3}{2}(10^{-7})\left(\eta_l \frac{I_C}{\rho}\right)^2 (M_C R_C)^2 \frac{1}{d^4}}{M_o + M_c + M_t + M_p} \tag{4.11}$$

$$M_p = \frac{P_t + (\eta \cdot I_C A_C)^2 R}{P_s}$$

Substituting Equations (4.8) and (4.9) into Equation (4.11)

$$a = \frac{\frac{3}{2}(10^{-7})\left((a_1 T + b_1)\frac{I_C}{\rho}\right)^2 (M_C R_C)^2 \frac{1}{d^4}}{M_o + M_c + M_l + \frac{a_2 T^2 + b_2 T + c_2 + (a_1 T + b_1)^2 A_C {I_C}^2 R}{P_s}} \tag{4.12}$$

Taking the partial derivative of acceleration with respect to temperature yields an optimum temperature which is simply a function of a_1 and b_1.

$$\frac{da}{dT} = 0 \rightarrow T_{opt} = -\frac{b_1}{a_1} = 86.2 \text{ K} \tag{4.13}$$

The parameters used to determine the optimum temperature are seen in Table 4.1. Figure 4.7 shows the acceleration with I_c variation from magnetic field and temperature (Equation (4.12)) normalized by the acceleration with no I_c variation (HTS wires at 77 K with no magnetic field) as a function of temperature. It is important to remember the temperature range used in the linear approximation of η_l (20 K $\leq T \leq$ 77 K) and in the second order polynomial approximation of P_T (50 K $\leq T \leq$ 77 K). These temperature ranges are marked in Figure 4.7. Outside of these ranges are regions where the approximations may not hold. The optimum temperature, T_{opt}, at 86 K is a minimum point. This optimum temperature occurs outside of the temperature ranges used in the polynomial approximations. In addition, temperatures greater than T_{opt} are unrealistic for operation since the HTS wire does not superconduct. Temperatures less than T_{opt}, indicate conditions where an increase in acceleration is achieved. This is an increase in acceleration compared to the acceleration achieved with HTS wires at 77 K with no magnetic field, which was the condition used in previous analyses. Between 70 K and 77 K is a region where there is a loss in acceleration compared to the acceleration used in previous analyses due to the reduction in I_c from the magnetic field. In this region, there is not a sufficient enough increase in I_c from the temperature reduction to offset the decrease in I_c due to the magnetic field. For example, from Figure 4.7 at 77 K

$$\frac{a\ (\text{B field})}{a\ (\text{no B field})}(T = 77\ \text{K}) = 0.4 \tag{4.14}$$

To verify this result, the reduction in I_c at 77 K from Equation (4.8) is

$$\begin{aligned} \eta_I(T = 77\ \text{K}) &= (-0.0684 \cdot 77 + 5.9) = 0.633 \\ \eta_I{}^2 &= 0.4 \end{aligned} \tag{4.15}$$

This result yields the same answer for the normalized acceleration at 77 K seen in Equation (4.14). Note this example is simplified since η_I is unity at 77 K with no magnetic field.

Temperatures less than 71 K yield designs where the gain is greater than one. In conclusion, there are significant benefits which can be achieved by operating at colder temperatures.

Table 4.1 Parameters used to determine effect of I_c variation

Parameter	Symbol	Value
Coil Radius	R_c	1 m
Coil Mass	M_c	10 kg
Power system resistance	R	0.010 Ohm
Spacecraft separation	d	25 m
Spacecraft nominal mass	M_o	100 kg
Thermal cryocooler mass	M_t	2.3 kg
Solar Array specific power	P_s	25 W/kg
Curve fit constant	a_1	-0.0684
Curve fit constant	b_1	5.9
Curve fit constant	a_2	0.128
Curve fit constant	b_2	-20.
Curve fit constant	c_2	831.

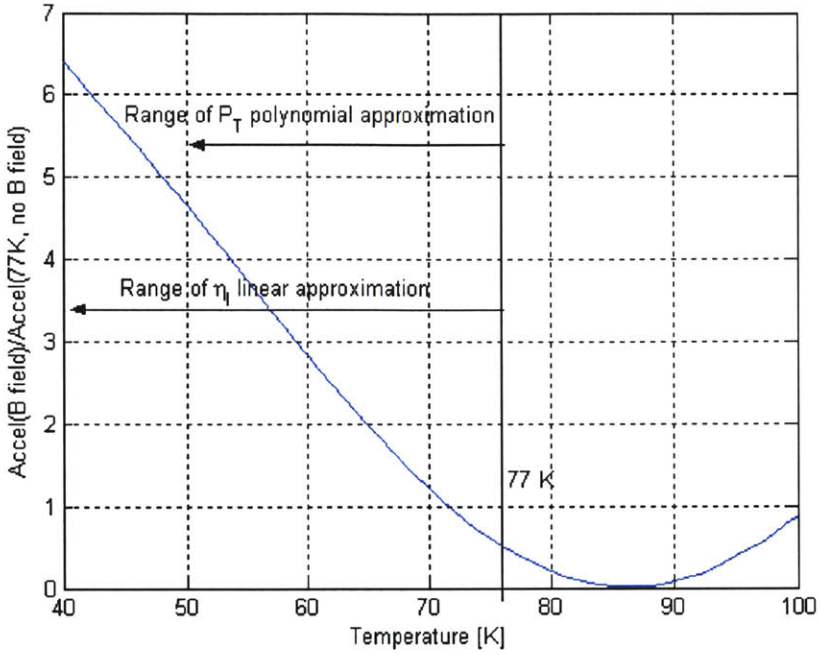

Figure 4.7 Acceleration with I_c variation from magnetic field and temperature normalized by acceleration with no I_c variation (77 K, no magnetic field)

4.1.2 Effects on total loop current

The magnetic moment is directly proportional to the total loop current. A primary concern of the reduction in I_c is its effect on the total loop current, I_t, which is the current in the conductor times the number of coil turns

$$I_t = ni = n\left(A_c I_c\right) \tag{4.16}$$

As the number of turns increases, the total current increases proportionally. But the magnetic field on the ends of the HTS stack also increases with each additional turn resulting in a decrease in I_c. Thus, it is important to understand if adding additional turns will increase or decrease the total loop current. Equation (4.16) is expanded to include the effects of magnetic field parallel to the wire and becomes

$$I_t = NA_c I_c(77\text{K, no field}) \cdot \eta_I = NA_c I_c(77\text{K, no field}) \cdot \left(0.92e^{-0.87 B_N} + 0.08\right) \tag{4.17}$$

where the exponential expression for η_I comes from curve fitting the η_I versus magnetic field for the 77 K data from Figure 4.1a. A constant term is also added to the fit to ensure η_I is unity for zero magnetic field. The total loop current as a function of turns is shown in the top graph of Figure 4.8 in solid red. The total loop current for the imaginary case where the magnetic field does not affect I_c is also plotted by the dotted blue line. The difference between these lines is the loss in total loop current caused by the reduction in I_c from the magnetic field. This is shown by the bottom graph of Figure 4.8 which plots the ratio of total loop current in the case where the magnetic field affects I_c over the total loop current in the imaginary case where the magnetic field does not affect I_c. For example, the total loop current at 200 turns is 80% of the total loop current possible in the case with no magnetic effects.

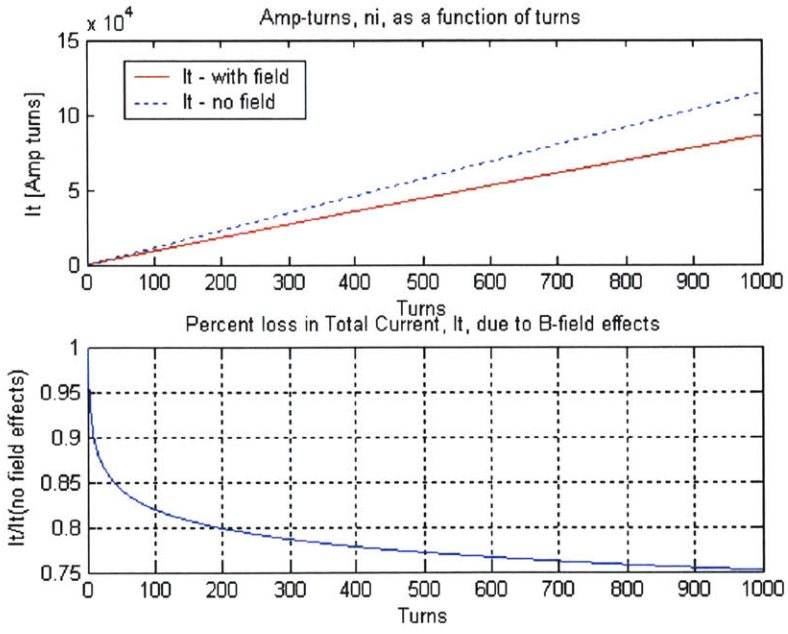

Figure 4.8 Total loop current versus loop turns at 77 K

For a HTS stack less than 1000 turns, the total loop current continues to increase in a linear fashion with the number of turns. According to the MIT-SSL EMFF testbed, the HTS wires are packaged with a distance of 400 μm per turn. For a spacecraft with 250 turns in a one or two meter radius coil, this results in a stack that is 10 cm tall. In comparison, this is about eight times taller than an HTS stack in the MIT-SSL EMFF

testbed. As an upper bound, Figure 4.8 uses 1000 turns to determine how coil turns affect total loop current. At 1000 turns, the total magnetic field on the ends of the HTS stack is approximately 0.36 T, which does not reduce I_c enough to cause in a decrease in total loop current for additional turns. For cases with 10,000 turns the total loop current continues to increase in a linear fashion with the number of turns and does not see a reduction of the total loop current for additional turns. This means that for high n the curve of total current versus turns (top graph in Figure 4.8) is linear.

4.2 Thermal Subsystem

One of the challenges of implementing superconducting wire for EMFF is maintaining the cold temperatures necessary for superconductivity. Superconducting wire has a critical temperature, below which superconducting occurs, and above which the wire 'trips' or ceases to conduct high currents. When the wire trips, the magnetic field generated drops significantly and since EMFF satellites depend on the forces and torques created by the external field, the formation could fail if the wire trips. By characterizing the thermal problem and its solution for EMFF, one can then begin to design the necessary subsystems to maintain the critical temperature.

Current commercially available high temperature superconducting wire (HTS) has a critical temperature of 115 K [18]. For a ground testbed system, the solution is to immerse the HTS wire in a liquid Nitrogen bath, which has a temperature of 77 K. A liquid Nitrogen reservoir is also necessary in order to replace the liquid Nitrogen that boils off. Two possible designs for this on a ground testbed are a gravity-fed reservoir system and a pressurized tank system as shown in Figure 4.9. For space applications, a reservoir of coolant is not desirable since a consumable is then required for EMFF. However, cooling in space can be achieved by cryocoolers, which are used in some current space telescope systems such as Spitzer and future space telescope systems such as TPF.

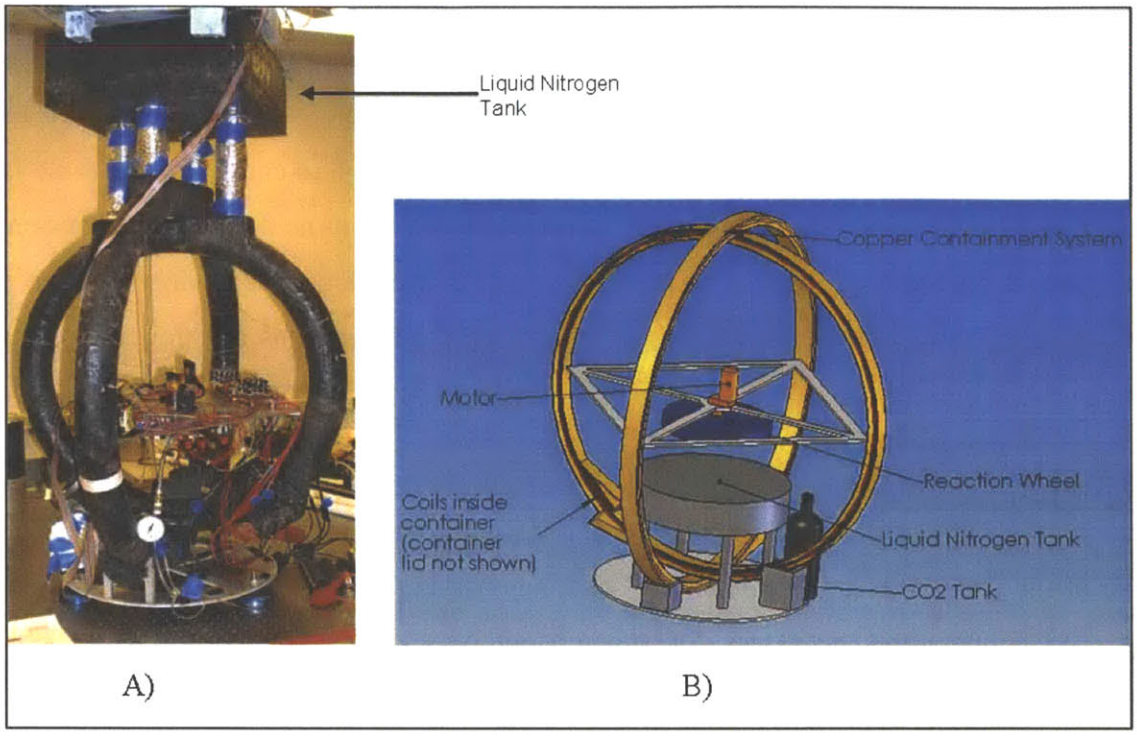

Figure 4.9 a) Gravity fed system b) Pressurized tank system

This thermal analysis of the EMFF system will determine if EMFF can operate with only passive thermal control components. Passive thermal control components are those not requiring power. If passive thermal control components are not sufficient, then the amount of heat that needs to be extracted to achieve superconducting temperatures needs to be determined. Then the next step is to design a system that minimizes the power needed by the active thermal subsystem. To determine the worst case steady state conditions a single coil whose plane is perpendicular to the solar radiation is analyzed. Figure 4.10 illustrates the analysis of one of the three orthogonal EMFF coils with major radius R_c and cross section A. The HTS wire radius, r_c, is the distance taken up by a bundle of HTS wires, and not necessarily a single wire.

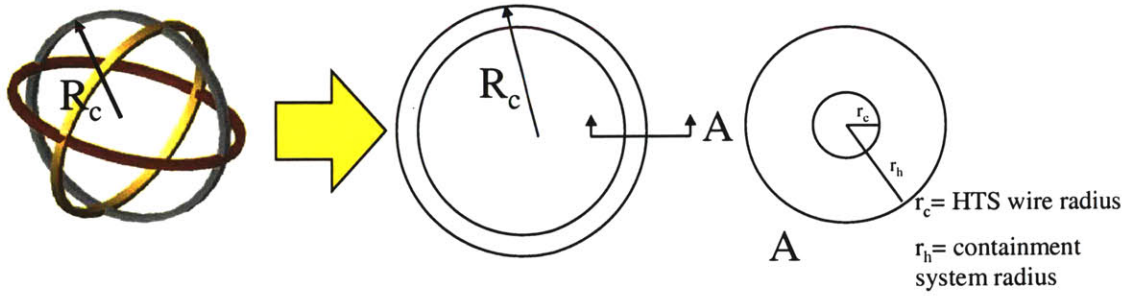

Figure 4.10 Coil geometry

Two possible designs for thermal protection around the HTS wire between r_c and r_h include insulation or a vacuum-gap. For the vacuum-gap case, it is assumed that the standoffs holding the HTS wire bundle in place conduct a minimal amount of heat. Additionally, the coil radius (R_c) and HTS wire bundle radius (r_c) are set by the mission specifications and are not driven by the thermal needs.

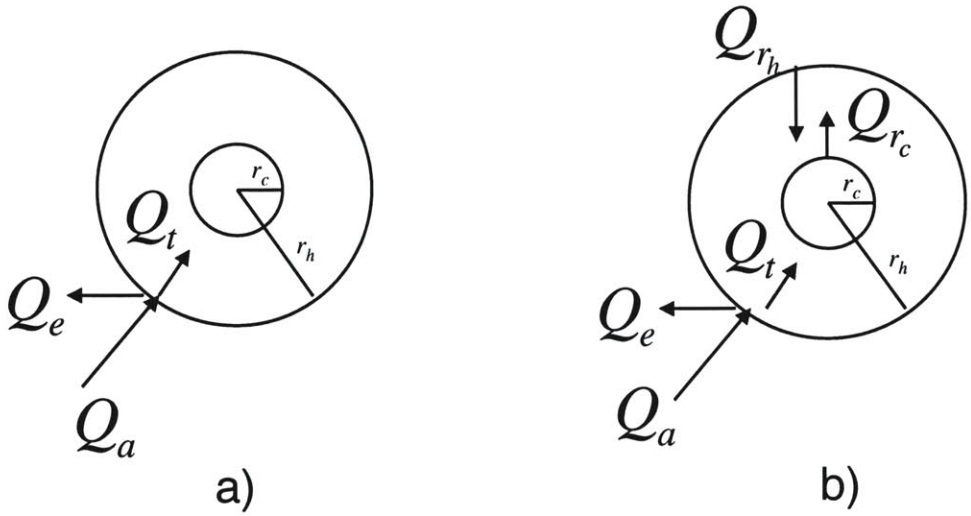

Figure 4.11 Thermal free body diagrams for a) Insulation case b) Vacuum-gap case

4.2.1 Earth Trailing Orbit

From the geometry given, Figure 4.11a shows the heat flow for the insulation case in a thermal free body diagram. It is assumed that the solar radiation uniformly heats the outside of the coil. The equilibrium equation is

$$Q_a = Q_e + Q_t \tag{4.18}$$

where Q_a is the heat rate in Watts into the coil from solar radiation, Q_e is the heat rate emitted by the coil into deep space, and Q_t is the heat rate into the HTS wire by conduction. These equations for heat flow can also be shown as

$$\begin{aligned} G_s \alpha A_a &= \sigma \varepsilon A_e (T_h^4 - 4^4) + \frac{4\pi R_c K (T_h - T_c)}{\ln(r_h / r_c)} \\ A_a &= 4\pi R_c r_h \\ A_e &= 4\pi^2 R_c r_h \end{aligned} \tag{4.19}$$

where G_s is the solar constant, α is the absorptivity of the containment material, A_a is the area of absorption, A_e is the area of emission, σ is the Stefan-Boltzmann's constant, 5.670 51 ·10-8 $W \cdot m^{-2} K^{-4}$, ε is the emissivity of the containment material, and K is the thermal conductivity of the insulation. The temperature needed at r_c, T_c, is the temperature of HTS operation, which is assumed to be 77 K, the same operating temperature as the MIT-SSL EMFF testbed. The unknown temperature T_h, can be solved from the fourth order polynomial, with constants c_1 and c_0, derived from Equation (4.19), which has the form

$$T_h^4 + c_1 T_h + c_0 = 0 \tag{4.20}$$

The design parameters are the containment material properties α and ε, the thermal conductivity of the insulation, and the size of the containment system, r_h. Since the objective is to minimize heat flow into the HTS wires, the insulation with the lowest thermal conductivity should be chosen. The original ground testbed in the MIT SSL has a foam insulation system, which has a thermal conductivity of 0.22 $W \cdot m^{-1} \cdot K^{-1}$, however for a flight system, one could use Aerogel which has a much lower thermal conductivity of 0.004 $W \cdot m^{-1} \cdot K^{-1}$. Once T_h has been determined from Equation (4.20), the heat flow into the HTS wires can be determined

A similar equilibrium analysis is carried out for the vacuum-gap case, whose thermal free body diagram is shown in Figure 4.11b. The heat flow equilibrium equations are

$$\begin{aligned} Q_a &= Q_e + Q_t \\ Q_t &= Q_{r_h} - Q_{r_c} \end{aligned} \tag{4.21}$$

containment material which has an absorptivity to emissivity ratio of 0.1. The coil has a major radius of 1 m and a HTS wire bundle radius of 1 cm. The vacuum-gap design is most favorable if the coil was tightly packed with the containment system, since a smaller containment system results in less solar radiation absorption. If a larger packaging system is needed, possibly for structural or electrical reasons, Aerogel is a more favorable option for radii greater than 2.08 cm. A cylindrical structure allows for greater amounts of insulation for increasing the containment system radius, which is why the heat flow into the coil decreases for increasing radii after a certain point for the Aerogel case. For this worst case scenario, where the plane of a single coil is perpendicular to the solar radiation, the heat rejection is in the tens of Watts. This amount of heat can be rejected by using one or two known commercial off the shelf (COTS) cryocoolers by SunPower, which are listed in Table 4.2. To interface with the cryocooler, the coil is in close contact with the cryocooler cold finger, which provides the low temperature throughout the coil by conduction. The amount of power needed by the cryocooler is about twenty to twenty-five times the cooling power. The mass of the cryosystem is relatively light, under 5 kg, which does not add significantly to the mass budget of a satellite. Custom made cryocoolers are also capable of higher heat rejection if necessary, but most likely for a greater cost than a commercially available system.

Table 4.2 Cryocooler specifications

Company	SunPower	SunPower
Model	M77	M87
Cooling Power (W)	4	7.5
Temperature (K)	77	77
Input Power (W)	100	150
Mass (kg)	3	2.7

4.2.2 Low Earth Orbit

The previous results were applicable for a satellite in an Earth trailing orbit. The thermal analysis for a satellite in LEO includes additional heat sources from the Earth albedo and infrared emissions. This affects the absorbed heat flow, Q_a, as follows

containment material which has an absorptivity to emissivity ratio of 0.1. The coil has a major radius of 1 m and a HTS wire bundle radius of 1 cm. The vacuum-gap design is most favorable if the coil was tightly packed with the containment system, since a smaller containment system results in less solar radiation absorption. If a larger packaging system is needed, possibly for structural or electrical reasons, Aerogel is a more favorable option for radii greater than 2.08 cm. A cylindrical structure allows for greater amounts of insulation for increasing the containment system radius, which is why the heat flow into the coil decreases for increasing radii after a certain point for the Aerogel case. For this worst case scenario, where the plane of a single coil is perpendicular to the solar radiation, the heat rejection is in the tens of Watts. This amount of heat can be rejected by using one or two known commercial off the shelf (COTS) cryocoolers by SunPower, which are listed in Table 4.2. To interface with the cryocooler, the coil is in close contact with the cryocooler cold finger, which provides the low temperature throughout the coil by conduction. The amount of power needed by the cryocooler is about twenty to twenty-five times the cooling power. The mass of the cryosystem is relatively light, under 5 kg, which does not add significantly to the mass budget of a satellite. Custom made cryocoolers are also capable of higher heat rejection if necessary, but most likely for a greater cost than a commercially available system.

Table 4.2 Cryocooler specifications

Company	SunPower	SunPower
Model	M77	M87
Cooling Power (W)	4	7.5
Temperature (K)	77	77
Input Power (W)	100	150
Mass (kg)	3	2.7

4.2.2 Low Earth Orbit

The previous results were applicable for a satellite in an Earth trailing orbit. The thermal analysis for a satellite in LEO includes additional heat sources from the Earth albedo and infrared emissions. This affects the absorbed heat flow, Q_a, as follows

$$
\begin{aligned}
Q_a &= G_s aA + Q_{IR} + Q_{albedo} \\
Q_{IR} &= q_{IR} A\varepsilon \sin^2 \rho \\
Q_{albedo} &= G_s aA\alpha K_a \sin^2 \rho
\end{aligned}
\tag{4.24}
$$

where q_{IR}, is the IR energy flux from the Earth. The angular radius of the Earth is ρ and K_a accounts for the reflection of solar energy off a spherical Earth. Both are a function of altitude, H, and the radius of the Earth, R_E, and are defined as

$$
\begin{aligned}
\sin \rho &= \frac{R_E}{H + R_E} \\
K_a &= 0.664 + 0.521\rho - 0.203\rho^2
\end{aligned}
\tag{4.25}
$$

The analysis uses a representative LEO altitude of 400 km. This is also the altitude of the International Space Station. Consequently these results are applicable for EMFF operations at the space station, which were discussed in Chapter 3. Again, the worst case scenario is analyzed using an upper bound for the Earth albedo and IR energy flux of 0.35 and 258 $W \cdot m^{-2}$ respectively. The mean area of the absorption for the coil considered is

$$
A_{mean} = 4\pi r_h R_c = 0.2356 \text{ m}^2 \tag{4.26}
$$

The heat rejection in LEO is shown by the upper two curves in Figure 4.13 and the lower two curves shows the Earth trailing orbit case. The heat rejection is greater in LEO, but still not an insurmountable problem. The LEO heat rejection would most likely require more than one cryocooler, however the important thing to consider is that these results show the worst case scenario for the coil that is perpendicular to the sun and receiving all its solar radiation. The coil that is edge on to the sun receives a significantly less amount of solar radiation, and thus a significantly less amount of heat rejection is needed. Also, in LEO, eclipse reduces heat load. In addition, if the spacecraft has a hot and cold side, created by a sunshield, the amount of heat rejection is approximately proportional to the amount of the coil that is exposed to the sun on the hot side.

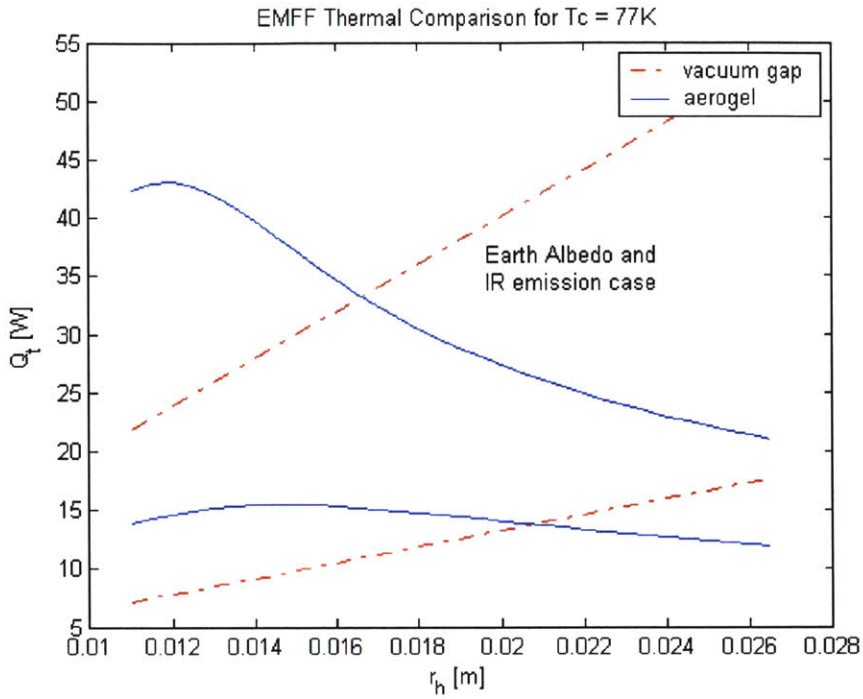

Figure 4.13 Heat flow comparison for LEO and Earth trailing orbit

4.2.3 Material Selection

Further design optimization can be accomplished by selecting the right materials for the containment system size. Table 4.3 shows two materials that have a different absorptivity and emissivity. This results in different heat rejection curves as shown in Figure 4.14. The first plot shows the heat rejection for the Earth trailing orbit case, where the material with the lower absorptivity to emissivity ratio results in the lower heat rejection design. For the LEO case, a combination of picking the lowest absorptivity to emissivity ratio and lowest emissivity yields the lowest heating. This is because the Earth's IR heat flow depends on the emissivity of the material.

Table 4.3 Containment material properties

Material	Absorptivity, α	Emissivity, ε	α/ε
OSR	0.079	0.79	0.1
Silvered Teflon	0.08	0.66	0.12

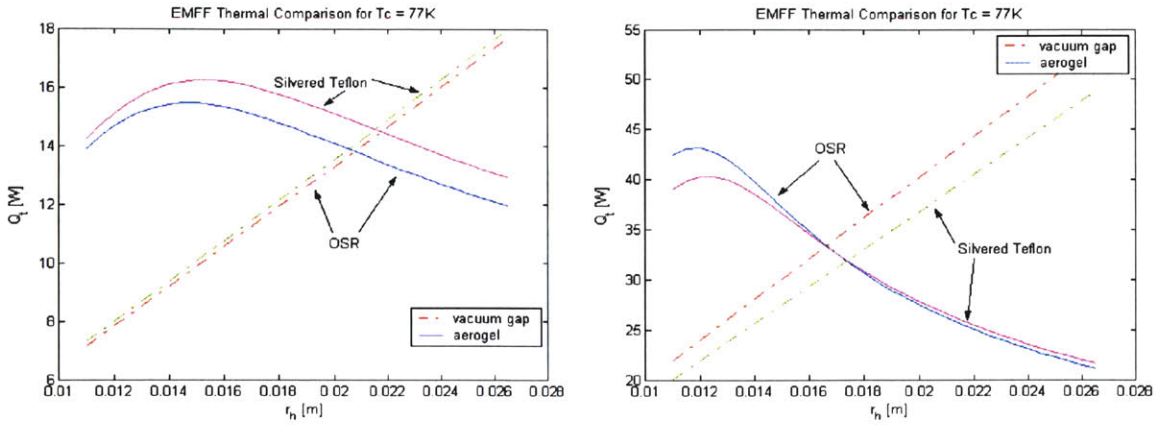

a) b)

Figure 4.14 Material selection comparison for a) Earth trailing orbit, b) LEO

4.2.4 Thermal Subsystem Conclusions

In conclusion, the heat flow into the EMFF coils in the worst case scenario is relatively low (approximately ten Watts), and can be accomplished with a combination of passive and active thermal components, which include insulation or a vacuum-gap and a cryocooler. COTS cryocoolers have a ratio of input power to heat rejection on the order of 20 Watts per Watt. The amount of heat rejection is decreased (less than ten Watts) if the coils that are only partially exposed to the sun.

4.3 Structure

The current EMFF coil model either has them placed tightly wrapped around the spacecraft obviating the need for structural elements or the coils are larger than the spacecraft and are placed around it without consideration for the structure needed to hold them in place. In fact, larger diameter coils are more favorable for generating the maximum electromagnetic force, as long as the support structure is not too massive and the coils can be deployed. The force equation for two identical coil mass and radius spacecraft from Chapter 3 is shown again in Equation (4.27).

$$F_{EM} = \frac{3}{2}\left(10^{-7}\right)\left(\frac{I_c}{\rho}\right)^2 \left(M_c R_c\right)^2 \frac{1}{s^4} \tag{4.27}$$

One metric to evaluate the performance of an EMFF system is the electromagnetic force. However, force produced does not consider the structure necessary to support large coils. A better metric is the system agility, or acceleration, which is the total force produced divided by the total mass. Without structural considerations for the coil, an EMFF spacecraft gains greater agility by increasing its coil size, which increases the force produced. However, when considering the structural elements necessary to hold the coils to the spacecraft bus, the larger the coils, the greater the mass of the structural elements, defined as M_{beams}. Therefore, the structural mass and coil size are two diametrically opposing design parameters for spacecraft agility, which is shown as

$$\ddot{x} = \frac{F_{EM}}{M_{total}} = \frac{\frac{3}{2}\left(10^{-7}\right)\left(\frac{I_c}{\rho}\right)^2 \left(M_c R_c\right)^2 \frac{1}{s^4}}{M_s + M_c + M_{beams}} \tag{4.28}$$

As a simple one dimensional model for the structure, three beams from a spherical spacecraft bus are used to attach to the coils as shown in Figure 4.15. The goal of this static analysis is not to determine the optimum structural configuration, but to understand basic trends between the agility and coil size when considering structural mass.

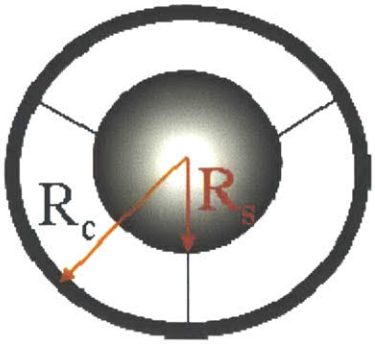

Figure 4.15 Simple three beam configuration for EMFF coil support structures

4.3.1 Beam analysis and trends

The electromagnetic force from a coil is exerted on the end of the beams and uniformly distributed over the number of beams. Modeling the spacecraft as fixed, where the other end of the beam is attached, the beam is assumed to be a cantilevered beam, which is

shown in Figure 4.16. The deflection for the end of a cantilevered beam with solid square cross-sectional area is given by

$$w = \frac{Pl^3}{3EI}, \quad I = \frac{h^4}{12} \tag{4.29}$$

where P is the electromagnetic force divided by the number of beams, l is the length of the beams and E is the Young's Modulus of the beams. A solid cross-sectional area is used for simplicity. To reduce the mass of the beam, one could consider a beam with a hollow square cross-section or I-beams.

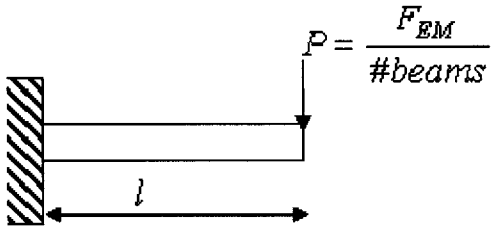

Figure 4.16 Cantilevered beam model

The mass of the beams is given as

$$M_{beams} = \#beams * (R_c - R_s) h^2 \rho \tag{4.30}$$

where h is the height of the beams and ρ is the density of the beam material. In order to non-dimensionalize the allowable deflection, due to the electromagnetic force, as a function of coil size, w is given by

$$w = \delta(R_c - R_s) = \delta l \tag{4.31}$$

where δ is a non-dimensional deflection, R_c is the coil radius and R_s is the spacecraft radius. Substituting Equation (4.27) into Equation (4.29) results in a deflection equation that is a function of the coil radius. Setting this result equal to Equation (4.31) allows the cross-sectional area of the beam to be found as a function of δ

$$h^2 = \sqrt{\frac{2 \cdot 10^{-7}}{E\delta}} (R_c - R_s) \frac{I_c}{\rho_c} \frac{M_c R_c}{s^2} \tag{4.32}$$

Substituting Equation (4.32) into the mass of the beam, Equation (4.30), yields an equation for the mass of beams that is a function of coil radius to the third power. Now the agility equation can be simplified as a function of coil radius as

$$\ddot{x} = \frac{F_{em}}{M_{total}} = \frac{f(R_c^2)}{f(R_c^3, w)} \tag{4.33}$$

To find an optimum coil size, one can take the derivative of the agility with respect to the coil radius. This results in the following cubic equation

$$\frac{d\ddot{x}}{dR_c} = R_c^3 + c_1 R_c + c_o = 0 \tag{4.34}$$

The optimum coil size is numerically solved for according to the spacecraft size, separation, beam material, and deflection constraint. The agility as a function of coil size for a 600 kg spacecraft with a two meter radius spacecraft bus (M_s = 600 kg, R_s = 2 m) at a separation for 25 m (s = 25 m) with Aluminum 6061-T6 beams in shown in Figure 4.17a. The spacecraft mass is based on the mass of a TPF collector spacecraft and the spacecraft separation is based on to the neighbor to neighbor separation of collector spacecraft from the 1999 TPF book [12]. In addition, a coil mass of 10 kg is used. The optimum coil radius is 47.1 m, which is unrealistically large, and operation at the optimum size should not be considered. However, a greater amount of agility is gained by increasing the coils even a small percentage from the spacecraft bus radius. This can be seen in Figure 4.17a where increasing the coil radius in the region of small R_c results in a large increase in acceleration (since the acceleration vs. R_c curve is very steep for small R_c). The deflection constraint can also affect the optimum point, and a tighter constraint reduces the optimum size, as seen in Figure 4.17b.

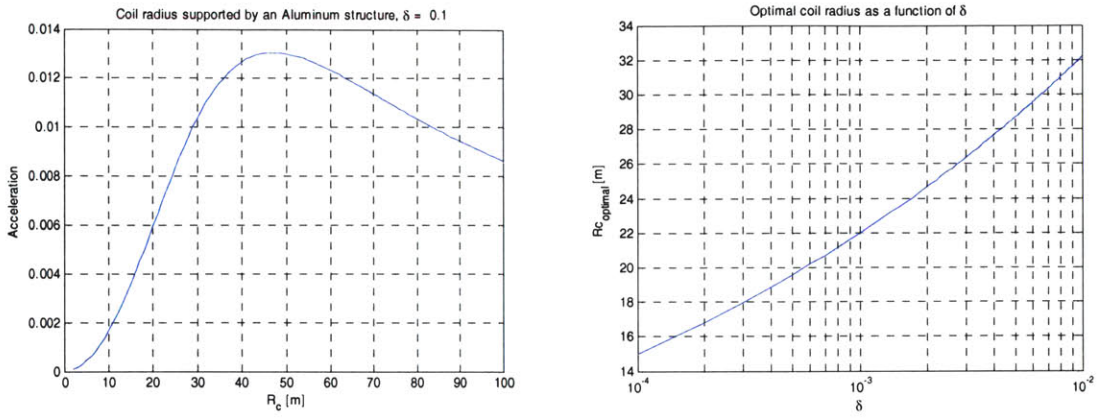

a) b)

Figure 4.17 a) Acceleration versus coil radius, b) Optimal coil radius versus deflection constraint for 600 kg spacecraft, R_s = 2 m, M_c = 10 kg

The main conclusion of the structural analysis is that if the spacecraft has the ability to be equipped with coils that are larger than its nominal bus size, even if only by a small amount, there is a greater amount of agility that can be gained. Possible limitations to the coil size include the launch vehicle shroud and deployment mechanisms. It is feasible for a coil to be larger than the launch shroud if the coil can be folded up and then deployed. Some possible scenarios, which need further investigation, include a coil with hinged sections and non-circular coils.

4.3.2 Future Structural Model Considerations

To create a more accurate model of the beam deflection, the coil and structure really should be modeled dynamically instead of statically. In addition to a more accurate model of deflection, the torsional load on the beams caused by electromagnetic torque between two vehicles should also be considered. The torsional mode would account for the reaction wheels and the coils. Depending on the beam design, the torsional mode could become a more constraining factor than the deflection.

In reality, the three dimensional structure for the EMFF spacecraft consists of three coils connected together. Depending on how the coils are attached together, it is likely that the structure with three coils have a significant amount of added rigidity over a single coil

system. It is possible to have the interlocking coils as the main structure of the spacecraft and connect the bus to the coils using a system of tethers.

4.4 Power

4.4.1 Design Overview

Superconducting wire allows for high strength magnetic fields to be created by providing the coils with high current. The magnetic moment is a function of current, so the force created increases with current squared. The HTS coil acts as a large inductor with zero resistance in a circuit while it is superconducting. Current through the coil, not the voltage, is the critical factor and for low power consumption, the voltage is kept relatively low. The only resistance in the circuit occurs in the power system's internal resistance, for example in batteries, wiring and mosfets. Therefore, the design of the power system must minimize this internal resistance, but also be capable of supplying high current at low voltages with enough accuracy to satisfy control requirements. In addition, since the magnetic field must have the ability to switch polarity, the current through the coil must be driven both in forward and reverse directions.

The power system that meets these constraints is an H-bridge design which is shown in Figure 4.18 where the electromagnet is the high current load. The figure shows current driven in one direction by closing a pair of switches. Likewise, the current can be driven in the reverse direction by switching the open and close positions. A current sensor in series with the electromagnet can be used to measure the coil current and with logic hardwired into the power circuit it is possible to regulate the current flow.

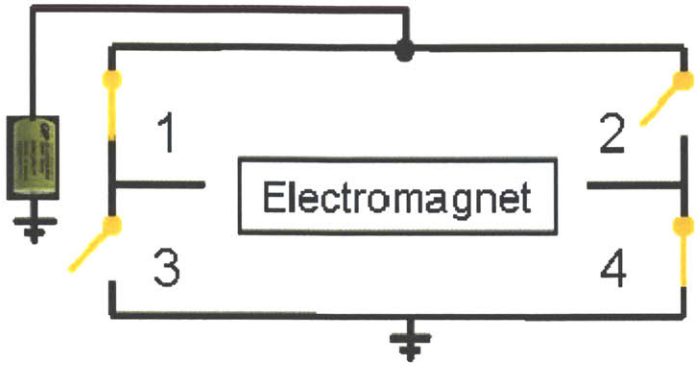

Figure 4.18 Power system setup

The EMFF testbed power circuit currently operates using the design shown in Figure 4.18 with current sensor and logic. The H-bridge mosfet driver is the HIP4081A made by Texas Instruments, the current sensor is the ACS750 made by Allegro, and the mosfets used are the HUF7614 made by Fairchild Semiconductor. The current source for the system is a set of high energy density Nickel Metal Hydride (NiMH) D-cell batteries, which can provide 45 Amps of continuous current discharge and up to 120 Amps momentarily. The next sections determine the power consumption by the EMFF power system experimentally and through analysis.

4.4.2 Experimental Calculations

The first implementation of the EMFF power system used a pulse width modulation signal (PWM) to constantly drive current from the batteries into the coil. To regulate a steady state coil current, current was also constantly pumped back into the batteries to charge them. This system had a duration of approximately 20 minutes and required nine total batteries consisting of three parallel sets of three batteries connected in series as seen in Figure 4.19. Because current was constantly charged and discharged, the system was relatively hot and required fans to cool the mosfets.

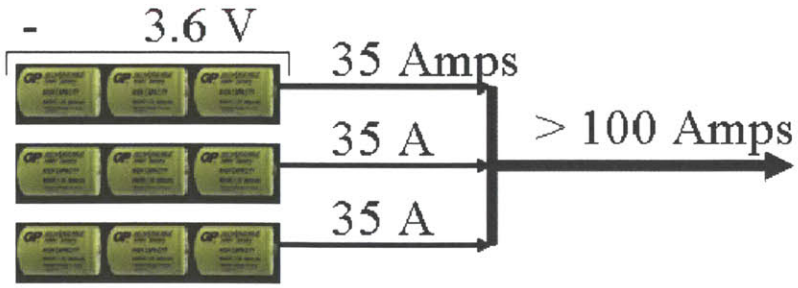

Figure 4.19 Original power system battery configuration

An improved design has been implemented using the same H-bridge circuitry, but exploiting logic built into the mosfet driver. A free wheeling or coasting state is achieved where the current in the coil is confined to a closed circuit and the battery set is taken out of the circuit. An example of the free wheeling state is seen in Figure 4.18 by closing switch 3 and opening switch 1 immediately after current is pumped into the electromagnet from the batteries. During the free wheeling state, the system represents an L-R circuit, where the resistance in the system comes from the closed mosfets and wiring. This mode of operation allows the batteries to only be in the circuit periodically to pump current while the rest of the time is spent free wheeling. An example of this is seen in the two graphs in Figure 4.20. The upper graph shows the PWM input signal which is set high to five volts when the batteries are pumping current into the coils. The circuit is running at a 10% duty cycle with a frequency of 0.1 Hz. This means that the batteries are in the circuit for ten percent of a full period, whose frequency is 0.1 Hz. The fraction of the time spent free wheeling is the duration of the full period that the batteries are out of the circuit. Therefore, the duty cycle and free wheeling time fraction add to unity

$$\text{Duty Cycle} + \text{Free Wheeling Time Fraction} = 1 \tag{4.35}$$

The lower graph of Figure 4.20 shows the response of the battery current (solid blue) and coil current (dotted red) to the PWM input signal as a function of time. Since the batteries and mosfets are not constantly switching like in the previous design, the overall system is much cooler and does not require any cooling fans. In addition, only a single set of three batteries in series is necessary for operation. Currents higher than 45 amps

are achieved by periodically pumping current into the coil. Figure 4.20 shows the coil and battery operating at frequency that enables one to easily determine the time constant. During actual tests, the operating frequency is typically 10 Hz.

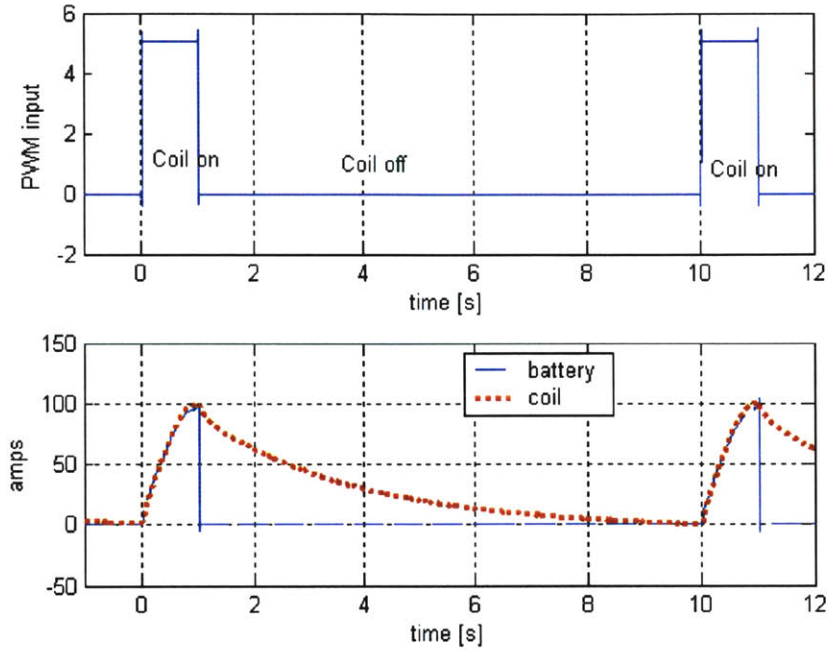

Figure 4.20 Coil and battery operation, 10% duty cycle at 0.1 Hz

The time constant of the current decay in the L-R circuit is measured from Figure 4.20 and is used to determine the power dissipated in the system. The power, P, of the system during the free wheeling state is a function of the current through the coils and the total resistance, R, of the system. The time constant, τ, and the inductance of the coil, L, are used to determine R,

$$P = i^2 R$$
$$\tau = \frac{L}{R} \rightarrow R = \frac{L}{\tau} \tag{4.36}$$

where L for a helical coil shown in Figure 4.21 is given by Wheeler [20] as

$$L[\mu\text{H}] = \frac{\left(nR_c[\text{in.}]\right)^2}{9R_c[\text{in.}] + 10H[\text{in.}]} \tag{4.37}$$

Here the coil geometry is given in English units and the inductance is in micro-Henries. For the EMFF testbed, the radius of the coil, R_c is much larger than the height of the helix, H, which is approximated by the HTS wire width (R_c = 0.424 m >> H = 0.004 m). Using this approximation and converting to SI units, the inductance of the coil is

$$L[\mu\text{H}] \simeq 39.37 \frac{n^2 R_c[\text{m}]}{9} \tag{4.38}$$

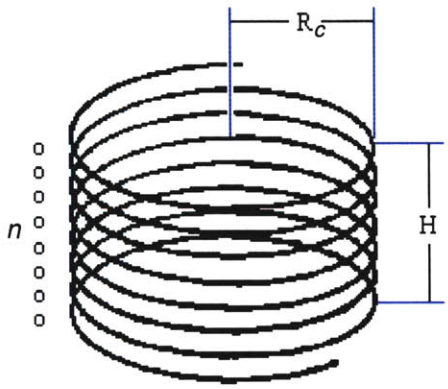

Figure 4.21 Helical coil

The power during the free wheeling state is approximately 55 Watts while operating at a current of 85 Amps. The results are summarized in Table 4.4 and the next section validates this approximation with analysis.

Table 4.4 EMFF testbed coil parameters and experimental power results

Turns, n	100
Coil Radius, R_c, (m)	0.424
Inductance, L, (Henries)	0.0186
Time Constant, τ, (sec)	2.43
Total Resistance, R, (mOhm)	7.65
Current, i, (Amps)	85
Power, P, (Watts)	55.3

A similar method exists to calculate the power using the HTS technology parameter. First, Equation (3.5) is solved for the current in the conductor, which yields

$$i = \frac{I_c}{\rho_c}\frac{M_c}{2\pi n R_c} \tag{4.39}$$

Then substituting Equations (4.38) and (4.39) into Equation (4.36) to find the power,

$$P = i^2 R = \left(\frac{I_c}{\rho_c}\frac{M_c}{2\pi n R_c}\right)^2 \left(39.37\cdot 10^{-6}\right)\frac{n^2 R_c}{9\tau} = \frac{39.37\cdot 10^{-6}}{\tau}\left(\frac{I_c}{\rho_c}\right)^2 \frac{M_c}{36\pi^2 R_c} \tag{4.40}$$

The testbed does not operate at maximum I_c/ρ_c and this can be determined from Equation (3.5) as

$$\frac{I_c}{\rho_c} = \frac{2\pi n i R_c}{M_c} \tag{4.41}$$

The mass of the coil is 2.44 kg and has 100 turns. For a current of 85 Amps, the I_c/ρ_c is 9288 A·m/kg resulting in a power of 55.3 Watts. This result is the same as the result from Table 4.4 since the same coil parameters and time constant are used. Equation (4.40) is used to determine the maximum power needed for an EMFF system given the coil parameters, HTS technology, and time constant of the power system. The theoretical maximum power needed for the testbed is 169 Watts if maximum current (115 A) is allowed through the conductors assuming no reduction in I_c from the HTS magnetic field at 77 K.

4.4.3 Theoretical Analysis

An alternative method of calculating the dissipated power, independent of obtaining the time constant, is accomplished by identifying all sources of resistance in the power system. This is also useful in identifying which components have the highest resistance and could be replaced with lower resistance components in the future. A summary of the various components in the system and their approximate resistance contributions during both the free wheeling state and charging state is seen in Table 4.5.

Table 4.5 EMFF testbed power subsystem component breakdown

				Free Wheeling State	Charging State (battery in the circuit)
Component	Type (company)	Quantity/Length	mOhm per []	Total component Resistance [mOhm]	Total component Resistance [mOhm]
Current sensor	ACS750 (Allegro)	1 [-]	0.13 [sensor]	0	0
Mosfet	HUF76145 (Fairchild)	2 [-]	4 [mosfet]	8	8
Wiring	12 gauge	0.5 [m]	1.6 [m]	0.79	0.79
Copper studs	4 gauge	0.083 [m]	0.25 [m]	0.0207	0.0207
Interconnects	8 gauge	0.167 [m]	0.63 [m]	0	0
Interconnects	12 gauge	0.167 [m]	1.6 [m]	0.26	0.26
Battery	GP900DH (GP Batteries)	3 parallel sets of 3 batteries in series	6 [battery]	0	6
			Analysis Resistance, R [mOhm]	**9.08**	**15.08**
			Power (i = 85 A)	65.6 Watts	108.9 Watts

The overall resistance of the system estimated by analysis during the free wheeling state (9.08 mOhm) is higher than the experimental resistance (7.65 mOhm). As a result, the power estimated by analysis (65.6 W) is approximately ten Watts higher than the experimental power (55.3 Watts). This difference is most likely due to an overestimate on the wiring lengths and the mosfet resistance. The resistance of the mosfet is dependant on the temperature of its operation as seen in Figure 4.22 [21]. Since the mosfets are cooled by liquid nitrogen boil off during experimental operation, it is conceivable that the mosfet resistance is as low as 3.5 milliOhm, which reduces the power obtained by analysis from 65.6 Watts to 58 Watts. This result is much closer to the experimental results. Overall, the main conclusion is that the power required for an EMFF system is relatively low (on the order of 50 to 100 Watts) and does not seem to pose a problem for space applications.

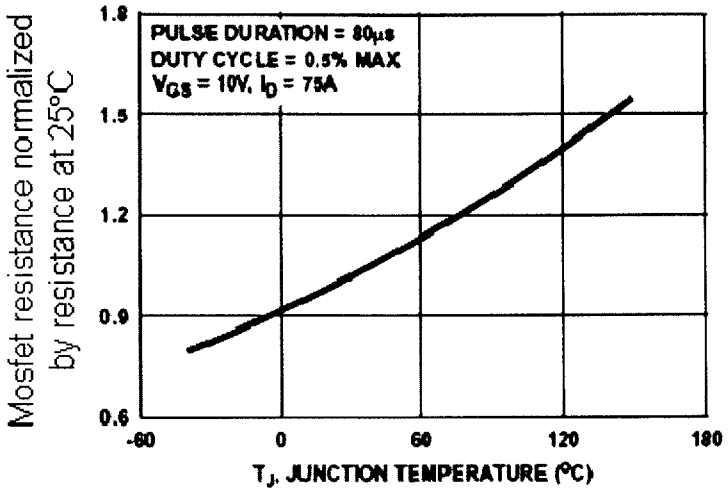

Figure 4.22 Resistance of mosfet as a function of temperature [21]

The final step is to determine the battery duration for the power system. The power consumed while pumping current into the coil includes the resistance of the battery, which is seen in Table 4.5. The resistance of the batteries adds approximately 6 mOhm, which increases the power to 109 Watts. As a result, the average power is higher. Charging occurs approximately 10% of the coil operation time (only when the battery is in the circuit). The average power dissipated while operating at a 10% duty cycle is then found to be

$$P_{average} = 0.1\ (\text{duty cycle}) \cdot 109\ \text{Watts} + 0.9\ (\text{free wheeling time fr.}) \cdot 65\ \text{Watts} = 70\ \text{Watts} \qquad (4.42)$$

Using the average power dissipated, the average current draw from the batteries is

$$I_{average} = \frac{\text{Power Dissipation}}{\text{Battery Voltage}} = \frac{70}{3.6} = 19\ \text{Amps} \qquad (4.43)$$

where the battery voltage is achieved by using three 1.2 volt D-cell batteries in series. The battery duration is now the product of the total energy per battery times the number of batteries divided by the average current draw

$$\text{Duration} = \frac{\#\ \text{Batteries} \cdot \text{Total Energy per Battery}}{\text{Average Current from Battery}} = \frac{3 \cdot 9\ [\text{A} \cdot \text{h}]}{19} = 1.42\ \text{Hours} \qquad (4.44)$$

where the total energy per battery is 9 Amp hours. The calculated battery duration is almost 1.5 hours which is over four times longer than the duration of the original power system design. Additional duration can be achieved by adding more batteries or decreasing the resistance of the system, which can be achieved by implementing lower resistance mosfets or reducing cabling.

4.5 Avionics Performance using GPS

One of the concerns of EMFF is possible adverse effects of the magnetic fields on electronics. This section summarizes an experiment that tested avionics hardware using the EMFF testbed. A possible payload sensor of an EMFF satellite is the Global Positioning System (GPS). Several experiments were carried out to determine the performance of GPS in an EMFF system. The GPS system used was the Canadian Marconi Company Superstar Development Kit, which contains a 12 dB active GPS antenna with a 20 foot cable. A single EMFF coil was used to provide the electromagnetic field. Schematics of the tests are shown in Figure 4.23. Tests occurred on the roof of an MIT building to ensure a clear signal from the GPS satellites. Figure 4.24 shows pictures of the tests containing the positions of the cable, antenna, and receiver and the current flowing through the coil in amps on the multimeter.

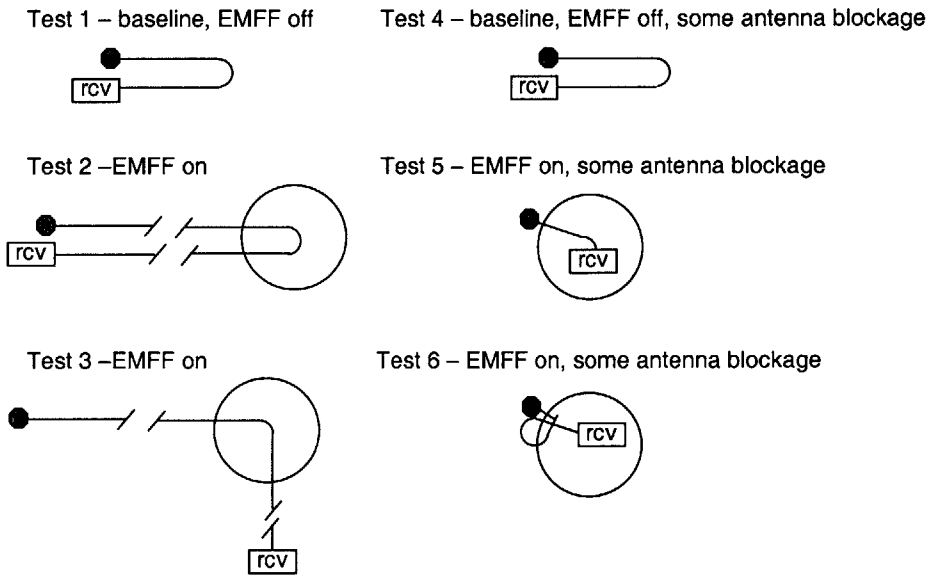

Figure 4.23 GPS test scenarios

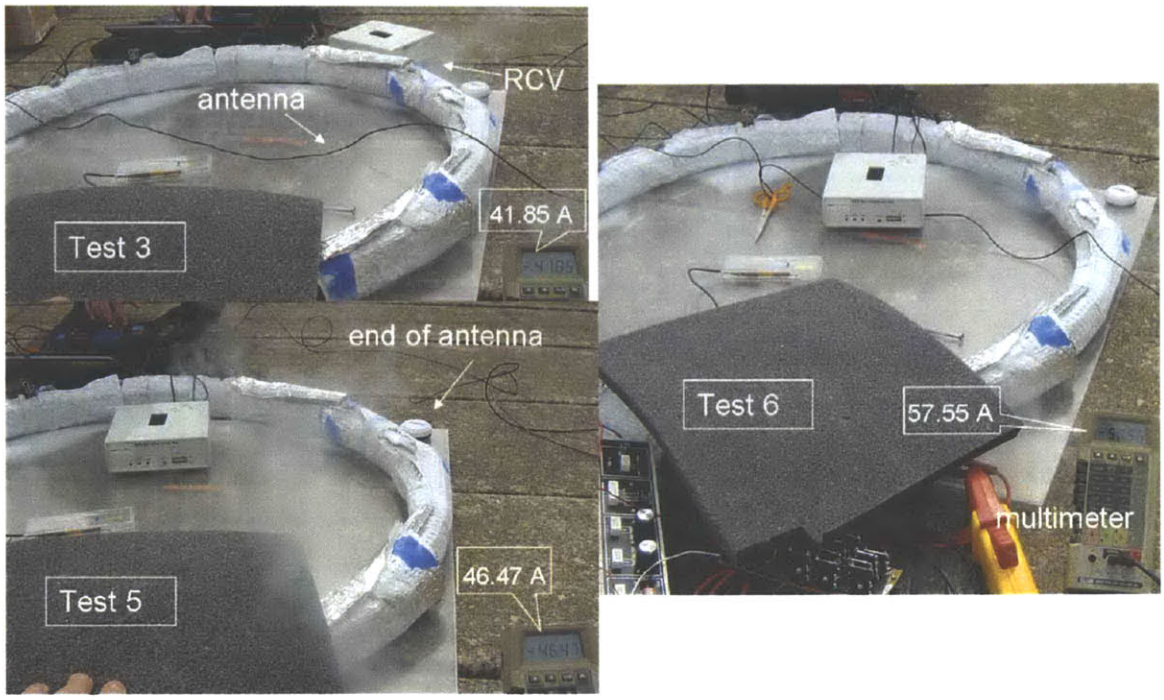

Figure 4.24 GPS experimental test setups

The antenna had a clear field of view during the first three tests. After a baseline test (Test 1), the antenna wire was passed through the field in two configurations. In each of the first three tests, seven to nine satellites were seen and SNR levels did not drop after the EMFF coils were turned on. The antenna and receiver were brought near the EMFF coil for tests 4-6 with the antenna ring alongside the outside of the coil and the receiver inside the coil. This configuration more closely resembles how GPS would be configured on a satellite. In addition, the antenna and receiver were near the coil since the field created is strongest right next to the coil. The number of satellites that the receiver was able to track dropped to six or seven, likely because of the blockage cause by a nearby rooftop building and the experimenters. Again, SNR levels were not affected by the EMFF field. The EMFF coil was operating at between 41 to 58 Amps for tests two, three, five, and six which is approximately half the capacity of the HTS wire and generates a field on the order of 50 Gauss [9]. Results of the test are also shown in Figure 4.25. It is important to observe that the SNR levels are relatively constant throughout the test, since the SNR is a better indication of the effects of EMFF as opposed to the appearance and disappearance of different satellites. These preliminary

tests indicate that the effect of the EMFF field on the GPS performance is minimal. The testing duration was relatively quick, approximately ten minutes. For a flight system, a longer duration test with more sensitive GPS equipment would be necessary to fully validify the performance of GPS in an EMFF system.

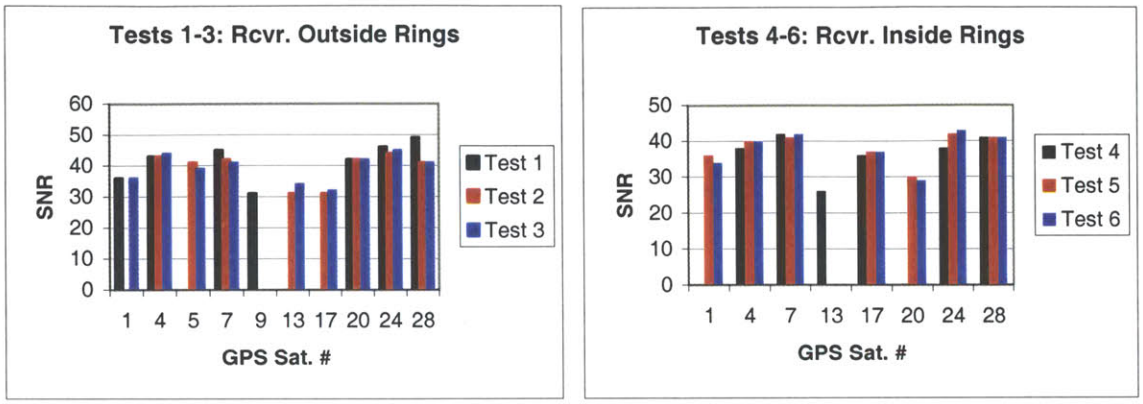

Figure 4.25 GPS test summary

In addition to operating GPS in an EMFF system, the Motorola Tattletale microprocessor and two radio frequency (RF) communication boards (DR-1012-DK and DR-2000 models by RF Monolithics) have been tested in the EMFF testbed and were no affected by the magnetic field. The RF communication boards did not experience any loss of packets when tested inside the EMFF vehicle with a field of approximately 50 Gauss. Under these same conditions, the Motorola Tattletale did not experience any problems. To obtain more quantitative results, future tests can be conducted to determine the effect, if any, of the magnetic field on the number of instructions per second by the microprocessor and the effect, if any, of the magnetic field on the bits per second transmitted by the communications boards.

4.6 Subsystems Summary

Several subsystem issues regarding EMFF have been explored in this chapter. These included the effect of temperature and magnetic field on the HTS wire, the thermal designs for insulating and cooling the HTS wire, the effect on agility posed by structural

components holding the coil to the spacecraft, the amount of power required by EMFF, the overall power design, and the effect of EMFF on avionics.

In Section 4.1, the variation in the critical current density, I_c, due to the magnetic field from neighboring HTS wires and the operating temperature was introduced. The magnetic field that is seen by the HTS wires reduces the critical current. In contrast, there is a significant increase in critical current by the HTS wires that can be achieved by operating at lower temperatures. It was shown that spacecraft can achieve a six times improvement in acceleration by operating at 40 K compared to the acceleration at 77 K for HTS where the effect of the magnetic field is not considered. In addition, there is a linear relationship between the total loop current and the number of turns, even for the case of 10,000 turns.

In Section 4.2, thermal design of the EMFF coils using insulation and a vacuum gap was investigated. Overall, these designs required approximately ten Watts of heat flow to be rejected. This was accomplished using COTS cryocoolers; one particular cryocooler had a mass of 2.7 kg and a power of 150 Watts. The thermal insulation is highly dependant on the material properties, geometry, and orbit.

The structures analysis showed that the agility of a spacecraft can be increased by making the coils larger. The optimum coil radius is significantly larger than the spacecraft bus. However, increasing the coil radius, even by a small percentage, results in a significantly higher acceleration.

The power system required to drive current through the coils is on the order of fifty to one hundred watts per coil for the EMFF testbed. Advances in lower resistance circuitry can help improve future systems. Finally, the performance of avionics in the presence of EMFF fields was tested using GPS equipment. A fifty Gauss magnetic field was produced by the MIT-SSL EMFF testbed and did not impact the signal to noise ratio obtained by the GPS receiver.

Chapter 5

TPF APPLICATION

The cornerstone mission of NASA's Origins program is the Terrestrial Planet Finder (TPF). A possible design for the mission is a four-aperture Michelson interferometer with a resolution capable of viewing extra-solar planets. The entire system consists of five spacecraft, where the center spacecraft is a combiner. One possible configuration is a collinear array shown in Figure 5.1, with each aperture (collector spacecraft) at equal separation distances and with the combiner in the center of the array. In order to detect planets, the array must rotate to fill the Fourier (u-v) plane. Current TPF designs use high I_{sp} thrusters on each spacecraft for this purpose. The faster the array rotation, the more images it can collect, and the more science that can be conducted (assuming that the interferometer maintains the necessary signal to noise ratio to obtain images). Unfortunately, increasing the rotation rate puts a greater demand on the propulsion system and more propellant must be expended. Then, consumables may limit the mission duration and consequently the science returns for TPF.

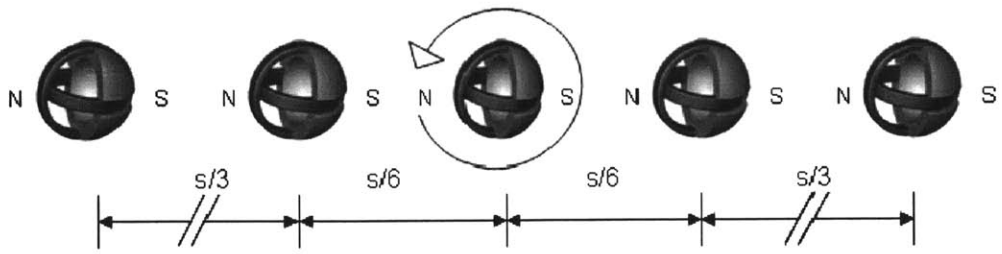

Figure 5.1 Five spacecraft TPF design using EMFF

This chapter applies the EMFF system designs from the previous chapters to the current design for TPF to understand how EMFF trades with current propellant-based options. The goal of this chapter is to show that EMFF is a more practical propulsion technology than high I_{sp} thrusters, when using mass as a metric for a variety of mission parameters such as lifetime, baseline, and rotation rate. To create a convincing argument, it is not

enough to only compare the amount of propellant consumed versus the EMFF coil mass, since the different propulsive options are closely coupled with other subsystems such as the attitude control subsystem (ACS), power, and structures. Therefore, the high temperature superconducting (HTS) coil, the main "propulsive" component for EMFF, is modeled with its associated ACS, power, and structures subsystems. It is important to understand how the EMFF related subsystems affect the total EMFF system budget and how they are affected by mission parameters. In addition, determining how the EMFF and micropropulsion systems affect the total mass of the array is useful for future designs of TPF.

5.1 Overview of original model

The TPF model in this chapter builds on the work of Kong and Kwon [22] for the electromagnetic system design and Reichbach [1] for the micropropulsion systems design. This section provides a brief introduction to the previous model and its results.

The micropropulsion systems analyzed were cold gas thrusters, colloids, Pulse Plasma Thrusters (PPTs) and Field Emission Electrostatic Propulsion thrusters (FEEPs). For the propellant-based options, the mass of each spacecraft was broken into the dry mass of the spacecraft (m_{dry}), the mass of the propulsion system ($m_{propulsion}$), the mass of the propellant ($m_{propellant}$), and the mass of the solar array (m_{SA}). To ensure fair comparison of the overall mass for the various formation flight options, the mass of the solar array panel associated with the peak power required to operate the propulsion was also included. As such, the mass of each spacecraft in an array that utilizes a propellant-based system was given by

$$m_{sc} = m_{dry} + m_{propulsion} + m_{propellant} + m_{SA} \tag{5.1}$$

The key equations used to design the micropropulsion systems are shown in Table 5.1. More detailed descriptions of the equations and the constants can be found in the appendix of Reichbach [1]. The 1999 TPF book [12] was used to determine the dry mass of each collector spacecraft (600 kg) and the dry mass of the combiner spacecraft (568

kg). The specific impulse of each thruster is shown in the third row of Table 5.1. The total dry mass ($m_{dry_{total}}$) used to determine the mass of the propellant is

$$m_{dry_{total}} = m_{dry} + m_{propulsion} + m_{SA} \tag{5.2}$$

Table 5.1 Summary of key equations for the micropropulsion systems

	PPT	Colloids	FEEPs	Cold Gas
m_{dry} [kg]	600 (Collector), 568 (Combiner)			
I_{sp} [s]	$\frac{2500E_o^{1.6}}{10^6 I_{bit}} = 1375$	$\frac{1}{g_o}\sqrt{2\frac{q_d}{m_d}V_{nominal}} = 1354$	$\frac{1}{g_o}\sqrt{\frac{2eV_e}{m_{Cs}}} = 6000$	65
$P_{propulsion}$ [W]	$E_o PRF_{max}$	$P_{neutral} + P_{thruster} = 500N_N I_N + \frac{1}{\eta} I_N V_N V_{max}$	$P_{neutral} + P_{thruster} = 500I_E + I_E V_E + I_A V_A$	15
m_{SA} [kg]	$\frac{P_{propulsion}}{P_{specific}} = \frac{P_{propulsion}}{25\frac{W}{kg}}$			
$m_{propulsion}$ [kg]	$N_{\frac{thruster}{s/c}}\left(m_c + m_{dic} + m_s + m_{ppu}\right)$	$N_{\frac{thruster}{s/c}}\left(m_c + m_s + m_{ppu}\right)$	$N_{\frac{thruster}{s/c}}\left(m_c + m_s + m_{ppu}\right)$	$N_{\frac{thruster}{s/c}} m_s + m_{feed}$
$m_{propellant}$ [kg]	$\frac{m_{dry_{total}} m_{shot} \Delta V}{I_{bit}}, m_{shot} = \frac{I_{bit}}{I_{sp} g_o}$	$m_{dry_{total}}\left(1 - e^{-\left(\frac{\Delta V}{I_{sp} g_o}\right)}\right)$	$m_{dry_{total}}\left(1 - e^{-\left(\frac{\Delta V}{I_{sp} g_o}\right)}\right)$	$m_{dry_{total}}\left(1 - e^{-\left(\frac{\Delta V}{I_{sp} g_o}\right)}\right)$
Details	capacitor energy (E_o), minimum impulse bit (I_{bit}), Pulse Repetition Frequency (PRF_{max}), capacitor mass (m_c), discharge circuitry mass (m_{dic}), structure mass (m_s), power processing unit mass (m_{ppu})	droplet charge to mass ratio ($\frac{q_d}{m_d}$), nominal needle voltage ($V_{nominal}$), number of needles (N_N), single colloid needle current (I_N),	emitter voltage (V_e), Cs ion mass (m_{Cs}) emitter current (I_E), emitter voltage (V_E), accelerator current (I_A), accelerator voltage (V_A)	feed system mass (m_{feed})

For EMFF, designs using a room temperature copper coil and a HTS coil at 77 K were both investigated. The mass of each spacecraft utilizing EMFF was given by

$$m_{sc} = m_{dry} + m_{coils} + m_{SA} \tag{5.3}$$

where the mass of the coil is m_{coils}. The same dry mass of the collector (600 kg) and combiner (568 kg) and the same solar array specific power ($P_{specific}$ = 25 W/kg) was used for the EMFF design. The power required by the EMFF coils was 400 Watts, a number estimated by Kong and Kwon. The mass of the coils was based on the concept of maximizing mission efficiency shown in Chapter 3.

The results for the EMFF and micropropulsion systems are shown in Figure 5.2 where the overall system mass for all five spacecraft is shown as a function of the mission lifetime for a two hour rotation period at a 75 m baseline (s = 75 m). For all the propellant-based systems, the plot clearly indicates an increase in overall system mass as the mission lifetime is extended. In order to keep the array rotating, propellant is required to provide the centripetal loads that are needed by the respective spacecraft. It is important to note that TPF plans for component reliability for five years and consumables for ten years. This means that the core science goals are met in the first five years, while the last five years are allocated for extended science goals. The results did not incorporate reliability, but indicate the total mass required for a ten year mission.

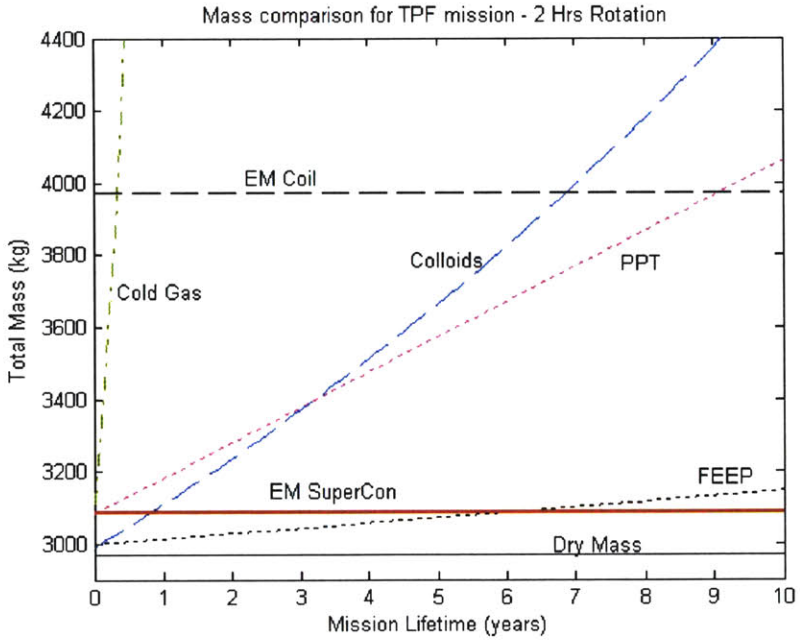

Figure 5.2 Mass comparison for TPF using various propulsion systems (two hour rotation period) [22]

There are several key observations from this initial study. First, the EM superconducting (HTS) design was the most favorable option for the mission when considering mass. This considers planning for a ten year mission based on consumables. Second, the room temperature copper coils did not trade well compared to the superconducting design even though it compares more favorably than colloids or PPTs for long duration missions

when considering mass. In addition, relatively large radius coils (10 m) were required by the copper coils to provide the necessary forces compared to the superconducting coils (2 m) [22]. Third, the high propellant expenditure rates seemed to rule out the use of the low specific impulse cold gas option (I_{sp} = 65 s). When higher specific impulse systems were used, less propellant was required, thus these were more attractive propellant-based options. Because of this, cold gas thrusters are no longer investigated in the higher fidelity model.

5.2 Higher Fidelity Model

5.2.1 Overview

The goal of the higher fidelity model is to design TPF with greater subsystem detail than the original model for both the EMFF and micropropulsion systems. The starting point for the model consists of mass and inertia data for a collector spacecraft that have been updated since the 1999 TPF book [23]. The subsystems common to both the JPL model and the higher fidelity EMFF and micropropulsion models are shown in Table 5.2. These common subsystems consist of the entire collector payload and most of the collector spacecraft subsystems and form the starting dry mass, m_{dry}, for both the EMFF and micropropulsion models. The subsystems that make up the collector spacecraft are listed in greater detail in Table 5.3.

The subsystems that are different from both the JPL model and the higher fidelity EMFF and micropropulsion models are also shown in Table 5.2 under the section called 'Different Subsystems.' The EMFF and micropropulsion models diverge from the JPL model for those subsystems whose mass vary with baseline, mission lifetime, and rotation rate. The following are the three subsystems from the JPL model that are modeled differently by the EMFF and micropropulsion systems. First, the Reaction Control Subsystem (RCS) mass (156.6 kg) in the JPL model is not part of the EMFF RCS mass or micropropulsion RCS mass. Instead, the mass for the EMFF RCS is denoted by m_{coils} and the masses for micropropulsion RCS are denoted by $m_{propulsion}$ and $m_{propellant}$. All the symbolic masses denoted in Table 5.2 are determined later in the chapter. The second

different subsystem is the attitude control subsystem. The EMFF and micropropulsion models do not consist of the entire ACS components that are part of the JPL collector spacecraft model, as seen in Table 5.2 The one component that is different and is determined by the EMFF and micropropulsion systems separately is the reaction wheel responsible for angular momentum management in the plane of the array rotation. This wheel is denoted by m_{RW}. A single reaction wheel in the JPL model has a mass of 5.96 kg. The third different subsystem is the power system, which is denoted by m_{power} in the EMFF model and m_{SA} in micropropulsion models. The power subsystem mass for EMFF consists of both the solar arrays and coil power processing units. The power subsystem mass for the micropropulsion systems consist of only the solar arrays. The power processing unit mass for the micropropulsion systems is included in $m_{propulsion}$, as seen in Table 5.1.

Table 5.2 Subsystems used in JPL, EMFF, and micropropulsion system models

	Subsystem	Mass, JPL model [kg]	Symbol, EMFF system	Symbol, Micropropulsion systems
Common Subsystems	Collector Payload	707.12	N/A	N/A
	Collector Spacecraft	695.27	N/A	N/A
Common Subsystems Total		**1402.39**	m_{dry}	m_{dry}
Different Subsystems	Reaction Control Subsystem	156.56	m_{coils}	$m_{propulsion}$, $m_{propellant}$
	Attitude Control (single Reaction Wheel)	5.96	m_{RW}	m_{RW}
	Power (Solar Arrays)	57.56	m_{power}	m_{SA}
	Structure	0	$m_{structure}$	m_s
Different Subsystems Total		**220.08**	m_{EMFF}	$m_{PropSys}$
TOTAL SPACECRAFT		**1622.47**	m_{sc}	m_{sc}

The structural mass needed by the RCS subsystem is denoted by $m_{structure}$ for the EMFF system. The structural mass needed by the micropropulsion systems' RCS is denoted by m_s, as seen in Table 5.1.

There are some assumptions that have been made about the overall system. No detailed combiner mass yet exists, so it is assumed that the combiner has the same mass as the collector. The operating temperature of TPF is assumed to be 35 K and is maintained by

the sunshields. The rotation rate for TPF is assumed to be target-independent, and is assumed constant throughout the mission lifetime. A nominal rotation period of 4 hours per revolution is assumed, however, this mission parameter will be varied to determine how the spin rate affects the TPF design. All other assumptions will be mentioned during the design of the corresponding subsystem. A summary of parameters used by the EMFF and micropropulsion models is shown in Table 5.4.

Table 5.3 Collector spacecraft subsystem breakdown

Collector Spacecraft Subsystems	Mass [kg]
Structures and Mechanisms	369.94
S/C Thermal Control (Sunshades)	199.63
Command and Data Handling	31.12
ADCS – Star Trackers	4.85
ADCS – Inertial Reference Unit	6.06
ADCS – 3 Reaction Wheels	17.88
ADCS – Other	2.36
Formation Flying Sensors	39.64
RF Communications	16.47
Power – Batteries	7.32
Total	695.27

In summary, the JPL model and the EMFF and micropropulsion models share common subsystems, which have a total mass of 1402.39 kg. The total EMFF system mass can be determined by

$$m_{EMFF} = m_{coils} + m_{RW} + m_{power} + m_{thermal} + m_{structure} \tag{5.4}$$

Combining the EMFF system mass with the dry mass results in the mass for an entire EMFF spacecraft

$$m_{sc} = m_{EMFF} + m_{dry} \tag{5.5}$$

Similarly, the total micropropulsion system mass can be determined by

$$m_{PropSys} = m_{propulsion} + m_{propellant} + m_{RW} + m_{SA} \tag{5.6}$$

and

$$m_{sc} = m_{PropSys} + m_{dry} \tag{5.7}$$

where combining the micropropulsion system mass with the dry mass results in the mass for an entire micropropulsion spacecraft.

Table 5.4 Summary of parameters used in TPF model

Parameter	Quantity	Units
Spacecraft Inertia (I_{veh})	30,400	kg·m^2
Spacecraft Dimensions	15.3 x 15.3	m
Distance Between Center of Solar Radiation and Center of Gravity	1.248	m
Spacecraft Radius (R_s)	1	m
Coil Radius (R_c)	2	m
Baseline HTS Technology (I_c/ρ_c)	16,250	A·m/kg
Number of Thrusters per Spacecraft	16	-
Number of Observations (N_{obs})	453	-
Observational Fraction (η_{obs})	0.75	-
Nominal Spacecraft Power	400	W
Solar Array Specific Power ($P_{specific}$)	66	W/kg

5.2.2 EMFF model

The EMFF system consists of the superconducting coils, solar arrays for the coil power, and structural beams necessary to hold the coils to the spacecraft bus. A flow diagram of the EMFF system design is shown in Figure 5.3. The inputs of the EMFF design are the coil mass, design variables, and constants. These are used to determine the masses in Equation (5.4). The EMFF design consists of fixed masses and fixed powers, which are not affected by the inputs, and variable masses and powers, which vary according to the inputs. The desired rotation rate that the system must achieve is defined as $\omega_{desired}$. For a given coil mass, the rotation rate is calculated. If the rotation rate equals the desired rotation rate, the system masses (coil, power, etc.) that achieve the specified design are now known. The spacecraft bus is approximately two meters in diameter according to a JPL finite element model of the collector [23]. The EMFF coils are sized to be equal to the aperture diameter of four meters, so each coil has a two meter radius.

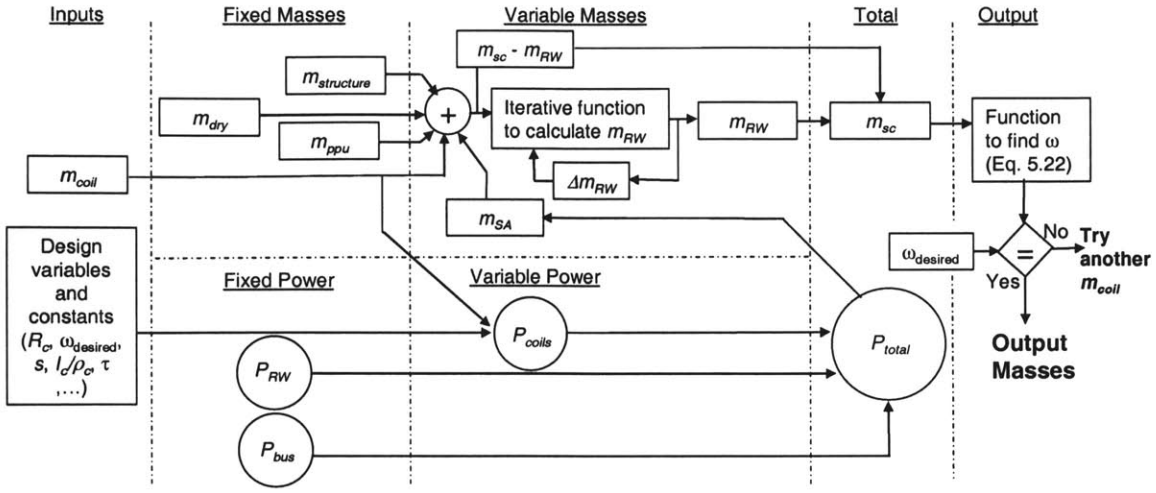

Figure 5.3 Flow diagram of EMFF system design

Structures

The EMFF model includes the beams necessary to attach the three orthogonal coils to the spacecraft bus. The mass of a beam is given by

$$m_{beam} = \rho_{beam} h^2 \left(R_c - R_s \right) \tag{5.8}$$

where the two meter radius coils (R_c) are mounted to the one meter radius spacecraft bus (R_s) resulting in a one meter beam length. The beams have solid square sides, h, and are made of Aluminum. A summary of the quantities unique to the structures subsystem is shown in Table 5.5.

Table 5.5 Structures subsystem parameters

Symbol	Structures Subsystem Parameter	Quantity
h	Length of beam side	0.025 m
N_{beams}	Number of beams	6
m_{beams}	Mass of a single beam	1.75 kg
$m_{structure}$	Structures subsystem mass	10.5 kg
ρ_{beam}	Beam density	2800 kg/m^3 for Al

The mass of a single Aluminum beam is 1.75 kg. Given the total number of beams, N_{beams}, the total structures subsystem mass, $m_{structure}$, is determined by

$$m_{structure} = N_{beams} m_{beam} \tag{5.9}$$

The model uses six beams, which are connected at the coil intersection points. The resulting structures subsystem mass is 10.5 kg and is fixed for all designs.

The beam configuration and its design are relatively simple. Future designs can further optimize the structures design by including a finite element model (FEM) for the coil and beams.

Power

The total EMFF power, P_{total}, consists of the spacecraft bus, coils, and reaction wheel power,

$$P_{total} = P_{bus} + P_{coils} + P_{RW} \tag{5.10}$$

A steady state spacecraft bus power, P_{bus}, of 400 W is selected based on a JPL study [24] that estimated the power for a collector spacecraft during the science acquisition mode for all subsystems except the reaction wheel and propulsion systems. The reaction wheel steady state power, P_{RW}, has a fixed value of 22 W and is discussed in more detail in this section. The power required by the coils, P_{coils}, is determined by

$$P_{coils} = \frac{39.37 \cdot 10^{-6}}{\eta_\tau \tau} \left(\eta_I \frac{I_c}{\rho_c} \right)^2 \frac{M_c}{36\pi^2 R_c} \tag{5.11}$$

given the coil radius, coil mass, HTS technology level, coil power processing unit (PPU) time constant, τ, and coil PPU efficiency, η_τ. A form of Equation (5.11) without η_τ was derived in Chapter Four. For the baseline HTS technology, the time constant, τ, of the MIT-SSL testbed is used which has a value of 2.43 seconds. The coil PPU efficiency is used to model the improvement in the time constant as lower resistance PPUs are developed. This analysis relates the coil PPU efficiency to the variation in I_c, η_I, which was introduced in Chapter 4.

$$\eta_\tau = \eta_I \tag{5.12}$$

The variation in I_c due to the magnetic field and temperature is also used later in this section. Note that the EMFF subsystems related power budget consists of only the coil and reaction wheel power, not the spacecraft bus power.

The total mass of the power subsystem is

$$m_{power} = m_{SA} + m_{ppu} \tag{5.13}$$

where m_{SA} is the solar array mass and m_{ppu} is the total mass of the coil power processing units. Once the EMFF power budget has been determined, the solar array mass necessary for the spacecraft is calculated by

$$m_{SA} = \frac{P_{total}}{P_{specific}} \tag{5.14}$$

The solar arrays used for this design are multi-junction Gallium Indium Phosphide/Gallium Arsenide (GaLnP/GaAs) cells. The solar arrays used in the previous model by Kong and Kwon were Silicon cells with a specific power of 25 W/kg. Multi-junction cells have a specific power of 66 W/kg [25] and are selected because of their more favorable performance. It is assumed that the sun direction is normal to the solar array surface and that the specific power of 66 W/kg includes the conversion efficiency.

The mass of a single coil power processing unit developed at the MIT-SSL is less than 0.5 kg. For a flight system, an approximation of 1 kg is used for the mass of a single coil power processing unit. Each spacecraft consists of three power processing units, one for each coil, resulting in m_{ppu} of 3 kg.

Reaction Wheel

The entire reaction wheel subsystem consists of four reaction wheels and is a combination of the JPL model and this model. This model determines the reaction wheel necessary for momentum storage during array rotation. This wheel is not momentum biased since it will have a large, quasi-steady speed during operation and therefore avoids the friction-stiction transition at zero wheel speed that can cause vibration. In addition to

this one reaction wheel, the EMFF model uses three of the four JPL reaction wheels and assumes that they are responsible for angular momentum management for all other disturbances. The JPL model consists of four orthogonal wheels with a total mass of 23.84 kg [23]. Therefore, the three wheels from the JPL model have a mass of 17.88 kg, as seen in Table 5.3. It is assumed that the JPL wheels are momentum biased. In summary, the EMFF reaction wheel system consists of four reaction wheels; the reaction wheel designed in this section manages angular momentum in the plane of array rotation; the three JPL wheels manage angular momentum in the other planes.

Since TPF is spinning during observations, the array must be "spun up" from relative rest to the desired angular rate. For the array to spin about the center spacecraft with angular rate ω, each collector spacecraft revolves around the combiner with angular rate ω, while also rotating about their respective body centers at that same rate to keep the desired spacecraft face pointing towards the combiner. For the EMFF system, the reaction wheel and electromagnets are used to angularly accelerate the spacecraft about their body centers as well as store the angular momentum associated with angularly accelerating the array as a whole.

Using EMFF to spin the array, no external torques are generated and no propellant is ejected from the system, so conservation of momentum must come from internal momentum storage. It is assumed that the array has zero angular momentum when it is initially at rest. When the array is revolving with angular rate ω, the total angular momentum of the system is the sum of the individual momentum values for the rotating spacecraft plus the momentum of the collector spacecraft in their motion around the combiner.

$$\begin{aligned} I_{tot} &= I_{veh} + 2\left(I_{veh} + m_{sc}\left(\tfrac{s}{6}\right)^2\right) + 2\left(I_{veh} + m_{sc}\left(\tfrac{s}{2}\right)^2\right) = 5I_{veh} + \tfrac{5}{9}m_{sc}s^2 \\ h_{spin} &= I_{tot}\omega \end{aligned} \tag{5.15}$$

Here h_{spin} is the total momentum due to array revolution and spacecraft rotation, I_{tot} is the moment of inertia of the array, I_{veh} is the moment of inertia of each spacecraft about its

center of gravity (CG), s is the baseline of the array, and ω is the spin rate of the array during an observation. Equation (5.15) assumes all five spacecraft have identical masses and moments of inertia. In addition, the collector spacecraft are evenly separated, as seen in Figure 5.1.

The reaction wheel on each spacecraft is also sized for the angular momentum accumulated from solar radiation pressure during one observation, which is one revolution of the array,

$$h_{env} = T_{env}\left(\frac{2\pi}{\omega}\right) \tag{5.16}$$

where solar radiation pressure torque, T_{env}, is given by Mitchell as $2.268 \cdot 10^{-4}$ N·m [26].

Since angular momentum must be conserved, the sum of the momentum of the whole array plus the momentum stored in momentum wheels must be zero. Assuming that h_{spin} is evenly divided between the five spacecraft, the momentum storage for each reaction wheel is

$$h_{rw} = -\left(\tfrac{1}{5}h_{spin} + h_{env}\right) = -\left(\tfrac{1}{5}I_{tot}\omega + T_{env}\tfrac{2\pi}{\omega}\right) = -\left(I_{veh}\omega + \tfrac{1}{9}m_{sc}s^2\omega + T_{env}\tfrac{2\pi}{\omega}\right) \tag{5.17}$$

In order to obtain an estimate of the mass and power of the required momentum wheels for the TPF mission, a representative class of wheels from Honeywell Aerospace is selected for study [27]. The relevant properties for this class of momentum wheel are shown in Table 5.6. Each wheel has a nominal operating torque of 0.2 N·m·s and a maximum torque of 0.4 N·m·s. The steady state power consumption of 22 W for each wheel is identical as well, however this is a conservative assumption based on the Honeywell data sheet and Mitchell [26]. The on-orbit lifetime for these momentum wheels is longer than 15 years. The largest wheel shown can store 150 N·m·s of momentum and has a mass of 15 kg. According to the Honeywell Aerospace data sheet additional sizes of wheels are available, so the mass of current Honeywell wheels and

their respective momentum data is extrapolated using a polynomial fit to size larger wheels. The customized wheel curve is shown in Figure 5.4.

Table 5.6 Properties of Honeywell Aerospace Constellation Series momentum wheels

Name	Momentum Storage (N·m·s)	Nominal Torque (N·m)	Mass (kg)	Steady State Power (W)
HR12-1	12	0.2	6.0	22
HR12-2	25	0.2	7.0	22
HR12-3	50	0.2	9.5	22
HR14-3	75	0.2	10.6	22
HR16-3	100	0.2	12.0	22
HR16-5	150	0.2	15.0	22

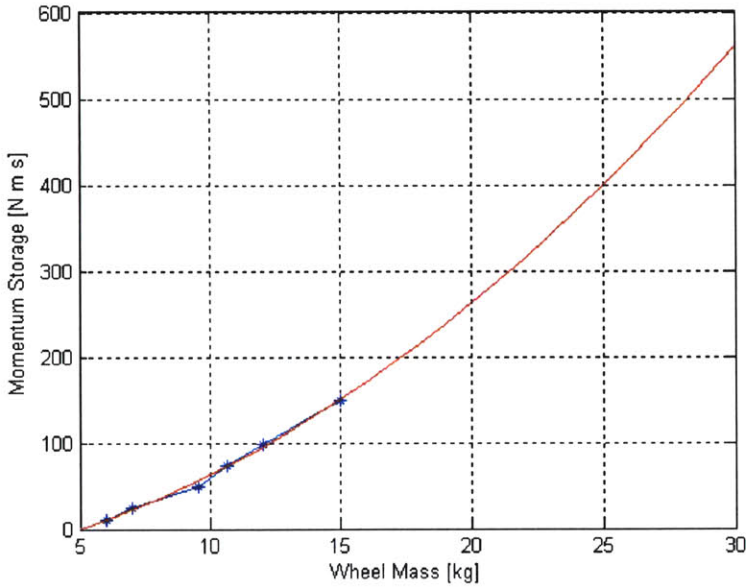

Figure 5.4 Custom reaction wheel curve fit

To choose an appropriate momentum wheel for the TPF mission, the total momentum storage requirement is calculated given the baseline and rotation rate. This includes the momentum storage due to the environmental disturbances and the momentum storage requirement for spin-up. Given the total angular momentum storage requirement, the reaction wheel mass is selected using Figure 5.4. An example of this process is shown

later in this chapter during the analysis of the reaction wheels for the micropropulsion systems.

To ensure that the reaction wheel has sufficient torque, the average angular momentum per spacecraft

$$H_{s/c} = \tfrac{1}{5} I_{tot}\omega = \tfrac{1}{5}\left(5I_{veh} + \tfrac{5}{9} m_{sc} s^2\right)\omega \tag{5.18}$$

is set equal to the angular momentum built-up while spinning up the array,

$$H_{s/c} = \tau_{avg} t_{spin-up} \tag{5.19}$$

and solved for τ_{avg}, which is the time average torque, averaged over all the spacecraft,

$$\tau_{avg} = \frac{I_{tot}\omega}{5t_{spin-up}} = \frac{\left(5I_{veh} + \tfrac{5}{9} m_{sc} s^2\right)}{5t_{spin-up}} \frac{2\pi}{t_{rotate}} \tag{5.20}$$

The time it takes to spin-up the array is $t_{spin\text{-}up}$, and the time it takes for one revolution of the array is t_{rotate}. For a mission with a 75 m baseline, eight hour rotation period, and a two hour spin-up time, τ_{avg} is estimated as

$$\tau_{avg} \simeq \frac{\left(5 \cdot 3.03 \cdot 10^4 + \tfrac{5}{9} 1600 \cdot 75^2\right)}{5\left(2 \cdot 3600\right)} \frac{2\pi}{\left(8 \cdot 3600\right)} = 0.031 \text{ N} \cdot \text{m} \cdot \text{s} \tag{5.21}$$

For this case, the time average torque, averaged over all spacecraft (0.031 N·m·s) is less than nominal torque (0.2 N·m·s) and maximum torque (0.4 N·m·s) provided by the Honeywell reaction wheels. Using this example, it is assumed that the reaction wheels provide sufficient torque for the spin-up of the array. One method of decreasing the amount of torque required to spin the array is to slow down the spin-up time, if it is discovered that there is insufficient torque.

One unique feature of the EMFF system is the ability to distribute the total angular momentum among the spacecraft in multiple ways. For example, instead distributing the

total angular momentum equally among each spacecraft, it is possible to distribute the angular momentum so that the majority of it is on the center spacecraft and the rest of it is equally distributed among the collector spacecraft. Current work is being conducted by Schweighart to understand the methods of distributing angular momentum among multiple spacecraft [10]. This research could lead to wheels that are specifically designed for each spacecraft's unique mass and inertia properties possibly resulting in a lower overall system mass. One can envision storing the majority of the angular momentum on the combiner and inner collectors, resulting in large wheels on these spacecraft and allowing the outer collectors to achieve a higher agility.

Coil

To determine the mass of the coils, the force generated by the coils must be equal to the centripetal force of the array during rotation as was seen in Chapter 3. For an array of five spacecraft with separations shown in Figure 5.1, this becomes

$$F = \frac{3}{8\pi}\mu_o\left(\eta_I \frac{I_c}{\rho_c}\right)^2 \left(M_c R_c\right)^2 \frac{1649}{16 s^4} = m_{tot}\omega^2 \frac{s}{2} \tag{5.22}$$

where the $\frac{1649}{16}$ factor comes from the bridging of the magnetic fields from all the EMFF spacecraft in the array. It is assumed that all five EMFF spacecraft have an identical coil mass, coil radius (R_c), total spacecraft mass (m_{tot}), HTS technology level (I_c/ρ_c), and HTS operating temperature. This enables the collector spacecraft to reconfigure to different positions in the array if necessary. The effect of the HTS operating temperature and magnetic field on the critical current density (I_c) is η_I. Given the radius of the coil, baseline (s), array rotation rate (ω), the total spacecraft mass, and HTS technology level, the mass of the coil can be found. The mass of the subsystems are determined first since the total spacecraft mass is needed for the calculation. In other words, the total mass that is accelerated by the coil includes the coil mass, dry mass and all subsystems. It is important to note that Equation (5.22) is used to determine the mass of the single coil necessary to generate the force along one axis. To control three degrees of freedom, three of these coils are used. Therefore, the total mass of the coils, m_{coils}, is

$$m_{coils} = 3 \cdot M_c \tag{5.23}$$

Since the rotation of the array takes place in a single plane, all three of the coils do not necessarily need to be identical. It is possible to configure the coils so that the two coils responsible for maintaining the centripetal force in the plane of the array rotation are stronger (i.e. more massive) than the one coil that provides force out of the plane of rotation. For simplicity, this analysis assumes all three coils have identical mass.

For fixed mission parameters (baseline and rotation rate) and fixed spacecraft properties (coil radius and total spacecraft mass) there are two ways the coil mass, M_c, can vary. The first way is to analyze different HTS technology levels. The baseline HTS technology level, I_c/ρ_c, for COTS superconducting wire is 16,250 A·m/kg. This analysis investigates operating at the baseline technology level and three times the baseline technology level. Higher technology levels can be achieved either by implementing more expensive wire or by superconducting wire technology maturation.

The second way to vary M_c to analyze η_I, the I_c due to the magnetic field and operating temperature normalized by the I_c due to no magnetic field at 77 K, which was defined in Equation (4.7). The magnetic field acts to reduce η_I, and reducing the operating temperature acts to increase η_I. First, the number of turns must be determined so that the effect of the magnetic field on I_c can be found. From Equations (3.3) and (3.5), the number of turns is a function of the coil mass

$$n = \frac{1}{A_c \rho_c} \frac{M_c}{2\pi R_c} \tag{5.24}$$

To determine an estimate for the number of turns required for a single coil, the following example is considered. A five kg, two meter radius coil (M_c = 5 kg, R_c = 2 m) using HTS wire with a density of 8000 kg/m^3 and cross-sectional dimensions of 0.004 m x 0.00025 m (ρ_c = 8000 kg/m^3, A_c = 10^{-6} m^2) results in approximately 50 turns.

Using Equation (4.3), the magnetic field at the end of a HTS stack from 50 turns is

$$B_{50} \simeq 0.22 \text{ Tesla} \tag{5.25}$$

Given the magnetic field acting on the HTS wire, η_I is determined for various temperatures using Figure 4.1a in Chapter 4. A summary of these results is seen in Table 5.7. It is assumed that the operating temperature for TPF is 35 K and that the sunshield for TPF provides the only means for temperature control. At 35 K, there is a 3.15 times increase in the baseline HTS technology level, which is measured at 77 K, with no magnetic field. A value of $\eta_I = 3.15$ is used for the rest of this analysis.

Table 5.7 Effects of temperature on I_c

Temperature (K)	η_I
77	0.72
70	1.1
64	1.61
50	2.32
35	**3.15**
20	5.05

The next section shows that a mission with a four hour rotation period, 75 m baseline results in a 2.1 kg coil and a mission with an eight hour rotation period, 75 m baseline results in a 4.2 kg coil. The five kg coil was used for simplicity in the example in this section. For a constant temperature, the coil mass does not have a large effect the value of η_I. For example, a coil mass of 2.1 kg yields an η_I of approximately 3.20, a 1.6% difference in η_I and a coil mass of 4.2 kg yields an η_I of approximately 3.16, less than a 1% difference in η_I.

The final issue to consider is designing the coil for margin. This analysis considers designing for a 10% margin in the force produced by the coil. From Equation (5.22), the force produced by the coils goes as coil mass squared

$$F \sim M_c^{\,2} \tag{5.26}$$

for a constant separation, coil radius, and HTS technology level. Therefore, to produce 10% more force, the coil mass with force margin is approximately 1.049 times greater than the coil mass without margin.

EMFF System results

Figure 5.5 shows the EMFF subsystem mass for a single spacecraft for different HTS technology levels (1x, 3x) and a 1x HTS technology level with 10% force margin in the coil design for three different cases; eight hour rotation period, 75 m baseline (case 1); four hour rotation period, 75 m baseline (case 2); eight hour rotation period, 100 m baseline (case 3). There are several observations that can be made from these results. First, the total EMFF system mass for all of the cases is less than the mass of the PPT system of the JPL design (156.56 kg). In fact for all cases, it is even less than the propellant mass of the JPL design (84 kg) [23].

Second, as the HTS technology level increases the overall system mass decreases. There is a decrease in the mass of the coil and the mass of the power subsystem for cases two and three. As a reminder, the mass of the structures subsystem is constant for all designs. At higher HTS technology levels, the reaction wheel mass becomes the most massive EMFF subsystem.

Third, the EMFF mass for a single spacecraft, given an HTS technology level, can be decreased by the following two scenarios: operating at a slower rotation rate while keeping the same baseline or decreasing the baseline while operating at the same rotation rate. An example of the first scenario examines the 1x HTS technology level designs, at a 75 m baseline for a four hour rotation period (case 2) and an eight hour rotation period (case 1). The case 2 design has a mass of 49.5 kg. Halving the rotation rate to an eight hour period, while keeping a fixed baseline (case 1), results in a mass of 35.2 kg, which is a reduction in mass of approximately 14.3 kg per spacecraft. An example of the second scenario examines the 1x HTS technology level designs, at an eight hour rotation period for a 100 m baseline (case 3) and a 75 m baseline (case 1). The case 3 design has a mass of 48.5 kg. Decreasing the baseline by 25 m, while keeping a fixed rotation rate (case 1)

results in a mass of 35.2 kg; this is a reduction in mass of approximately 13.3 kg per spacecraft.

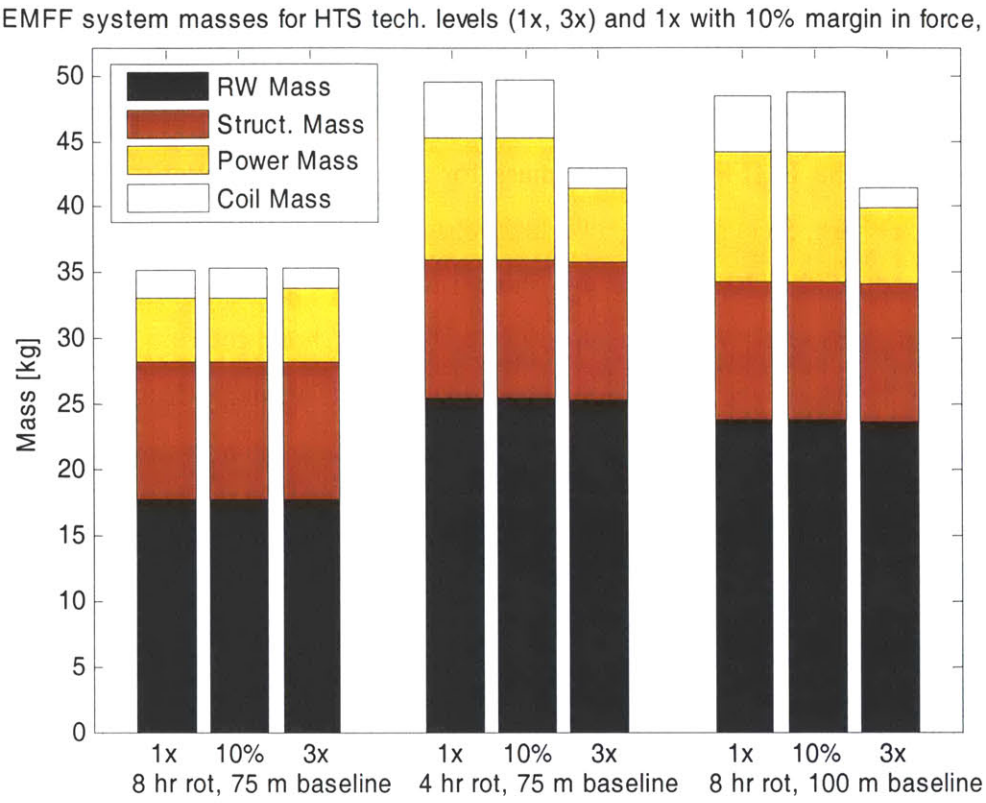

Figure 5.5 EMFF subsystem mass breakdown for various HTS technology levels, rotation periods, and baselines

Fourth, designing for 10% margin in the force does not add a significant amount of mass to the EMFF system. For the 1x HTS technology level designs for case 2, the mass of the coil with margin is 4.405 kg. This is not significantly larger than the mass of the coil without margin, which is 4.2 kg.

It is possible that the baseline and rotation rate are coupled, since larger baseline systems look at more distant stars requiring a slower rotation rate to achieve enough signal to noise (SNR). This analysis does not account for the possible coupling between baseline and rotation rate. The four main observations should not be affected by this coupling.

5.2.3 Micropropulsion System Designs

The current design of TPF uses thrusters to achieve the rotation of the array. The baseline thruster design for the JPL model is Pulsed Plasma Thrusters. This analysis models PPTs, colloids, and FEEPs. A summary of the key equations used to model these micropropulsion systems are shown in Table 5.1. Cold gas thrusters are not considered due to their low I_{xp} (65 s). This section goes into greater detail on some of the micropropulsion subsystems.

In order for TPF to rotate, propellant is constantly expended by the collector spacecraft in order to achieve the centripetal force necessary for a steady state spin. The centripetal force for the outer collector spacecraft is given by

$$F_c = \frac{s}{2} m_{tot} \omega^2 \tag{5.27}$$

where ω is the steady state rotation rate, and m_{tot} is the total spacecraft mass (wet and dry mass). Using Equation (5.27) the ΔV necessary for station keeping the outer and inner collector spacecraft is

$$\begin{aligned} \Delta V_{rotation_{outer}} &= \frac{s}{2} \omega^2 T \\ \Delta V_{rotation_{inner}} &= \frac{s}{6} \omega^2 T \end{aligned} \tag{5.28}$$

where T is the rotation duration. There is no propulsion system necessary on the combiner since it only needs to spin in place, which can be accomplished using a reaction wheel.

Array Slewing

The previous model did not allocate propellant for slewing the array to observe different targets throughout its mission lifetime. Array slewing can be accomplished by two methods. If the array is in a steady state spin, the array can be despun (called a spin-down maneuver), then repointed and rotated in another direction. This maneuver requires

propellant (and time) for the spinup and spindown maneuvers. The total ΔV for N maneuvers for the entire array can be given by

$$\Delta V_{spin} = 2\left(\frac{s}{6}\omega + \frac{s}{2}\omega\right)N = \frac{4}{3}s\omega N \tag{5.29}$$

An alternative method of slewing the array is to precess the entire array while it is spinning. This is achieved by thrusting each spacecraft in a direction normal to the plane of rotation at an appropriate point in the rotation. For small angles, Δi, this maneuver can be approximated as

$$\Delta V_{prec} = N\left(\frac{s}{6}\omega + \frac{s}{2}\omega\right)\Delta i = \frac{2}{3}s\omega N\Delta i \tag{5.30}$$

Comparing Equations (5.29) and (5.30), the precession maneuver is a more efficient method when considering angles less than two radians. To incorporate array slewing, the ΔV for the outer and inner collector spacecraft is now

$$\begin{aligned} \Delta V_{outer} &= \Delta V_{rotation_{outer}} + \frac{1}{2}s\omega N\Delta i \\ \Delta V_{inner} &= \Delta V_{rotation_{inner}} + \frac{1}{6}s\omega N\Delta i \end{aligned} \tag{5.31}$$

Actually, a change in angle of two radians invalidates the small Δi assumption and is much larger than necessary. A good observation schedule for TPF will most likely accommodate small slew maneuvers. The ΔV calculations implement the precession method using 5 degree array slews.

Plume Impingement Avoidance

The propellant plumes created while thrusting are a potential hazard of propellant-based propulsion systems for TPF. Plumes can deposit propellant onto the optics or even thermally blind TPF [1]. Additionally, plume clouds can obscure images that TPF takes. To avoid plume impingement, the thrusters should fire 20-45 degrees off-axis [28] as

shown in Figure 5.6. To approximate a worst-case scenario, thruster firings of 45 degrees off-axis are used. This result increases the total ΔV by a factor of $\sqrt{2}$.

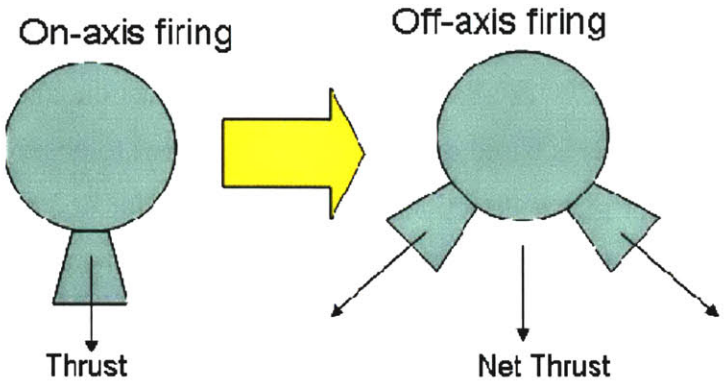

Figure 5.6. On-axis and off-axis thruster configuration

Non-observation time

TPF does not rotate for its entire mission lifetime and there is some allotted mission downtime where it is assumed that TPF does not move. These downtimes are used for communications, to uplink the next observational scenario and downlink any science data. While constant rotation does place an upper bound on the amount of propellant, it does not provide an accurate mission scenario. According to JPL, the goal of TPF is to have 75% of the mission time allocated for observation [29]. Observation consists of planet detection maneuvers and spectroscopy. Both scenarios require rotation of the array. The observation time fraction, η_{obs}, affects $\Delta V_{rotation}$ by limiting the rotation duration, T, to

$$T = \eta_{obs} T_{lifetime} \tag{5.32}$$

where $T_{lifetime}$ is the lifetime of the mission.

After accounting for array slewing, plume impingement avoidance, and non-observational time the final ΔV calculation can be made by

$$\Delta V_{outer} = \left(\frac{s}{2}\omega^2 \eta_{obs} T_{lifetime} + \frac{1}{2} s\omega N \Delta i\right)\sqrt{2}$$
$$\Delta V_{inner} = \left(\frac{s}{6}\omega^2 \eta_{obs} T_{lifetime} + \frac{1}{6} s\omega N \Delta i\right)\sqrt{2} \quad (5.33)$$

The design uses η_{obs} = 0.75 as the observational time fraction and the number of observations, N is 453. This is based on the fact that TPF plans to observe 151 stars each three times minimum for planet detections. The total ΔV_{prec} for 453 precessions for all collector spacecraft is 1.9 m/s, which is very small compared to the total ΔV needed over a mission.

Reaction Wheel

For the micropropulsion systems, the thrusters are used to rotate the array, while a reaction wheel is used to rotate the individual spacecraft during the revolution. The worst-case momentum storage requirement occurs when the array is at relative rest and needs to be "spun-up" to its operating spin rate. The reaction wheel needs to initiate the rotation of the individual spacecraft about its center of gravity, and the thrusters are used to initiate and maintain the revolution about the combiner. At the maximum spin rate about the spacecraft center of gravity, the spacecraft have the angular momentum defined by

$$h_{spin} = I_{veh}\omega \quad (5.34)$$

where I_{veh} is the moment of inertia of the spacecraft about the spacecraft center of gravity, and ω is the revolution rate of the array. Similar to the EMFF reaction wheel design, there is angular momentum buildup from environment disturbances during array revolution. The total momentum storage requirement for the reaction wheels is

$$h_{rw} = -\left(h_{spin} + h_{env}\right) = -\left(I_{veh}\omega + T_{env}\frac{2\pi}{\omega}\right) \quad (5.35)$$

Given the total angular momentum, the reaction wheel mass is determined using Figure 5.4. This is the same procedure used to determine the reaction wheel mass for the EMFF

system. The results of the reaction wheel selection for an eight hour rotation period, 75 m baseline case are shown for an outer collector in Table 5.8. The reaction wheels for the micropropulsion systems (PPTs, colloids, and FEEPs) have identical masses since the same spacecraft inertia is used. The reaction wheel mass for the micropropulsion systems are very close to the reaction wheel mass of the JPL design (5.96 kg), only a 2.3% difference. The reaction wheel for the EMFF system are larger than the reaction wheels for the micropropulsion systems since the EMFF wheel has to store a much larger amount of angular momentum. The EMFF reaction wheel has to store angular momentum from both the revolution of the array and rotation of the individual spacecraft while the reaction wheel for the micropropulsion systems only have to store angular momentum from rotation of the individual spacecraft.

Table 5.8 Reaction wheel masses for outer collector, eight hour rotation period, 75 m baseline

Propulsion Type	Wheel Mass [kg]
PPT	6.1
Colloids	6.1
FEEPs	6.1
EMFF – Baseline HTS	17.8
EMFF – 10 x Baseline HTS	17.8

Power

The total micropropulsion systems power budget consists of the power for the spacecraft bus, thrusters, and reaction wheel

$$P_{total} = P_{bus} + P_{propulsion} + P_{RW} \tag{5.36}$$

where $P_{propulsion}$ is described in Table 5.1 for PPTs, colloids, and FEEPs. The steady state spacecraft bus power, P_{bus}, and steady state reaction wheel power, P_{RW}, are the same as the EMFF system, 400 W and 22 W respectively. The mass of the solar array is determined using Equation (5.14), also for multi-junction solar cells. The mass of the power processing unit for PPTs, colloids, and FEEPs is also described by Reichbach [1].

Comparison with JPL model

The total ΔV needed over a mission for the inner and outer collector spacecraft is shown as a function of baseline in Figure 5.7. The solid lines represent the outer collector and the dotted lines represent the inner collector. The pair of thick red, medium thickness blue, and thin green lines represent six, eight, and twelve hours of rotation period for the collector. The ΔV for the collector spacecraft with a 100 m baseline, eight hour rotation period, and 10 year mission life is approximately 1,230 m/s according to Martin Lo at JPL [30]. As seen in Figure 5.7, the total ΔV for the outer collector used by the micropropulsion systems with the same mission specifications is 1,124 m/s. This result does not consider any ΔV margin. A 10% margin in the total ΔV would result in a total ΔV (1,236 m/s) that is similar to the JPL design.

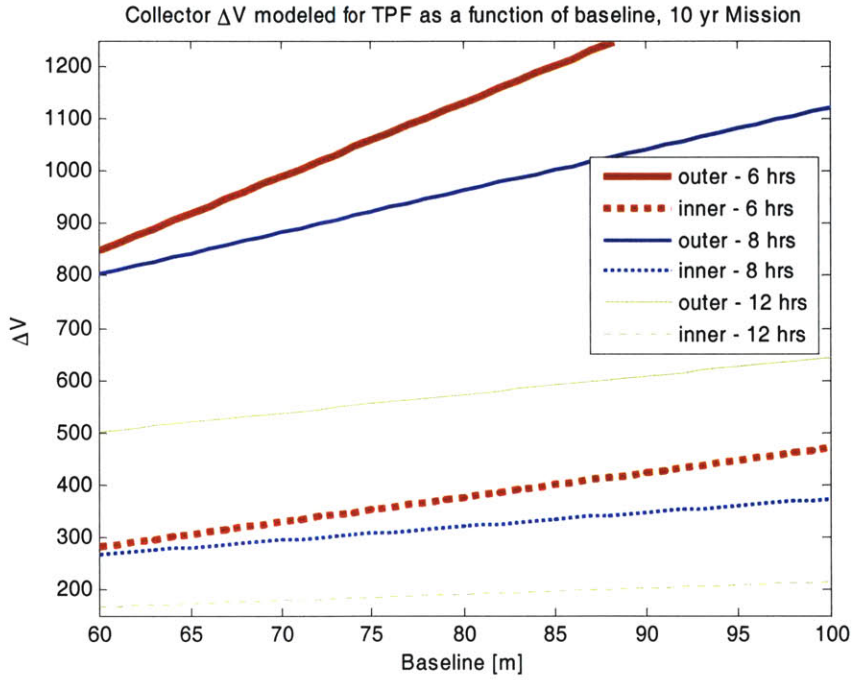

Figure 5.7 ΔV for collector spacecraft

This analysis models sixteen thrusters which are placed in sets of four at each corner of the spacecraft (or sunshield). The mass for the PPT model is compared to the mass of the JPL design and the results are shown in Table 5.9 for a PPT design using a 100 m baseline, eight hour rotation period. It is important to note that these results vary for

different baselines and rotation rates and that it is unknown what exact mission parameters and margins the JPL design is based on. The likely cause of differences are the idealizations in Reichbach's model for the PPT power processing unit and structural mass and the use of margin in the JPL design. The PPT design used an impulse bit, I_{bit}, of $1{,}200 \cdot 10^{-6}$ N·s for a single PPT pulse, which resulted in an I_{sp} of 1,376 seconds. These design parameters could be more efficient than the JPL design possibly resulting in a system with lower mass than the JPL design. The margin built into the JPL design also could have resulted in more massive components and propellant in their model.

Table 5.9 PPT mass comparison

Reaction Control Subsystem Item	JPL Model	Micropropulsion PPT Model
Pulsed Plasma Thruster modules [kg]	30.00	22.20
Power Processing units [kg]	42.56	35.76
Propellant (Teflon) [kg]	84.00	87.48 (outer), 29.16 (inner)
Total	156.56	145.44 (outer), 87.12 (inner)

5.3 Results

The results of the EMFF and micropropulsion models for a four hour rotation period, 75 m baseline TPF mission are seen in Figure 5.8, which plots the total wet mass of all five spacecraft as a function of mission lifetime. The operating temperature of TPF is 35 K. The thin solid horizontal black line at approximately 7012 kg represents the total dry mass of all five spacecraft. This is the mass of the system without a propulsion system, reaction wheel for array spin-up, and solar arrays. The thick dotted horizontal black line at 8112 kg represents the total mass of the JPL design. Any system above this line for any duration mission represents an option that is not mass favorable when compared to the current JPL design.

The PPT and colloid systems (less than 8.5 years) are less massive than the current JPL design, but the EMFF system using current state of the art HTS technology is more favorable than either of them when considering mass. The EMFF system is less massive than the FEEPs system for mission over 6.7 years. The mass of the total EMFF system is 7295 kg, and at ten years the mass of PPTs is 8037 kg, colloids is 8257 kg, and FEEPs is

7349 kg. One potential problem of the FEEPs systems is their contamination potential due to their hot metal (Cesium or Indium) propellant plumes.

The TPF mission is designed for five years of component reliability, and includes ten years of consumables. The total mass of the PPT system at ten years is close to the total mass of the JPL PPT model. Since the PPT system is not based on the JPL PPT model it is not surprising that there is a small difference, especially since the mission parameters (baseline, rotation rate, number of observations, etc) and margins used to determine the JPL PPT system are unknown.

In addition to the micropropulsion trades, an important observation is that the EMFF system trades favorably compared to the JPL model. Higher HTS technology can decrease the overall EMFF system to make it even more mass favorable. In addition, since the EMFF system has no consumables its mission can last beyond ten years.

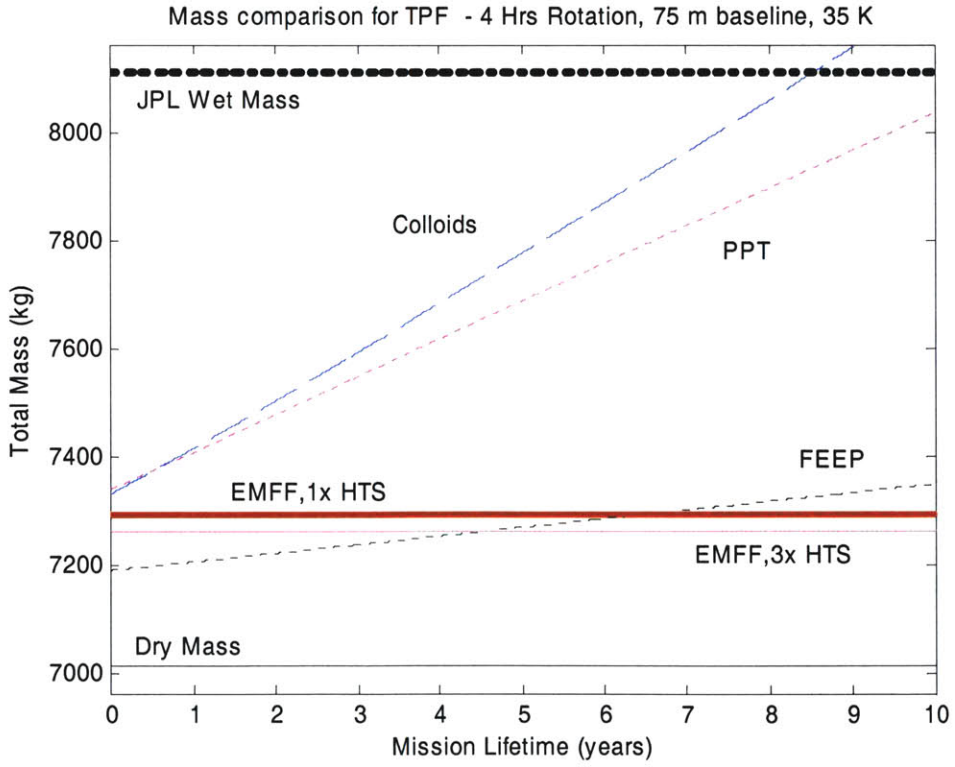

Figure 5.8 Mass comparison for TPF using various propulsion systems, four hour rotation period, 75 m baseline

The mass breakdown for the outer collector, inner collector and combiner spacecraft for the various systems are shown in Figure 5.9. Note that for the propellant-based options, the outer collector is the most massive since it has the highest centripetal load, while the combiner does not have any propulsion mass since it only needs to rotate in place. The propellant-based options also have a relatively high amount of mass (excluding the dry mass) allocated for propellant. If the micropropulsion systems incorporated design margin and the combiner had a propulsion system (which is likely in reality), their overall mass will increase beyond that seen in Figure 5.8.

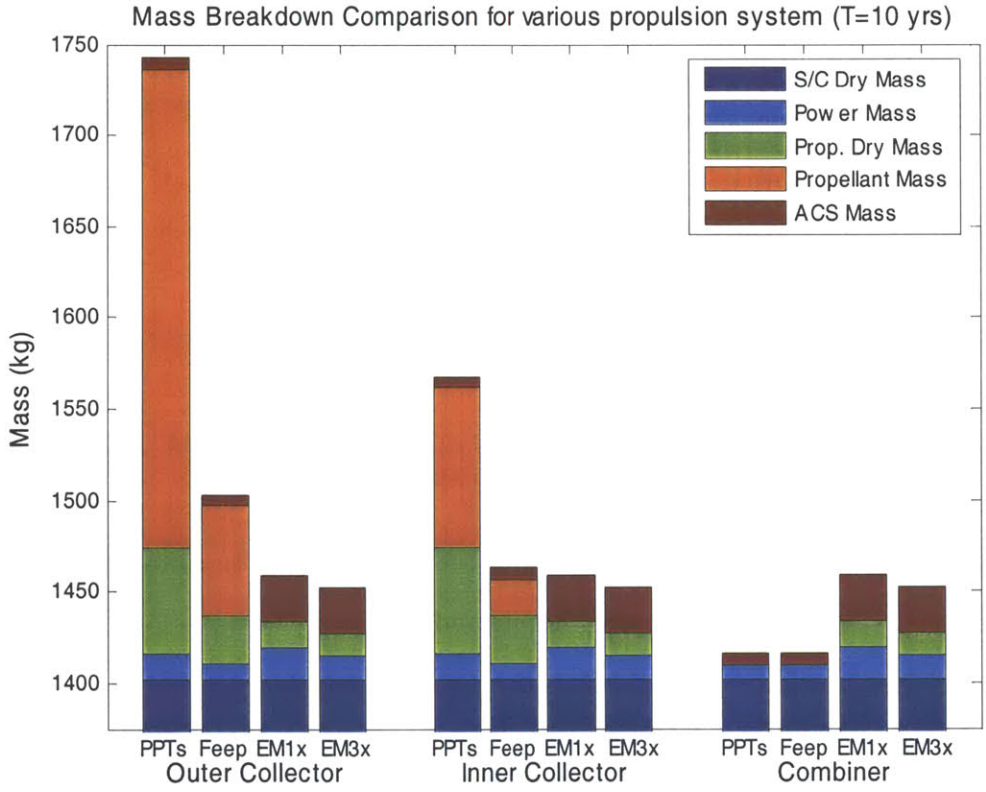

Figure 5.9 Mass breakdown for various propulsion systems, four hour rotation period, 75 m baseline

The effect of designing for different baselines and rotation rates is shown in Figure 5.10 for PPTs and EMFF using 1x HTS technology level (35 K operation) with a ten year mission lifetime. When comparing designs for different rotation rates, some PPT designs are less massive than EMFF designs, however these only exist for PPTs with slower

rotation rates than EMFF. EMFF is more favorable, in terms of mass, than PPTs for all baselines when considering the same rotation rate. For large baseline systems and fast rotation rates, the EMFF TPF design is well below the JPL model.

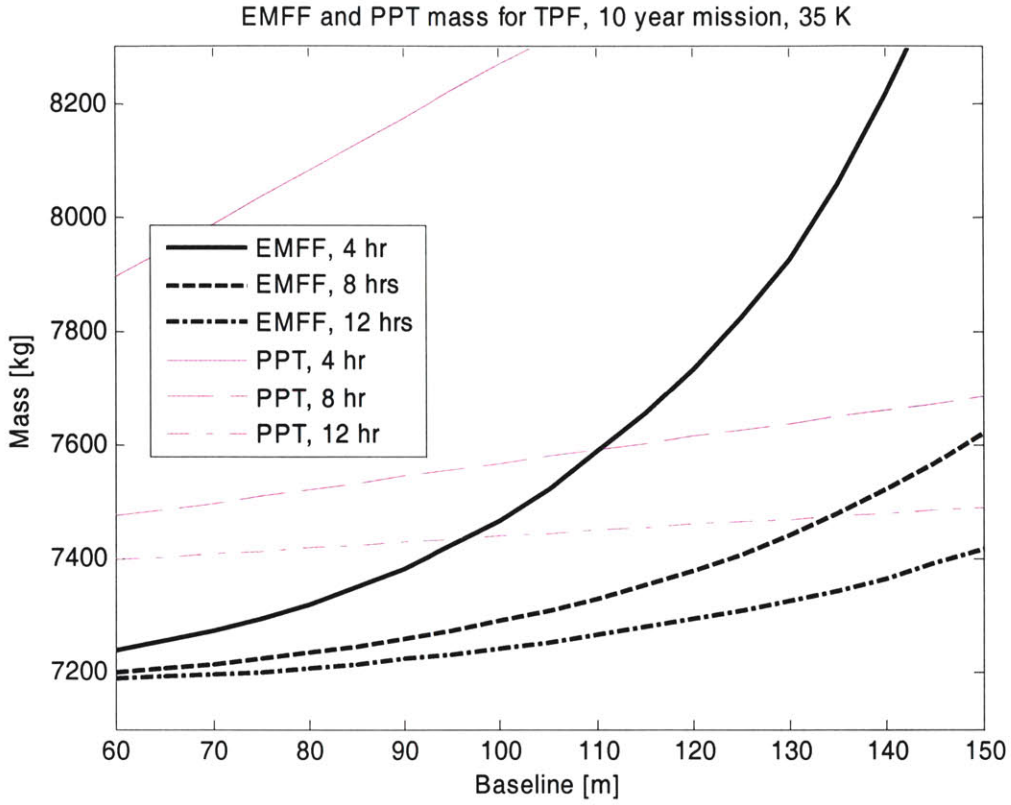

Figure 5.10 EMFF (1x HTS technology) and PPT mass versus baseline for various rotation periods

5.4 Conclusions and Future Work

EMFF is a feasible option for NASA's Terrestrial Planet Finder mission. In this study, electromagnets are shown to provide the centripetal acceleration necessary for array rotation. Furthermore, it does so with subsystem requirements, mass fractions, and power demands that are quite favorable when compared to thrusters.

When compared to propellant-based systems, the EMFF design is deemed to be the most attractive option in terms of mass. Such findings hold valid even for high specific

impulse systems. The lack of propellant contamination and reliance on consumables further reinforces the viability of this EMFF concept.

In theory, the proposed EMFF interferometer can operate indefinitely or at least until component failure, since no non-renewable resources (propellant) are used. System trades incorporating reliability, as well as controllability studies and experimental validation must be performed to determine if such an approach can be made to work.

The design for TPF is under constant revision, so updating the model (dry mass, inertias, spacecraft dimensions, etc) is necessary to continue to understand how the EMFF system trades. Additional work that can be done is to incorporate FEM models of EMFF to the TPF FEM model to understand how the dynamics of the structure are affected. Geometric integration of the coils into the spacecraft warrants further investigation. This involves determining the arrangement of the coils during launch and deployment of the coils after launch.

Chapter 6

EMFF MULTI-ROLE CAPABILITIES

The primary role of EMFF is to impart forces and torques to maintain a satellite array for its specified mission maneuvers. This chapter investigates the feasibility of using EMFF in a multi-role sense, where possible secondary roles include power transmission, passive offensive and defensive capabilities, and communications. These expanded capabilities can add greater value and versatility to EMFF spacecraft.

6.1 Power Transmission

EMFF has a unique ability to generate power on a non-EMFF satellite by means of flywheel energy storage modules (FESM). The basic concept contains at least one EMFF satellite and one non-EMFF satellite without a power generation system. This is illustrated in the left half of Figure 6.1. The EMFF satellite generates power through solar arrays, which are not pictured. By generating a magnetic field, the EMFF satellite is able to rotate a permanent magnet attached to a reaction wheel on the non-EMFF satellite. Flywheel energy storage is a method to convert the rotational energy into electrical energy using a generator. To maintain zero net angular momentum in the system, the non-EMFF spacecraft must have two reaction wheels of equal mass spinning in opposite directions at the same speeds. This is done with two permanent magnets attached to the reaction wheels with dipoles in opposite directions, such as those pictured in Figure 6.1.

A possible time history of the EMFF dipole orientation and strength and the permanent magnet orientations in the xy-plane are shown in Figure 6.2. The two permanent magnets spin about the z-axis (directed out of the page) and are shown separated at times t_0, t_2, and t_4 for clarity. Initially, no EMFF dipole is generated, shown by the dot. On the non-EMFF vehicle, the two permanent magnets are aligned in phase. This is an unstable

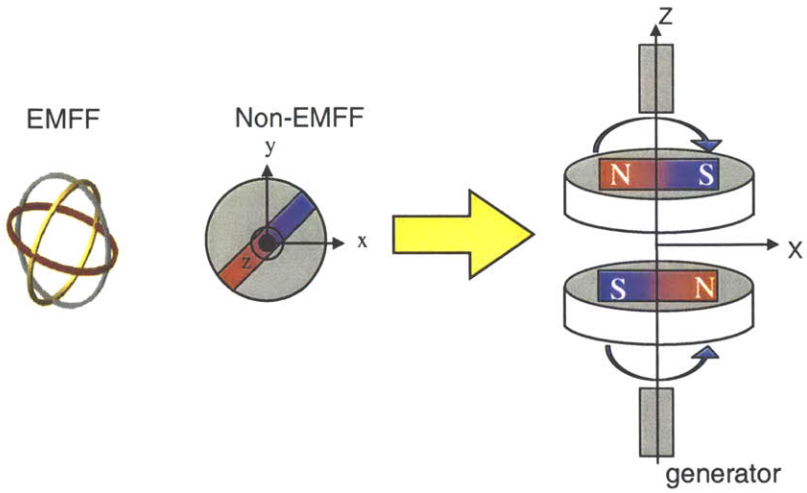

Figure 6.1 Diagram of EMFF-FESM power sharing concept with non-EMFF vehicle reaction wheel arrangement

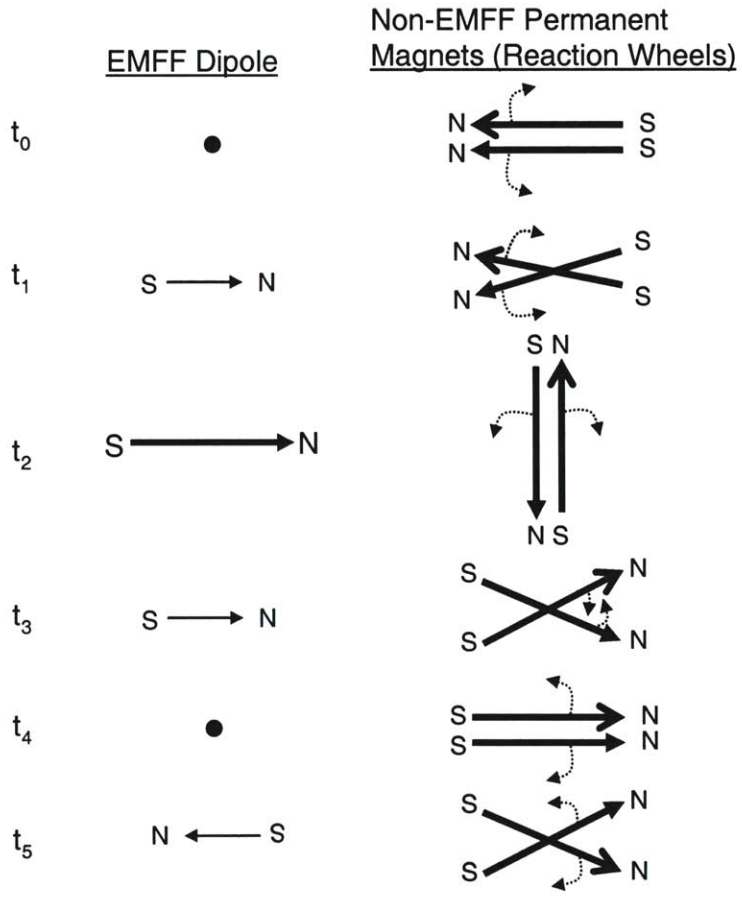

Figure 6.2 Notional time history of EMFF dipole and permanent magnet orientations in xy-plane

configuration and a small perturbation can initiate them to spin. One possible direction of spin is shown in Figure 6.2. Next, at time t_1 an EMFF dipole is generated to push the north ends of the permanent magnets apart causing them to rotate even more. At time t_2, the EMFF dipole strength is increased, shown by the thicker line. The EMFF dipole exerts a clockwise torque on the right magnet, which is rotating clockwise, and a counterclockwise torque on the left magnet, which is rotating counterclockwise. At time t_3, the EMFF dipole strength is reduced. Now the EMFF dipole pulls the south ends of the permanent magnets together. The rotating permanent magnets are momentarily aligned at time t_4. This push pull cycle repeats itself after time t_5.

The rotational kinetic energy for each reaction wheel is equal to the stored energy in a lossless system described by

$$KE = \frac{1}{2} I\omega^2 = \text{Stored Energy} = U \tag{6.1}$$

For a real system with an efficiency factor, η, and using a solid reaction wheel disk, the stored energy for the two reaction wheel system is

$$\begin{aligned} U &= \eta \frac{1}{2} m_w r_w{}^2 \omega^2 \\ I &= \frac{1}{2} m_w r_w{}^2 \quad \text{for a solid disk} \end{aligned} \tag{6.2}$$

where m_w is the reaction wheel mass including the permanent magnet, r_w is the reaction wheel radius, and ω is the wheel rotation rate. The rotation rate of the system is constrained by the magnetic field switching capabilities of the EMFF system. This is determined by the ability to change current through the EMFF coil, which is described by the inductance equation from Chapter 4,

$$v = L\frac{di}{dt} \rightarrow \omega = \frac{V}{iL} \quad , \quad L[u\text{H}] \simeq 39.37 \frac{n^2 R_c}{9} \tag{6.3}$$

The rotation rate achievable by EMFF is a function of the coil parameters, where N is the number of turns and R_c is the coil radius. Substituting Equation (6.3) into Equation (6.2) and dividing by the reaction wheel mass yields an equation for the specific energy density

$$\frac{U}{m}[\frac{\mathrm{W}\cdot\mathrm{hr}}{\mathrm{kg}}] = 7.26\cdot 10^{6}\cdot \eta {r_w}^2 \left(\frac{V}{in^2 R_c}\right)^2 \tag{6.4}$$

where the numerical constant is obtained by various unit conversions. Using parameters in Table 6.1, which contains coil parameters similar to the EMFF testbed, the specific energy density obtained is

$$\frac{U}{m}[\frac{\mathrm{W}\cdot\mathrm{hr}}{\mathrm{kg}}] = 8.04 \tag{6.5}$$

Table 6.1 EMFF-FESM power sharing parameters

Parameter	Symbol	Quantity	Units
Coil voltage	V	50	volts
Coil current	i	10	amps
Coil turns	n	100	turns
Coil radius	R_c	0.425	meters
Reaction wheel radius	r_w	1	meters
Efficiency factor	η	0.8	-

The specific energy density generated in this example is sufficient for low power systems on satellites. Energy generated is increased by lowering the inductance of the coil which is achieved by either decreasing the number of turns or decreasing the coil radius. Increasing the voltage can increase the frequency of the magnetic field, which can also lead to a higher energy generation. One challenging aspect of this power sharing maneuver is the synchronization of reaction wheels by the oppositely aligned dipoles. By placing them 180° out of phase at certain times, it is possible that the reaction wheels will self align during the rotation ensuring that one wheel does not move ahead of the other wheel, preventing angular momentum build up. The permanent magnets must be

designed so that they have the strength to perform this alignment and also enough strength to react with the EMFF field to spin up in a reasonable amount of time. An additional benefit of this maneuver is that any number of reaction wheel pairs can be run in parallel. One could position two additional flywheel energy storage modules to Figure 6.1, with one on top and one beneath the pictured system.

A concept related to power transmission is power sharing between two EMFF spacecraft, using the coils from the two separate spacecraft as primary and secondary pairs of a transformer. In a typical power transformer, a highly permeable material guides the majority of the magnetic flux from one coil through the other coil. However, for EMFF the permeability of free space (μ_o) is so small that it limits the amount of magnetic flux that passes from one coil to the other coil. The limiting factors for this power sharing concept are the low magnetic flux, low permeability, and slow current switching abilities (due to high coil inductance). Because of these limitations, there are minimal power sharing capabilities unless special configurations are used, such as a small EMFF spacecraft docked within a much larger EMFF spacecraft. In this configuration, the small EMFF spacecraft sees a portion of the magnetic flux from the coil of the larger EMFF spacecraft.

6.2 Passive offensive capability

A passive offensive capability is defined as any set of maneuvers where one satellite does not directly impinge another proximate satellite either by direct contact or by its emissions. The passive offensive capability of EMFF exploits a target's thrusters to impinge on itself as shown in Figure 6.3. A charged particle from a thruster, such as from an electric propulsion thruster, follows a trajectory according to the Lorentz force

$$\vec{f} = q\left(\vec{E} + \vec{v} \times \vec{B}\right) \tag{6.6}$$

which is a function of the particle charge, q, the external electric field, $\vec{E}$, the particle velocity, $\vec{v}$, and the external magnetic field, $\vec{B}$. Assuming a negligible external electric field in the space environment, the path of the ion is a circle which is given as

$$\vec{f} = \frac{m_{ion} v_y^{\,2}}{R} = q v_y B_z \tag{6.7}$$

using the coordinate frame from Figure 6.3. The external magnetic field is created by a nearby EMFF satellite which according to the figure is either behind the target satellite or in front of it in the xy-plane. This configuration allows the EMFF satellite to create a magnetic field in the z-direction. From each location, the EMFF satellite can switch the magnetic field in either the positive or negative direction by switching its steerable dipole allowing circular particle trajectories to be created on either side of the satellite. Moving the EMFF satellite relative to the target affects the magnetic field strength for a given magnetic moment creating different circular trajectories. Thus the particle can impinge on any number of places including on the EMFF vehicle. Figure 6.3 shows how this can be done to impinge on a solar array, and also a camera on the far side of a satellite, which is obstructed by the solar arrays. The precision of particle deposition depends on the plume size and the uniformity of the magnetic field. A magnetic field that is not uniform over the entire particle does not create a perfect circular path.

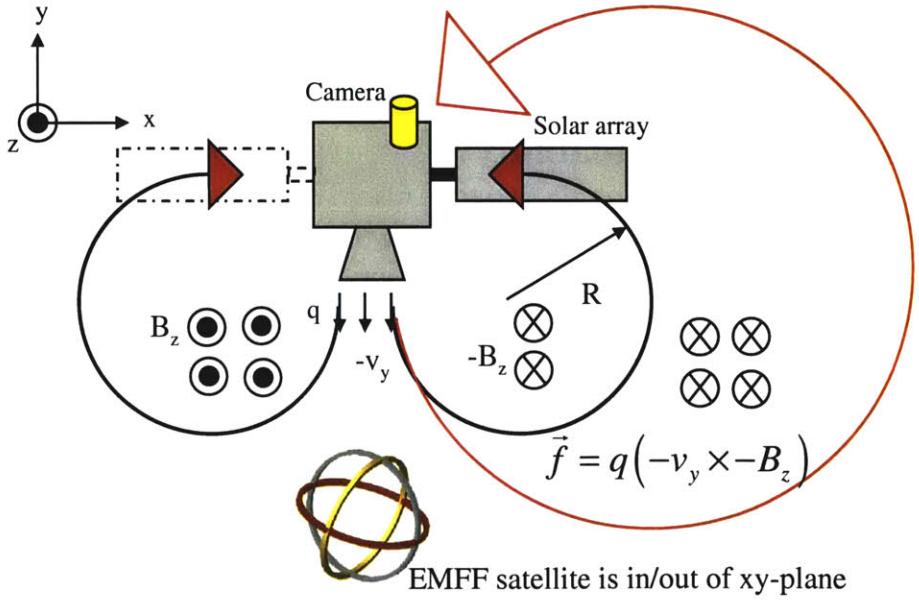

Figure 6.3 EMFF Deny, Degrade concept diagram

Understanding how these various circular trajectories are created begins with a description of the EMFF magnetic field, which is a function of the magnetic moment, μ, and the distance, d, given by

$$B_z \simeq \frac{\mu_o}{2\pi}\frac{\mu}{d^3} \tag{6.8}$$

Substituting μ from Equation (3.3) into Equation (6.8) and expressing the magnetic field in terms of the HTS critical current density, I_c, wire density, ρ_c, and coil mass, M_c, yields

$$B_z \simeq \frac{\mu_o}{2\pi} I_t \frac{\pi R_c}{d^3} = \frac{\mu_o}{4\pi}\left(\frac{I_c}{\rho_c}\right)\left(M_c R_c\right)\frac{1}{d^3} \tag{6.9}$$

From Equation (6.7), the magnetic field necessary for a certain particle motion is

$$B_z = \frac{m_{ion} v_y}{qR} \tag{6.10}$$

Setting Equation (6.10) equal to Equation (6.9), allows the maximum radius of the circular trajectory to be described by the separation between the EMFF satellite and the target. This relationship is shown in Figure 6.4 using the parameters listed in Table 6.2, where the thick blue curve is for the current state of the art for HTS wire. The thin red curve shows a ten times improvement in HTS technology, represented by the I_c over ρ_c ratio, and the dotted magenta curve represents a hundred times improvement. The dotted line represents the condition when the particle radius is equal to the separation distance. Above the line, the magnetic field produced may not be uniform over the entire particle trajectory. Operation of this passive offensive maneuver likely occurs below the line, where the uniform magnetic field approximation hold true for larger separation distance and smaller particle radii. The results show that the current state of HTS wire gives limited abilities, however given a ten times HTS improvement allows separation distances greater than 10 meters. With a hundred times increase in HTS technology, the range of particle trajectories and the distances needed to create these trajectories could be sufficient for some desired applications. It is important to note that Figure 6.4 illustrates

the maximum radius of the particle path. A larger radius can be created by decreasing the magnetic moment, which is done by decreasing the current through the coils.

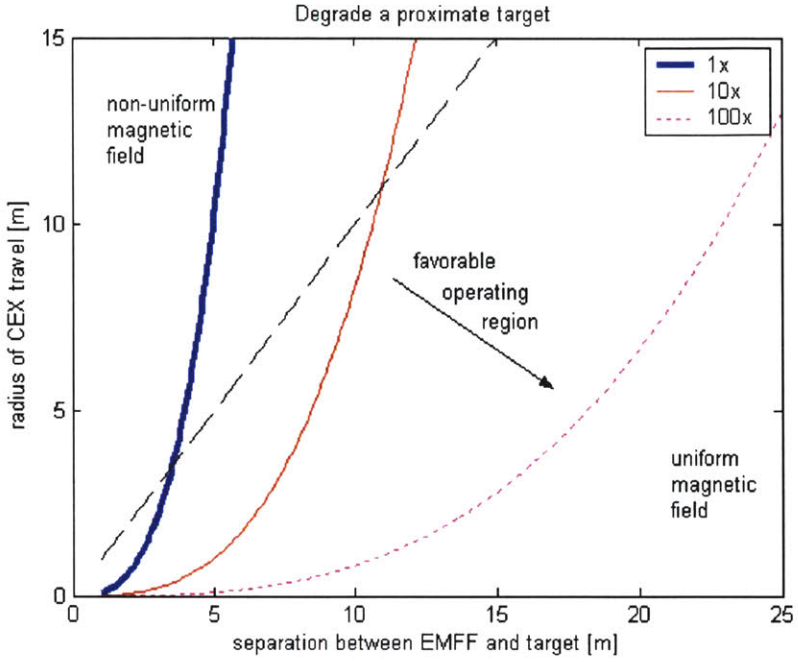

Figure 6.4 Degradation capabilities

Table 6.2 EMFF and target satellite parameters

Parameter	Symbol	Quantity	Units
Ion mass	m_{ion}	$2.16\ 10^{-25}$	kg
Ion velocity	v_y	3000	m/s
Particle charge	q	$1.6\ 10^{-19}$	Coulombs
EMFF coil design	$M_c \cdot R_c$	30	kg·m
Current state of HTS wire	I_c/ρ_c	16250	A·m/kg

In this analysis EMFF is targeting a SPT-100 class Xenon Hall Thruster and affecting the charge exchange (CEX) ions because of their relatively low speeds and low plume population; they constitute less than 2% of the propellant plume. Because of these characteristics, the EMFF vehicle can more discretely affect a target. In terms of operational procedure, the target thrusters must be those for attitude control, not main thrusters, otherwise the EMFF satellite would need some way of following the target. The EMFF satellite can loiter nearby, then approach the target periodically and alter trajectory paths to affect the target in a slow and inconspicuous fashion.

6.3 Passive Defensive Capabilities

Affecting particle trajectories using EMFF can also be used as a defensive capability. If charged particles are approaching an EMFF satellite, for example from a nearby satellite's thruster plumes, EMFF can redirect the particles away by creating a magnetic field that is perpendicular to the particle velocity. This utilizes the Lorentz force in the absence of an electric field. This idea of an EMFF protective magnetosphere is similar to the shielding effect that the Earth's magnetic field has on solar radiation as shown in Figure 6.5. The EMFF protective magnetosphere could be used to shield a satellite from certain types of radiation or plumes depending on the strength of the field generated and the mass and velocity of the particle.

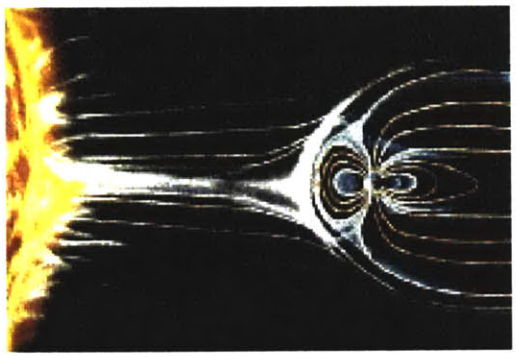

Figure 6.5 EMFF protective magnetosphere

Sensor spoofing can be accomplished using EMFF on a target satellite with a magnetic compass or guidance system based on the Earth's magnetic field as a reference. The EMFF satellite could have the ability to affect their sense of direction and use this maneuver for detection avoidance. In addition, the reaction wheel speed on a target can be affected by an EMFF satellite. A metallic wheel experiences eddy currents in a magnetic field which slow down the wheel. Thus, an EMFF satellite has the potential ability to adjust a target's attitude in a passive defense maneuver.

6.4 Communications

It is possible to use the coils from two EMFF satellites as transmitter receiver pairs. However, similar to the problems of power sharing, the coils likely have inductances that

are too large to offer sufficient bandwidth due to the large number of turns and size. In addition, this system most likely does not trade favorably with commercially available communications systems, some of which are less than 5 kg [25], unless the coils were designed specifically for the communications application.

However, similar to the testing of GPS hardware in an EMFF system, communications between EMFF-enabled spacecraft using COTS RF systems have been tested and are not affected by the magnetic fields produced at the level the MIT SSL has tested [9]. On the MIT-SSL EMFF ground testbed, two radio frequency systems by RF Monolithics, the DR-1012-DK and DR-2000 models, did not experience loss of packets when tested inside the EMFF vehicles with a field of approximately 50 Gauss. In summary, EMFF does not seem to pose a problem for satellite communication systems, nor does it enhance it beyond commercially available systems.

6.5 Multi-role Conclusions

This chapter investigated EMFF multi-role capabilities in power transmission and offensive and defensive capabilities. Overall, the EMFF multi-role capabilities are enabled by lower inductance systems and higher levels of HTS technology. While the large inductance of the coils may not be viable for communications, the fields generated at the testbed level indicate that COTS technology for metrology and communications are unaffected and viable for use on a flight system, however further testing is recommended. A potential multi-role capability that was not investigated is the possible use of the EMFF coils as torque coils for attitude control. This concept could be similar to using magnetic torque rods in low Earth orbit for angular momentum dumping.

Chapter 7

CONCLUSIONS

7.1 Thesis Summary

The overall objective of this thesis was to analyze the effect of EMFF on multi-spacecraft arrays and spacecraft subsystems. To achieve this overall objective, the following sub-objectives were recognized:

- Develop trades on the performance of multi-spacecraft arrays using EMFF; performance is defined as the spacecraft agility and mission efficiency.
- Formulate models to describe the subsystems associated with EMFF.
- Develop a systematic framework for the implementation of EMFF on TPF.
- Investigate the potential benefits of using EMFF for multiple roles.

The following is a chapter-by-chapter summary of the research performed to meet these objectives.

Chapter 2

This thesis began with an introduction of designing for a space interferometer such as TPF using uncertainty and completeness. The uncertainty associated with detecting Earth-like planets around other stars was modeled as a Poisson distribution. A large uncertainty drove the mission towards a desire for more observations, and therefore shorter baselines to detect planets. For a small uncertainty, operating at longer baselines granted access to a much larger volume of stars, in order to successfully detect planets. Since the interferometer architecture must be selected well before the uncertainty can be determined, the most robust solution was to make the baseline variable, over a relatively large extent, allowing operation in either mode. The completeness of a fixed baseline

(SCI) and variable baseline (SSI) interferometer were compared and it was concluded that a system that is tunable posed the least science risk. Formation flight is one method of creating a tunable architecture and this thesis considered using electromagnets to achieve formation flight.

Chapter 3

Design of propellant-based systems for formation flying is reliant on the ΔV required for maintaining orientation. Designs of EMFF systems do not have this constraint. Instead, the parameters affecting EMFF systems are the High Temperature Superconducting (HTS) wire critical current density and volumetric mass density, coil size, coil mass, and spacecraft separation distance(s). These parameters were used to optimize the performance of multi-spacecraft arrays. There were two performance metrics defined. The first was the agility of an EMFF system undergoing circular and linear trajectories. The agility of the system was modeled as the array rotation rate for the circular trajectories and the linear acceleration for the linear trajectories. The second performance metric was the mission efficiency of the array, which was defined as the ratio of rotation rate to array mass.

There were several conclusions from the performance trades. First, it was found that creating asymmetric arrays with mother-daughter relationships resulted in an increase in performance. An optimum distribution of the coil mass existed that maximized the array rotation rate, linear acceleration, or mission efficiency. For example, the mission efficiency of a three spacecraft array analyzed in Chapter 3 was maximized when approximately 50% of the electromagnetic mass was located on the center spacecraft. The second conclusion was that adding additional EMFF spacecraft increased the performance of the array. For example, a three spacecraft system in a circular trajectory could achieve one revolution in less than three minutes while a two spacecraft system could not achieve one revolution in ten minutes. A third conclusion was that the linear trajectories created by EMFF have higher agility than circular trajectories, however their control was very sensitive to changes in the magnetic moment profile. To understand

these boundaries of sensitivity, escape velocity and the idea of operating with margins was introduced.

Chapter 4

The system trades in Chapter 3 allowed for an overall picture of EMFF performance. The next step was to understand the subsystems required for EMFF in greater detail. These included the effects of temperature and magnetic field on the HTS wire, the thermal designs for insulating and cooling the HTS wire, the effect on agility posed by structural components holding the coil to the spacecraft, the amount of power required by EMFF, the overall power design, and the effect of EMFF on avionics. The magnetic field seen by the HTS wires reduced the critical current density while operating at lower temperatures increased the critical current density. It was shown that spacecraft can achieve a six times improvement in acceleration by operating at 40 K compared to the acceleration at 77 K for HTS where the effect of the magnetic field is not considered. In addition, there was a linear relationship between the total loop current and the number of turns.

The design of the thermal subsystem was investigated to ensure that superconducting temperatures can be sustained for the EMFF coils. Insulation or vacuum-gap designs required on the order of ten Watts of heat flow to be rejected depending on the insulation material properties, coil geometry, and orbit.

Effects of the structure necessary to support the EMFF coils were investigated to understand how larger sized coils more realistically impacted agility. By increasing the coil radius, even by a small percentage, a significantly higher acceleration was achieved even when accounting for the additional structural mass needed.

The design of an EMFF power system was conducted to ensure a high current, low voltage driver was achievable using reasonable amounts of power. An H-bridge design was chosen and D-cell batteries supplied current to the coils. The power system required to drive current through the coils was on the order of fifty to one hundred watts per coil for the MIT-SSL EMFF testbed. These results were obtained by experimentation and

verified by analysis. Finally, the performance of avionics in the presence of EMFF fields was tested using GPS equipment. A 50 Gauss magnetic field was produced by the MIT-SSL EMFF testbed and did not impact the signal to noise ratio obtained by the GPS receiver.

Chapter 5

A model of TPF operating at 35 K was designed to include the EMFF subsystems from the previous chapter and was used to benchmark EMFF against various micropropulsion systems (PPTs, colloids, and FEEPs). The micropropulsion systems experienced an exponential increase in propellant mass because of the relationship with ΔV. The EMFF system mass was constant over the mission lifetime. For a mission with a four hour rotation period and a 75 m baseline, the EMFF system was more favorable over the micropropulsion options in terms of mass. The EMFF system was less massive than the FEEPs system for mission longer than 6.7 years. The mass of the total EMFF system was 7295 kg, and at ten years the mass of PPTs was 8037 kg, colloids was 8257 kg, and FEEPs was 7349 kg. The EMFF system also was less massive than the JPL designed system (8112 kg) which used PPTs as their propulsion system. Higher science productivity has the potential to be achieved using EMFF, and higher levels of HTS technology lead to the most attractive EMFF design.

Chapter 6

In previous chapters, the primary role of EMFF was to impart forces and torques to maintain a satellite array. This chapter investigated using EMFF in a multi-role sense, in other words, determining potential secondary roles of EMFF. These included power transmission and passive, offensive capabilities. Power generation using an EMFF spacecraft and a non-EMFF spacecraft with flywheel energy storage modules was capable of producing a specific energy of approximately 8 Watt hours per kilogram. The EMFF spacecraft was used to rotate permanent magnet dipoles located on the non-EMFF spacecraft's reaction wheel. The mechanisms behind aligning the dipoles on the non-EMFF spacecraft warrant further investigation.

A second EMFF multi-role capability was using propellant plumes on nearby target satellites to impinge itself. The magnetic field created by the EMFF spacecraft was used to guide propellant particles from the target thruster back onto the target spacecraft. Since EMFF does not contact the target, it is a passive, offensive maneuver. This capability was most favorable when separation between the EMFF satellite and target were large and when the HTS wire had a large critical current density.

7.2 Contributions

The following are contributions made by this thesis.

- Theoretical analysis of the detection of Earth-like planets on other stars using completeness and uncertainty.
- Developed trade analysis tools to evaluate the performance of multi-spacecraft arrays.
- Designed subsystem models for EMFF spacecraft and the MIT-SSL EMFF testbed.
- Development of a systematic framework for the implementation of EMFF on a rotating space interferometer, specifically the Terrestrial Planet Finder.
- Proposed and demonstrated the viability of using EMFF for secondary roles.

7.3 Recommendations for Future Work

There are several topics that would benefit from additional research.

Circular and linear trajectories of EMFF arrays were simulated separately in Chapter 3; however to further the understanding of EMFF maneuvers, a simulation capable of creating hybrid circular and linear trajectories could be created. One could design an array containing EMFF spacecraft with a payload and EMFF spacecraft without a payload. These EMFF spacecraft without a payload, or EMFF intermediaries, are used for the sole purpose of bridging the magnetic field. This simulator would investigate the effect of adding EMFF intermediates. A possible result would determine the optimal number and size of the EMFF intermediaries that maximize agility or mission efficiency.

The model of the coil was restricted to be circular since its symmetry allowed for an easy model of the far field. However, other coil shapes such as elliptical or triangular configurations should be investigated to understand how they compare to circular coils. One of the potential benefits of other configurations is that they can be folded or arranged in such a way to fit inside a launch vehicle and then deployed to create a total area larger than circular coils.

The thermal design of EMFF could be experimentally verified by a future EMFF testbed. Using a thermal vacuum chamber, the space environment can be simulated while a small HTS coil could be operated. This is likely a challenging task since it requires additional subsystems, such as the power system, to also operate in the simulated space environment. Therefore, some of the testbed subsystems may have to be redesigned. Successful demonstration of an EMFF testbed in a more realistic space environment has the potential to increase the technology readiness level of EMFF. Additional work on the testbed involves verification of the near field and far field models and testing of more sensitive avionics equipment such as a CCD.

The baseline TPF specifications from NASA will undoubtedly change throughout the years. As components such as the sun shield, aperture size, or separation distances change it is important to update the model accordingly. Since the mission is several years in the future, it is important to understand the near term and far term evolution of HTS wire and how it affects future TPF designs.

APPENDIX A

This section goes into greater detail on the I_2 calculations for $\alpha \neq 3$. Starting with Equation (2.14) for Case 2.

$$I_2 = 4\pi \int_{R_{min}}^{R_{min}} \int_{r_i}^{r_o} n_s n_p R^2 dr dR = 4\pi \int_{\frac{2r_iB}{\lambda}}^{\frac{2r_oB}{\lambda}} \int_{\frac{\lambda R}{2B}}^{r_o} \frac{a_s}{R^\alpha} \frac{a_p}{r} R^2 dr dR \tag{8.1}$$

Solving the first integral yields

$$I_2 = 4\pi \int_{2q}^{2p} a_s a_p R^{2-\alpha} \ln(\frac{2p}{R}) dR \tag{8.2}$$

where $p = \frac{r_o B}{\lambda}$ and $q = \frac{r_i B}{\lambda}$. Now integrating by parts

$$\begin{aligned} u &= \ln(\frac{2p}{R}) \quad & dv &= R^{2-\alpha} dR \\ du &= -\frac{1}{R} dR \quad & v &= \frac{R^{3-\alpha}}{3-\alpha} \end{aligned} \tag{8.3}$$

$$I_2 = 4\pi a_s a_p (\frac{R^{3-\alpha}}{3-\alpha} \ln(\frac{2p}{R}) + \frac{1}{3-\alpha} \int_{2q}^{2p} \frac{R^{3-\alpha}}{R} dR) \tag{8.4}$$

$$I_2 = 4\pi a_s a_p (\frac{R^{3-\alpha}}{3-\alpha} \ln(\frac{2p}{R}) + \frac{R^{3-\alpha}}{(3-\alpha)^2}) \Big|_{2q}^{2p} \tag{8.5}$$

$$I_2 = \frac{4\pi a_s a_p}{(3-\alpha)^2} (R^{3-\alpha}((3-\alpha)\ln(\frac{2p}{R}) + 1)) \Big|_{2q}^{2p} \tag{8.6}$$

yields Equation (2.17)

$$I_2 = 4\pi a_s a_p \frac{1}{(3-\alpha)^2} ((2p)^{3-\alpha} - (2q)^{3-\alpha} - (2q)^{3-\alpha}(3-\alpha)\ln(\frac{p}{q})) \tag{8.7}$$

Bringing out q and substituting for p and q

$$I_2 = 4\pi a_s a_p \frac{1}{(3-\alpha)^2}\left(\frac{2r_i B}{\lambda}\right)^{3-\alpha}\left(\left(\frac{r_o}{r_i}\right)^{3-\alpha} - 1 - (3-\alpha)\ln\left(\frac{r_o}{r_i}\right)\right) \tag{8.8}$$

Using $r_o = 6\, r_i$,

$$I_2 = 4\pi a_s a_p \frac{B^{3-\alpha}}{(3-\alpha)^2}\left(\frac{2r_i}{\lambda}\right)^{3-\alpha}\left(6^{3-\alpha} - 1 - (3-\alpha)\ln(6)\right) \tag{8.9}$$

which can be used in the $I_1 + I_2$ calculation.

REFERENCES

[1] Reichbach, Jeffery G., Sedwick, Raymond J., and Martinez-Sanchez Manuel, *Micropropulsion System Selection for Precision Formation Flying Satellites*, Masters Thesis, Massachusetts Institute of Technology, SERC #1-01, January 2001.

[2] Elias, Laila M, and Miller David W., *Dynamics of Multi-Body Space Interferometers Including Reaction Wheel Gyroscopic Stiffening Effects: Structurally Connected and Electromagnetic Formation Flying Architectures*, Ph.D. Thesis, Massachusetts Institute of Technology, SSL #5-04, March, 2004.

[3] Kong, Edmund M.C., *Spacecraft Formation Flight Exploiting Potential Fields*, Ph.D. Thesis, Massachusetts Institute of Technology, SERC #2-02, February 2002.

[4] Sedwick, R.J. and S.A. Schweighart, *Propellantless Spin-Up and Reorientation of Tethered or Electromagnetically Coupled Spacecraft*, SPIE 4849-26, SPIE Highly Innovative Space Telescope Concepts Conference, Waikoloa, HI, Aug 22-28, 2002.

[5] Schweighart, S.A. and R.J. Sedwick, *High-Fidelity Linearized J2 Model for Satellite Formation Flying*, Journal or Guidance Control and Dynamics, Vol 25 No.5, Sept-Oct, 2002.

[6] Hashimoto, T., Sakai S., Ninomiya K., et al., *Formation Flight Control Using Superconducting magnets*, 2002.

[7] King, Lyon B., Parker, Gordon G., Deshmukh, Satwick, et al., *NIAC Phase I Final Report: Spacecraft Formation-Flying using Inter-Vehicle Coulomb Forces*, Michigan Technological University, January 2002.

[8] Miller David W., Sedwick Raymond J., et al., *NIAC Phase I Final Report: Electromagnetic Formation Flight,* Massachusetts Institute of Technology, December 2002.

[9] EMFFORCE Design Document, MIT Space Systems Product Development Class, May 2003.

[10] Schweighart, Sam, *Open Loop Dynamics of Satellites Flying in Formation using Electromagnets* (working title-not yet finished), Ph.D Thesis, Massachusetts Institute of Technology, Feb., 2005.

[11] Brown, Robert A., *Obscurational Completeness*, Space Telescope Science Institute, 2003.

[12] Beichman, C. A., Woolf, N. J., and Lindensmith, C. A., ed., *The Terrestrial Planet Finder (TPF): A NASA Origins Program to Search for Habitable Planets*, JPL Publication 99-003, 1999.

[13] 16.89 Students, *Paradigm Shift in Design for NASA's New Exploration Initiative*, Massachusetts Institute of Technology, 16.89 Space System Design Final Report, Spring 2004.

[14] Fischer, Debra, Valenti, Jeff A., and Geoff Marcy. *Spectral Analysis of Stars on Planet-Search Surveys*. IAU S219: Stars as Suns: Activity, Evolution and Planets. ASP Conference Series, 2004.

[15] Chung, Soon-Jo, and Miller, David W., *Design, Implementation and Control of a Sparse Aperture Imaging Satellite,* Masters Thesis, Massachusetts Institute of Technology, SSL Report #19-02, August, 2002.

[16] Makins, Brian. *Interferometer Architecture Trade Studies for the Terrestrial Planet Finder Mission*. Masters Thesis, Massachusetts Institute of Technology, February 2002.

[17] Sedwick, Raymond. *Coordinatization of Ideal Magnetic Dipole-Dipole Interaction*, MIT Space Systems Lab Internal Document. August 9, 2002.

[18] American superconductor, "Bi-2223 High Strength Wire," URL: http://www.amsuper.com/products/htsWire/index.html [cited 2 February 2003].

[19] KAS and ISB, *Cryogenic Thermal Performance (EM#1) at 0℃*, PowerPoint Presentation slides, NASA Goddard Space Flight Center, Cryogenics and Fluids Branch.

[20] Wheeler, H.A., *Inductance Formulas for Circular and Square Coils*, Proc. IEEE, Vol 70, no. 12, pp. 1449-1450, Dec. 1982.

[21] Fairchild Semiconductor. HUF76145P3, HUF76145S3S UltraFET Power MOSFETs Data Sheet, December 2001.

[22] Kong, Edmund M.C., Kwon, Daniel W., Schweighart, Samuel A., et al., *Electromagnetic Formation Flight for Multisatellite Arrays*, Journal of Spacecraft and Rockets, Vol. 41, No. 4, July-August 2004.

[23] Beda, Michael G., *Structural Analysis Summary Collector Spacecraft* Presentation, Jet Propulsion Laboratory, June 11, 2004.

[24] Jet Propulsion Laboratory, FFI Power Profile 9-2003 Excel Spreadsheet.

[25] Wertz, James R., and Larson, Wiley J., *Space Mission Analysis and Design*, 3rd Edition, Microcosm Press, 1999.

[26] Mitchell, Scott, Terrestrial Planet Finder Solar Radiation Pressure and Torque, Ball Aerospace, April 13, 2004.

[27] Constellation Series Reaction Wheels, Honeywell Aerospace, http://content.honeywell.com/dses/assets/datasheets/constellation_series_reaction_wheels.pdf, 2002.

[28] Miller, David W., Notes for the TPF-SWG Technical Interchange Meeting, July 30-31, 2003.

[29] Jet Propulsion Laboratory, Mission Time Budget Excel Spreadsheet (FFI activity), November, 3, 2003.

[30] Lo, Martin W., TPF Baseline FFI Mission Design, PowerPoint presentation, Jet Propulsion Laboratory, Version 5/6/03.